ABSTRACT

Title of Document:	DEVELOPMENT AND APPLICATION OF INTEGRATED SILICON-IN-PLASTIC MICROFABRICATION IN POLYMER MICROFLUIDIC SYSTEMS
	Likun Zhu, Doctor of Philosophy, 2006
Directed By:	Associate Professor Don L. DeVoe, Department of Mechanical Engineering

Polymer-based microfluidic devices can offer a number of advantages over conventional devices, and have found many applications in chemical and biological analysis. In order to fully develop a lab-on-chip (LOC) device, the functional components, such as sensors and actuators, tend to be assembled to complete a functional device. But the integration of silicon chips into polymer-based microfluidic systems remains a virtually unexplored area. In this work, a novel silicon-in-plastic microfabrication technology is developed, which involves seamlessly integrating individual microfabricated silicon chips into a larger polymer substrate, where the silicon components provide functionality, and the plastic substrate provides system-level fluid handling. This technology employs low-cost polymer substrates and simple polymer processing techniques which are amenable to mass production.

The fabrication and testing of two polymer microfluidic systems using the silicon-in-plastic technology are presented in this dissertation. The first integrated microsystem is a water-based chemical monitoring system based on microhotplate gas sensor and polymer microfluidics. The chemical monitoring system is designed to sample a water source, extract solvent present within the aqueous sample into the vapor phase, and direct the solvent vapor past the integrated gas sensor for analysis. Design, fabrication, and characterization of a prototype system are described, and results from illustrative measurements performed using methanol, toluene, and 1,2-dichloroethane in water are presented.

The second one is an integrated UV absorbance detection system that uses silicon-in-plastic technology to seamlessly integrate bare photodiode chips into a polymer microfluidic system. Detection platforms fabricated using this approach exhibit excellent detection limits down to 1.5×10^{-8} M for bovine serum albumin (BSA) as a model protein. In addition to providing high sensitivity, sub-nanoliter detection volumes are enabled by the use of direct photodetector integration. The fabrication methodology is detailed, and system performance metrics including minimum detection limit, detection volume, dynamic range, and linearity are reported.

DEVELOPMENT AND APPLICATION OF INTEGRATED SILICON-IN-PLASTIC MICROFABRICATION IN POLYMER MICROFLUIDIC SYSTEMS

By

Likun Zhu

Dissertation submitted to the Faculty of the Graduate School of the
University of Maryland, College Park, in partial fulfillment
of the requirements for the degree of
Doctor of Philosophy
2006

Advisory Committee:
Associate Professor Don L. DeVoe, Chair
Professor Balakumar Balachandran
Associate Professor Cheng S. Lee
Assistant Professor Bao Yang
Assistant Professor Adam Hsieh

Dedication

To my parents for their support and encouragement in this endeavor.

Acknowledgements

I would like to thank my advisor, Professor Don L. DeVoe, for his support, insights and encouragement throughout this dissertation work. I would also like to thank Dr. Steve Semancik, Dr. Doug Meier, Dr. Zvi Boger, Mr. Chip Montgomery and Mr. James Melvin at NIST for their assistance and input throughout this work.

I would like to express my appreciation to Professor Cheng S. Lee, and Dr. Yan Li for their help in the protein detection project. I am indebted to Tom Laughran, Nolan Ballew, and Jonathan Hummel for their expertise in the cleanroom. Finally I would like to thank my friends and colleagues at Maryland Microfluidics Lab, Yi Zhou, Lihua Li, Jing Liu, Wei-Jen Cheng, Parshant Kumar, Chris Kimball, Nate Sniadecki, and Lou Hromada for their assistance and advice in this work.

TABLE OF CONTENTS

List of Tables

List of Figures

Chapter 1

Introduction

1.1 Microfluidics in Silicon-Based Substrates

Microfluidic devices have found many applications in fields including chemical and biological analysis, drug delivery, molecular separation, amplification, sequencing or synthesis of nucleic acids, and environmental monitoring. Such devices can offer a number of advantages over conventional analytical tools. For example, the required sample volumes, analysis times, and consumption of reagents and analytes can be greatly reduced. In addition, devices can be made portable. For several microfabrication methods, the cost may also be significantly lower than macro-scale fluidic systems, which makes disposable devices feasible.

Microfluidic devices are commonly associated with the terms “lab-on-a-chip (LOC)” and “micro total analysis systems (μTAS)”, which arose historically from the analytical chemistry community. The first microfluidic device was a miniaturized gas chromatography system developed at Stanford Univeristy in the 1970s [1]. It was fabricated on a silicon wafer using photolithography and chemical etching techniques.

In 1990, a conceptual μTAS paper was published [2], which led to wide developments and discoveries in this field, first only in academic research, but since the mid 90s also on a commercial basis. In the beginning, microfluidic devices often used silicon as a substrate material to leverage compatibility with exiting methods of microfabrication used in microelectronics and MEMS industries. Further development focused on various types of glass or quartz as substrate materials, as the conductivity of silicon proved problematic for the application of high voltages needed for electroosmotic flow [3]. The simplest microfluidic devices were microchannels fabricated on a silicon wafer, using standard photolithography and subsequent wet etching. In order to increase functionality of the microfluidic devices, additional components have been integrated into silicon, glass or quartz substrates including heaters, resistive temperature sensors [4, 5] , pumps [6, 7] , and valves [8, 9].

The silicon, glass and quartz based microfluidic devices are fabricated using the exiting techniques for microelectronics devices. However, for the ongoing commercialization of this technology, these fabrication processes represent certain disadvantages, such as fabrication cost and limitations in geometrical design due to the isotropic nature of the etching processes [3]. Polymers as substrate material offer a possible solution to these fabrication challenges and lend themselves to the mass fabrication of microfluidic devices. Compared with silicon, quartz and glass, polymers are inexpensive, and microchannels can be formed by molding or embossing rather than etching. Their wide range of material properties, low costs, and

the development of suitable polymer microfabrication methods in the past few years have attracted significant interest [3].

1.2 Integrated Polymer Microfluidics

1.2.1 Polymer Microfluidics

Polymers are macromolecular substances with a relative molecular mass between 10000 and 1000000 Da and more than 1000 monomeric units. The polymerization process is started by an initiator substance or a change in the physical parameters (light, pressure, temperature). Due to the great length of the polymer chain, polymers are bulk materials [10]. In most cases polymers are amorphous or in some cases microcrystalline, where the length of the polymer chains is larger than the size of the crystallites. In the study of polymers and their applications, it is important to understand the concept of the glass transition temperature, T_g. As the temperature of a polymer drops below T_g, it behaves in an increasingly brittle manner. As the temperature rises above T_g, the material becomes plastic-viscous and can be molded.

There are a wide variety of polymers which have been used for microfabrication processes, including polyamide (PA), polycarbonate (PC), polymethylmethacrylate (PMMA), polyimide (PI), polybutyleneterephthalate (PBT), Polystyrene (PS), polypropylene (PP), polyethylene (PE), polyoxymethylene (POM), polyphenylene ether (PPE), polysulfone (PSU), cyclic olefin copolymer (COC), parylene, polydimethylsiloxane (PDMS), SU-8, and epoxy. To date, PMMA and PC are the

most popular materials for microfabrication via hot embossing and injection molding. Fabrication of microfluidic devices in PDMS by casting is also a faster and less expensive method. COC is a relatively new polymer material for microfluidic devices, and it attracts more and more interest due to its excellent light transparency, good chemical resistance, low water absorption, and low gas permeability. SU-8 is a negative photoresist material developed by IBM for UV-lithography, and it has been used for fabricating high aspect ratio microfluidic channels [11].

Many techniques of fabricating microchannels in polymers have been developed. They can be divided into two general categories: direct micromachining techniques and replication techniques. Direct micromachining techniques fabricate each single device individually. This allows a rapid fabrication of single device, but the fabrication throughput is limited by the fabrication time of each individual device. Reported techniques for direct micromachining include laser ablation [10, 12] , optical lithography in deep photoresists [11, 13], Stereolithography [14], and surface micromachining [15]. However, these techniques have not found significant commercial applications in microfluidic devices due to their high cost. Replication techniques are good for polymer microfluidics fabrication, because they are generally much less expensive than direct micromachining and the principles behind these processes are already well known in the macroworld. In general, replication techniques can be divided into three categories: casting, injection molding, and hot embossing. Casting can offer flexible and low-cost access to planar microchannel structures. The mostly used material is poly (dimethylsiloxane) (PDMS), such as the

Sylgard 184 formulation offered by DuPont, which offers good optical properties into the UV range. In this microfabrication method, a mixture of the elastomer precursor and its curing agent are poured over a molding template. After curing, the soft elastomer copy can simply be peeled off the mold. Injection molding is one of the most widespread processes for fabricating polymer parts in the macroscopic world. In this process, a molten polymer is injected into an evacuated mold, where it is cooled until solid and then ejected. Hot embossing is a widely used replication process to fabricate channel structures for microfluidic applications. In this fabrication process, a thermoplastic polymer is heated above its glass transition temperature, pressed against a mold, and cooled down below the glass transition temperature before separating. These replication methods represent commercial pathways for the microfabrication of microfluidic devices, with the potential for high volume and low cost production.

In order to form enclosed microfluidic networks, the microchannels which are normally open after the fabrication steps have to be sealed, obviously without clogging the channels, changing their physical parameters, or altering their dimensions. This can be accomplished by adhesive bonding, thermal bonding, lamination, plasma treatment, or solvent treatment as outlined below:

Thermal bonding Typical thermal bonding heats the polymer close to its glass transition temperature to allow sufficient melting at the interface between the two

substrates. This has been commonly reported for PMMA and polycarbonate [16, 17].

Lamination A lamination film generally consists of two polymers: a melting adhesive and a cover layer. The film is heated above the glass transition temperature of the adhesive layer and rolled onto the structure with a heated roller. The softened adhesion layer bonds to the surface of the wafer, sealing the microchannels. Finally, localized areas of the film can be peeled off to provide access holes for fluid and electrical connections. This method works well for large channels. However, the adhesive tends to block smaller channels.

Adhesives Similar to lamination, adhesives with a low viscosity can be applied as a thin coating to bond a wafer with microchannels to another wafer, creating a sealed device. The adhesives can be epoxy, PDMS or other compounds. But this method also has the risk of blocking the small channels.

Plasma Treatment This method was only applied to sealing PDMS microfluidic structures [18]. The PDMS surface to be bonded is exposed to oxygen plasma, which activates surface functional groups and allows for siloxane (Si-O-Si) bonds when it contacts with another suitable surface, such as PDMS, glass, or silicon.

Localized Bonding Several methods have been reported for bonding a localized area, rather than an entire wafer. These include the use of lasers [19] and lithographically patterned heaters [20].

Solvent treatment The polymer substrates can be bonded by solvent treatment, because polymers can be readily dissolved by some solvents [21, 22]. In this

study, a solvent bonding technique is used to bond two polycarbonate surfaces permanently with a room temperature curing.

1.2.2 Silicon Components in Polymer Microfluidics

Microfluidic channels are only part of a functional analysis system. In order to fully develop a lab on chip (LOC) device, other functional components, such as sensors and actuators, must be integrated with the polymer-based microchannels. For example, Thorsen et al. developed a microfluidic chip in PDMS which contains plumbing networks with thousands of micromechanical valves and hundreds of individually addressable chambers [23]. These fluidic devices are analogous to electronic integrated circuits fabricated using large-scale integration.

The most basic integrated functionality on a polymer microfluidic substrate can be realized by adding a patterned metal layer, which can form electrodes, heaters, thermocouples, etc. For example, an integrated microfluidic system for temperature measurement and control was recently reported [24]. In this system, a thin layer of Cr and Cr/Au were deposited on PC to form a two-dimensional array of resistive temperature sensors and a serpentine microheater in a microchannel. However, compared with patterned metal layers, semiconductor devices can offer substantially more functionality. But directly depositing semiconductor materials on polymers is not practical, since the semiconductor processing usually involves high temperatures which are not compatible with polymer substrates. Fabricating semiconductor devices together with integrated silicon-based [1] or polymer-based [25] microfluidics is

feasible, but not cost effective due to the high expense of silicon processing. Because microfluidic networks are generally large, with length scales in the cm-range, substantial silicon real estate is expended to support the microchannels, and only a small fraction is used to provide additional functionality beyond simple fluid flow.

As an alternate cost-effective approach for integrating semiconductor elements into polymer microfluidic systems, silicon-based devices can be batch fabricated on a silicon wafer and then diced into individual chips which can be integrated into an inexpensive polymer microfluidic system. In this case the silicon processing costs are not wasted on producing simple microchannels. To date, very little work has been done in this area. One similar work was reported by Mastrangelo, and consisted of a polymerase chain reaction (PCR) device cast in epoxy [26]. This system was fabricated by manually assembling a glass capillary with a wire coiled around it, a thermoelectric cooler, and an Omega Engineering thermocouple. This assembly was then cast in epoxy. However, no microfabrication was used in this system. Other work involves the integration of LED chips was reported by Uchiyama in 2001 [27]. In this work, a microfluidic device was fabricated in polyester by in-situ polymerization, and a blue LED was integrated into the polyester microchannel as a fluorescence excitation light source, with an optical fiber integrated into the microchannel for the collection of emitted fluorescence. However, the LED used in this work is a fully packaged device. The LED chip is not really seamlessly integrated inside the microchannel, and the distance between the chip and the microchannel could be more than 1 mm.

1.3 Dissertation Objective

The integration of silicon chips into polymer-based microfluidic systems remains a virtually unexplored area. There are two primary challenges in this integration work. The first challenge is how to embed individual silicon chips into polymer-based microchannels to seamlessly form fluidic interconnection between the polymer substrate and the silicon chip. The second challenge is how to make electrical access to the silicon chip embedded in the microchannel.

The main objective of this dissertation work is to develop a set of techniques to seamlessly integrate functional silicon chips into polymer-based microfluidic systems (silicon-in-plastic), and apply this technique to the development of two miniaturized chemical and biological analysis systems, namely: (1) a water-based chemical monitoring system, and (2) a protein UV absorbance detection system. The water monitoring system based on metal oxide microhotplate gas sensors combined with polymer microfluidics is developed as a disposable sensor to monitor and characterize volatile organic compounds (VOCs) in water supply systems. The integrated protein UV absorbance detection system combines commercial silicon photodetectors with polymer microfluidics, and is developed to demonstrate the potential for the silicon-in-plastic technology in monitoring protein separations without resolution loss due to sample dispersion when passing through the detection region.

1.4 Dissertation Organization

This dissertation consists of 5 chapters. Chapter 1 contains a brief introduction to polymer-based microfluidics and the integrated functional components in microfluidics. In Chapter 2, the silicon-in-plastic microfabrication technology is described in detail. This technology can be used to seamlessly integrate functional silicon chips into polymer-based microfluidic systems. In Chapter 3, the development of a water-based chemical monitoring system using silicon-in-plastic microfabrication, including design, fabrication and experimental results, is presented. The development of an air-liquid two-phase flow system in polymer microfluidic systems, which is used to perform solvent extraction in the water monitoring system, is also described in this chapter. In addition, a detailed vapor transport model is presented to model the air-liquid two-phase flow system, including 2-D membrane vapor diffusion and bulk gas flow. In Chapter 4, the development of an integrated polymer microfluidic platform for UV absorbance detection of proteins is described, including the detail of design, fabrication and experimental results. Finally, the conclusion of this work and the suggestion for future work are presented in Chapter 5.

Chapter 2

Silicon-in-Plastic Microfabrication

2.1 Overview

In order to integrate individual silicon chips into polymer-based microfluidic systems, a novel silicon-in-plastic microfabrication technology has been developed [28, 29]. This technology employs low-cost polymer substrates and simple polymer processing techniques which are amenable to mass production. The first step of this microfabrication is to seamlessly embed the silicon chip into the polymer substrate. The fabrication process is shown in Figure 2.1. First, a round hole large enough to accommodate the silicon chip is milled through the polymer substrate. After milling, the burrs around the hole were removed by a deburring tool. The silicon chip is placed face-down on a partially cured flat PDMS layer, and the milled polymer substrate is positioned over the chip, with the chip located inside the milled hole. The PDMS layer provides for easy mold removal while also forming a seal against the surface of the chip. The mold is placed under vacuum and filled with epoxy (353ND, EPO-TEK). Casting in vacuum can prevent air bubbles from becoming trapped at the edge of the chip, which appear as large pits when the mold is removed. Filling the

mold under vacuum is accomplished by placing a syringe loaded with epoxy and air in the vacuum. The fill rate can be controlled by the diameter and length of the needle and epoxy viscosity. The epoxy is gelled at room temperature overnight, then cured at 120 ° C for 30 min. After curing, the PDMS is removed. The epoxy serves to secure the chip in the polymer substrate, while leveling the front chip surface to within several microns of the polymer surface.

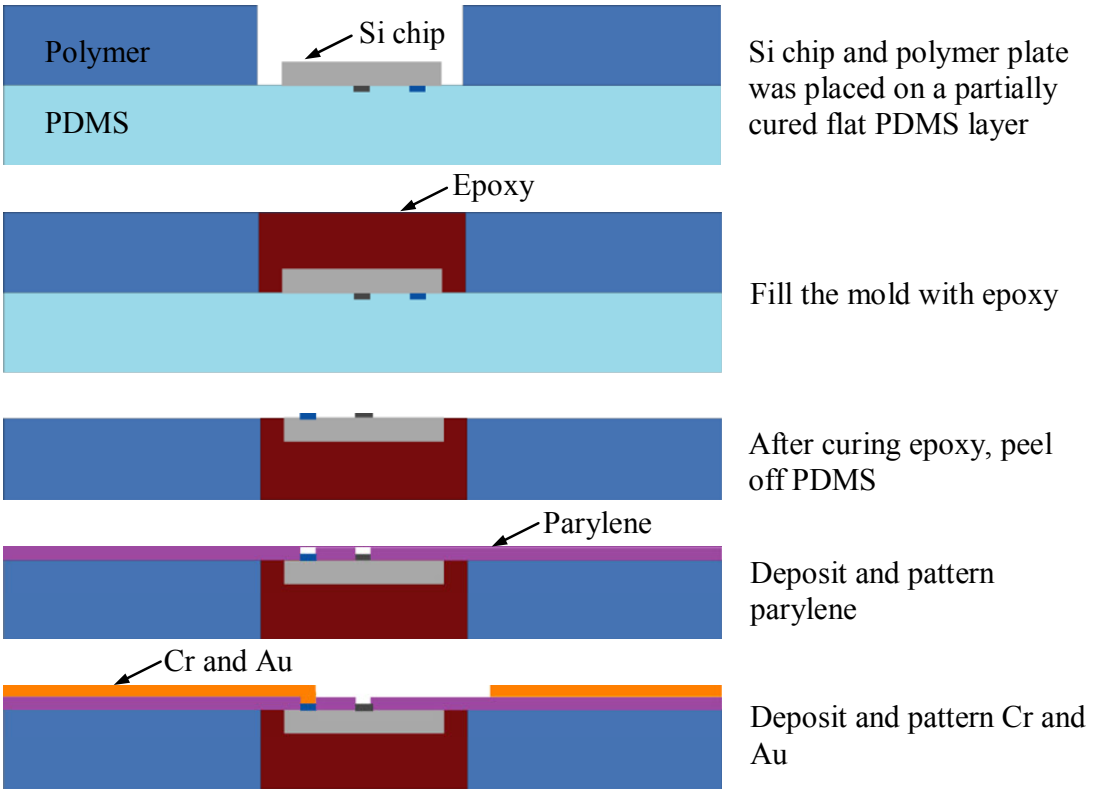

Figure 2.1 The fabrication process of integrating silicon chip into polymer substrate.

2.2 Passivation Layer

Although the epoxy layer can level the silicon chip surface to within several microns of the polymer surface, the small gaps usually occur between the

silicon/epoxy/polymer interfaces due to epoxy shrinkage during curing. The surface profile of the typical silicon/epoxy/polymer interfaces is shown in Figure 2.2. The gaps can cause several problems during the metal deposition and patterning processes. First, the sidewall of the diced silicon chip is bare silicon, which is semiconductor. If the metal layer deposited in the later process contacts the sidewall of silicon chip in the gaps, the interconnection will be shorted by the bare silicon. Second, the interconnection trace may be open at the silicon/epoxy/polymer interfaces, because the thickness of metal layer is several thousands angstrom and the gaps may be several micron deep. To overcome this problem, a passivation layer is needed to bridge small gaps and isolate the bare silicon with the metal layer.

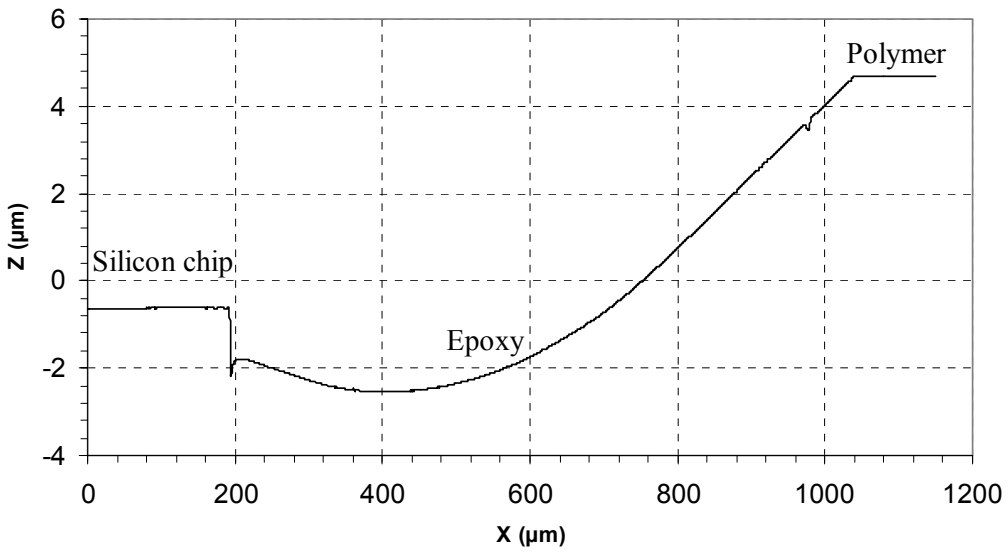

Figure 2.2 Surface profile of silicon/epoxy/polymer interfaces.

There are some polymers which have been used as passivation layer in semiconductor devices, including polyimide (PI), benzocyclobutene (BCB), and parylene. Photosensitive polyimide (PI-2771, HD MicroSystems) is widely used as a

passivation layer in the semiconductor devices or dielectric material in the printed circuit boards, etc [30]. The photosensitive polyimide allows smooth angled sidewalls to be readily fabricated with a 60-70° slope, which provides an excellent surface for metallization. However, the main solvent (N-methyl pyrrolidone, NMP) in polyimide tends to attack many polymers [31], including both the epoxy and polycarbonate used in this work. In order to solve this problem, a thin layer of parylene C (< 1 μm) is deposited and patterned (RIE, O_2 plasma) to protect epoxy and polycarbonate before polyimide coating. However, the fully cured condition for PI2771 is 350 °C for 1 hour in a convection oven or furnace. This temperature will melt most suitable polymers. In this case, PI2771 can only be partially cured.

Benzocyclobutene (BCB) is a high purity organic polymer commercialized by the Dow Chemical Company under the tradename Cyclotene. It is developed for microelectronics applications and already widely used as dielectric layer for high density interconnect substrates (multi chip modules, MCM-D). This polymer can be spin-coated and patterned by lithography. But, again, the high curing temperature (above 250 °C) of BCB severely limited its compatibility to other polymer substrates with low glass transition temperature such as PC and PMMA.

Due to its ease of fabrication and compatibility of polymer substrates, parylene C can be used as the passivation layer in this fabrication. Parylene is a common name for a class of polymers called poly (para-xylylene). Six forms of parylene are currently available. Each form represents the basic polymer backbone of xylylene with a

replacement of 1-4 atoms in the ring. The basic structure of the parylene polymers is shown in Figure 2.3.

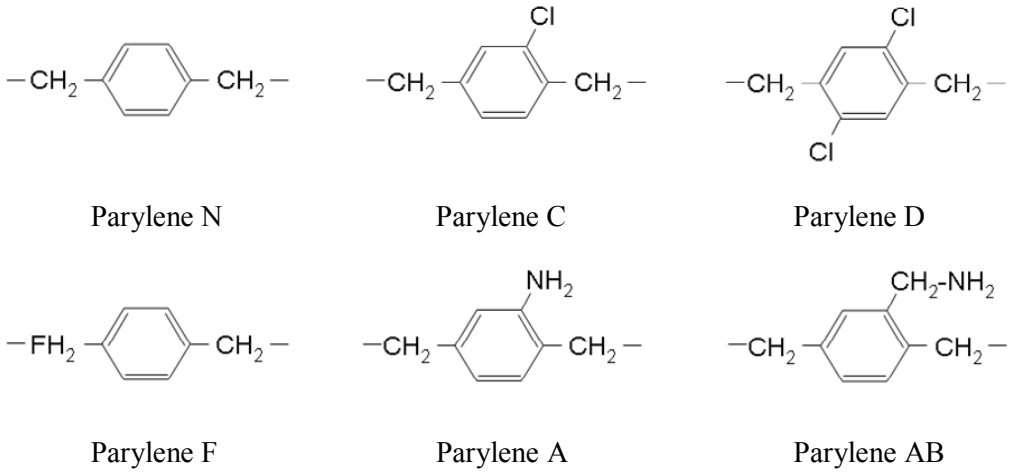

Figure 2.3 Molecular structures of parylene monomers.

Parylene can be deposited by vapor deposition at room temperature in a vacuum. Figure 2.4 shows a diagram of the deposition process, known as the Gorham process [32]. The parylene dimmer (solid) is first sublimated at 120-170° C. The vapor is then drawn into the pyrolysis chamber where the dimmer molecule is then split into two monomers at 680-720° C. The monomers will then polymerize on surfaces below 100° C, although the deposition chamber is typically at room temperature. The low temperature of the deposition chamber is compatible with a wide range of polymer substrates with low glass transition temperature, e.g. PC or PMMA. Since the deposition is done at 0.1 torr, the mean free path of the monomer is on the order of centimeters, which creates pinhole-free conformal coatings. Unlike vacuum metallization that has a high mean free path, the deposition of the parylene monomer

is not line of sight due and all sides of the object are uniformly coated. The deposition process has excellent thickness control down to the sub-micron range.

Of the parylene forms, parylene C has the highest dielectric constant. The melting temperature is 290° C. When the film is at a temperature below the melting temperature, it is resistant to all solvents. These properties make parylene C an ideal polymer candidate for the passivation layer used in silicon-in-plastic microfabrication. In order to completely bridge the gaps, 6~7 μm parylene layer was deposited on the polymer substrate. As can be seen from Figure 2.5, the gap between silicon chip and epoxy has been filled with parylene. This parylene layer can also help bridge the gap and isolate the sidewall of silicon chip prior to metal deposition. However, the bondpads and other functional elements on the silicon chip are also coated by the parylene layer. So the parylene layer needs to be patterned to expose the bondpads and other functional elements. Parylene can be patterned in oxygen plasma with a photoresist mask or metal mask [33, 34]. Cr/Au layer was used as the etching mask in this fabrication process. First, 200 Å Cr and 2000 Å Au was deposited on the substrate by sputtering. Second, the metal was patterned by photolithography and wet etching. Third, the whole device was etched by oxygen plasma (0.58 Torr, 100 W) to expose bondpads and other functional elements. At last, the Cr and Au were removed by wet etching.

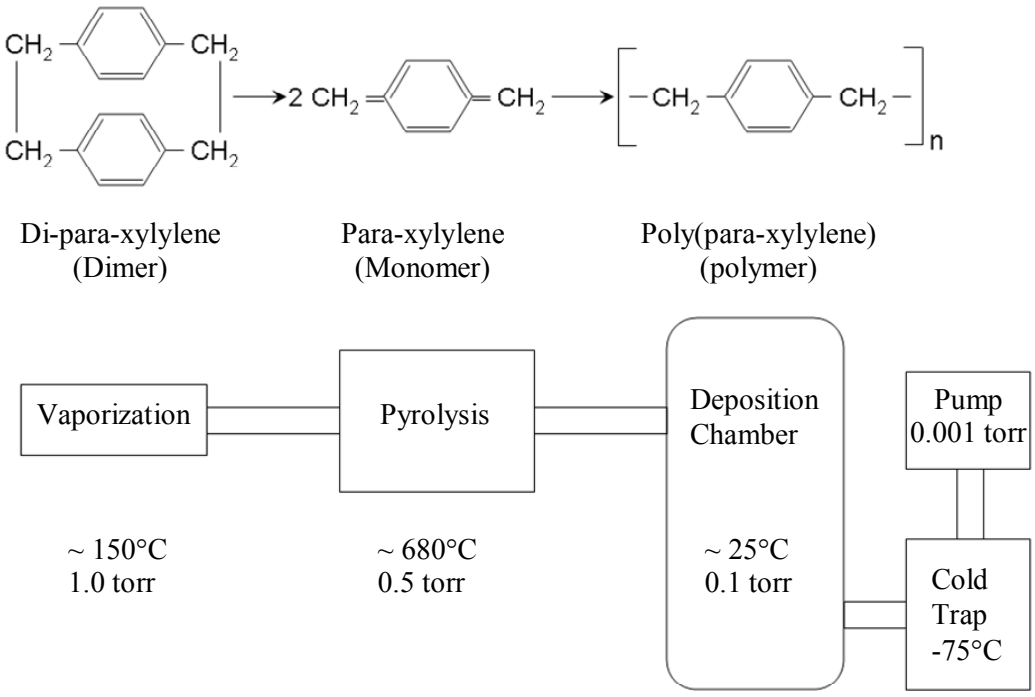

Figure 2.4 Chemical vapor deposition of parylene.

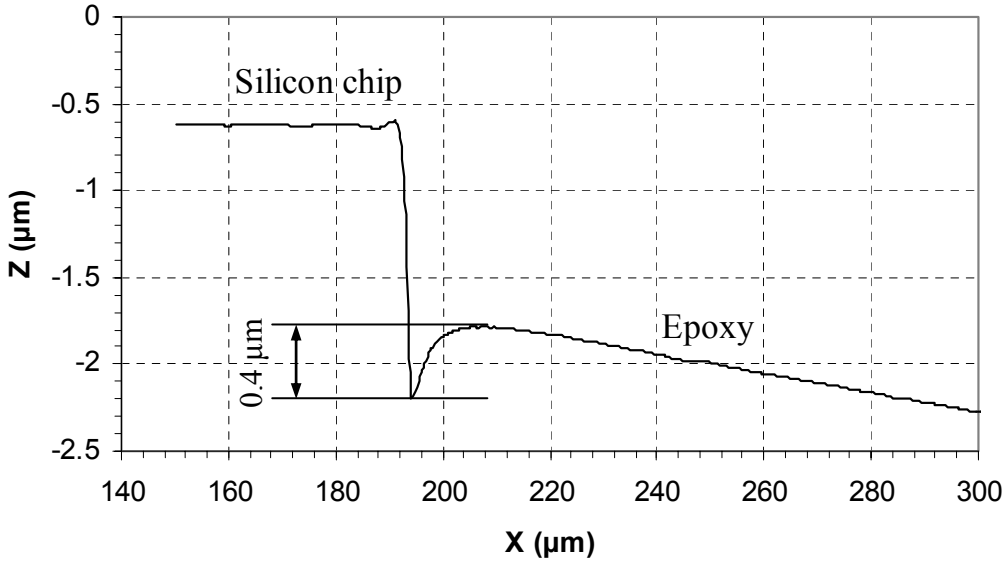

(a)

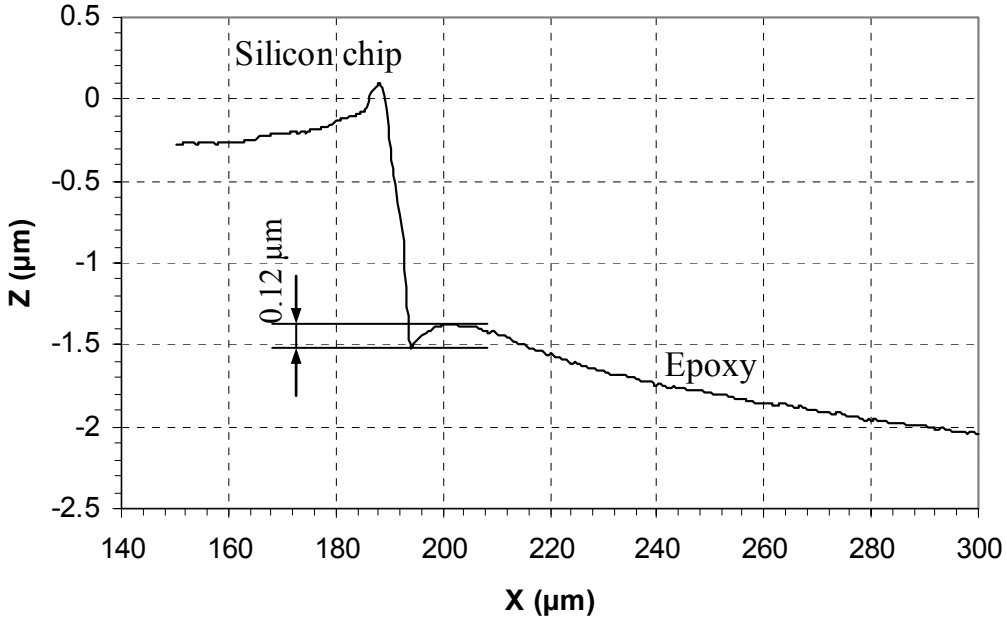

(b)

Figure 2.5 Surface profiles of silicon/epoxy interfaces (a) before parylene coating and (b) after parylene coating.

2.3 Electrical Interconnection Formation

After the parylene layer was patterned, additional Cr (200 Å) and Au (5000 Å) layer were deposited and patterned to provide interconnections from bond pads on the silicon chip to connection pads on the polymer substrate. The Cr and Au layer were deposited by sputtering, since sputtering can provide better step coverage than thermal or e-beam evaporation. In addition, the adhesion of sputtered films to the polymer substrate tends to be significantly better than evaporated films. The Cr/Au layer can also be used for other functions, for example to form integrated resistive temperature sensors and microheaters for temperature measurement and control. Figure 2.6 shows SEM images of the parylene layer bridging the gaps between sensor chip, epoxy and polycarbonate interfaces, and the Cr/Au interconnection crossing these gaps. Using the previously described integration approach, the epoxy-PC interface is extremely flat, with no discernable gaps or trenches following parylene refill, allowing metallization to readily bridge the interface for thermal control and sensor monitoring of the chip. After the Cr/Au was patterned, conductive epoxy was applied at the interconnection pads to provide electrical access to the system.

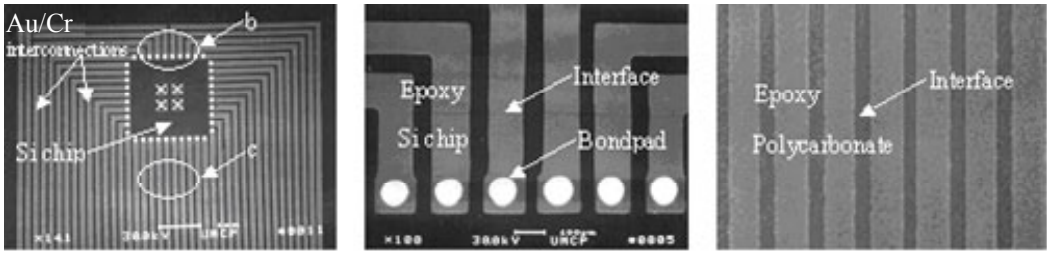

(a) (b) (c)

Figure 2.6 SEM images of gas sensor chip integrated into polycarbonate wafer: (a) gas sensor chip integrated into polycarbonate wafer with aluminum interconnections;

(b) polyimide layer bridging the gap between sensor chip and epoxy interface; and (c) polyimide layer bridging the gap between epoxy and polycarbonate interface.

2.4 Microchannel Fabrication

2.4.1 Hot Embossing

As described previously, polymers offer numerous advantages over other substrates, such as glass or silicon, for microchannel fabrication. Many methods of fabricating microchannels on polymer substrates have been reported [10, 16, 35, 36]. One of the most widely used replication processes to fabricate channel structures for polymer-based microfluidic applications is hot embossing. Upon heating above a characteristic glass transition temperature (T_g), polymers enter a viscoelastic rubbery state. This property is exploited in the embossing process. The microfabrication process of hot embossing itself is rather straightforward. Briefly, the polymer and embossing master are heated to a temperature just above the polymer's T_g, and the polymer substrate and master are brought into contact with controlled pressure. After pressing the master into the polymer, the assembly is cooled just below T_g and pulled apart [37].

Details of the hot embossing process used in this work is as follows:

- Substrate is off-gassed under vacuum at 100 °C overnight to dehydrate the polymer. If water vapor is present, it will be released during hot embossing and cause bubbles in the polymer substrate.
- Load the substrate into the press with the plattens 10 °C above T_g.

- Apply minimum pressure for 5-10 sec
- Apply imprint pressure for 5 min
- Apply minimum pressure as the plattens cool to 7 °C bellow T_g.
- Release

The highest quality embossing molds are generally metal made with the LIGA or UV-LIGA processes, and plasma-etched silicon. Unfortunately the LIGA and plasma-etched silicon processes are expensive. Direct embossing using high aspect-ratio photoresists such as SU-8 has also been demonstrated, but the resulting templates can be relatively fragile, and exhibit short lifetimes. Wet-etched silicon templates are commonly used for polymer embossing, which has been examined previously [16]. Silicon is an attractive template to use, since its properties and application have been highly characterized through integrated circuit fabrication and MEMS techniques.

The fabrication process of the wet-etched silicon templates used in this study is as follows. A 4" silicon wafer <100> with 2 μm oxide layer was used to make embossing template. A layer of photoresist (AZ5214) was spin-coated over the surface of the oxide and subsequently exposed to UV light through the transparency image aligned to the wafer flat. The photoresist was then developed, revealing the transferred image. In this step, all photoresist was removed except for that in the area defining the microchannels. The wafer was then placed in buffered oxide etchant solution to etch the exposed oxide layer. After a thorough rinse with DI water, the photoresist was removed with acetone. The remaining oxide layer was used as a mask

for anisotropic etching of the silicon wafer. The silicon wafer was etched in KOH for 4 hours at 75 °C. Silicon was etched in all areas surrounding the channels, and the resulting structure was a raised three-dimensional image of the channels. This embossed structure was then used to imprint the device image into the polymer substrate.

2.4.2 Replica Molding

Replica molding is simply the casting of prepolymer against a master and generating a negative replica of the master. PDMS is an excellent material for the fabrication of microfluidic structures by replica molding. The fabrication process is shown in Figure 2.7. First, PDMS was poured onto the master. After it was cured for 2 h at 60 °C in a convection oven, the replica was peeled off from the master. Holes were punched into the end of the microchannels to form fluid reservoirs. The replica can be simply placed on a flat surface to form the sealed microchannel. This sealing is reversible, but it does not withstand high pressures (> 5 psi). Exposing a PDMS replica to oxygen plasma introduces polar groups on the surface. This plasma treatment can help form tight and irreversible seal to the surfaces of a number of materials: PDMS, glass, silicon, SiO_2, quartz, silicon nitride, polyethylene, polystyrene, and glassy carbon. But this method does not work with all polymers. A thin layer of partially cured PDMS can be used as adhesive layer to bond PDMS microchannels to the polymer substrates.

The masters for replica molding can be fabricated by many techniques including etching in silicon, electroplating metal, patterning SU-8, or conventional machining of other hard materials. The composition of the masters used in production may depend on the production run. When the production run is large, metal or other hard materials may be used because of their durability. For fabricating new device or limited production run, metal and silicon molds are expensive and time consuming. In this case, SU-8 can be used to make replica mold, due to its ease of fabrication.

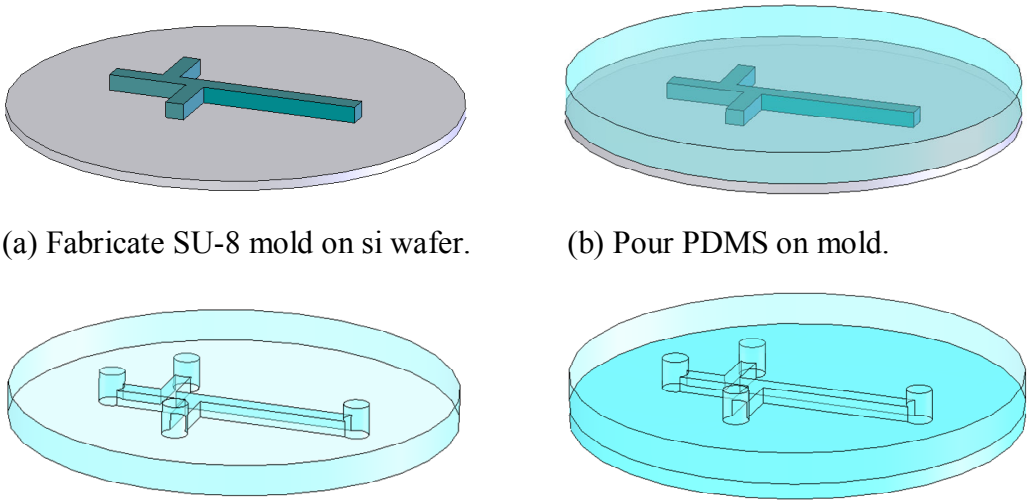

(a) Fabricate SU-8 mold on si wafer.

(b) Pour PDMS on mold.

(c) Cure PDMS and peel it off. Punch out reservoirs.

(d) Seal on the bottom polymer wafer.

Figure 2.7 PDMS micromolding process.

2.4.3 Optical Lithography in Deep Photoresists

Polymer microchannels also can be made by directly patterning a photosensitive polymer material such as polyimide and SU-8 [11]. SU-8 is epoxy-based negative photoresist, and standard formulations are offered to cover a wide range of film thicknesses from < 1 μm to > 200 μm. SU-8 has high optical transparency in the

visible range, and is sensitive to near UV radiation. Images having exceptionally high aspect ratios and straight sidewalls are readily formed in thick films by contact-proximity or projection printing. Cured SU-8 is highly resistant to solvents, acids and bases and has excellent thermal stability. These properties make SU-8 to be an excellent material for high aspect ratio microstructures.

An approach [38] for fabricating SU-8 microchannels on polymer substrate with embedded silicon chips has also been used in this study. The fabrication process is shown in Figure 2.8. Briefly, the first SU-8 layer is spin-coated, pre-baked, exposed, post-baked and developed to form microchannels on substrate embedded with silicon chips. The second thin SU-8 layer is spin-coated and pre-baked on another polymer or glass wafer. The two wafers are bonded at 50°C with manually applied pressure. After the bonded stack cools to room temperature, the second SU-8 layer is exposed through the second wafer. Finally, the stack is post-baked with temperature ramping while applying pressure. Using this approach, the microfluidic network with high aspect ratio and very good channel sealing can be formed on the polymer substrate embedded with silicon chips.

However, SU-8 has a rather large internal stress once developed, and is very hard to remove from the substrate. The developer for SU-8, PGMEA (propylenglygol-monomethylether-acetate), is intended to attack some polymers, such as PC, PMMA and epoxy. These disadvantages limit its application in this work.

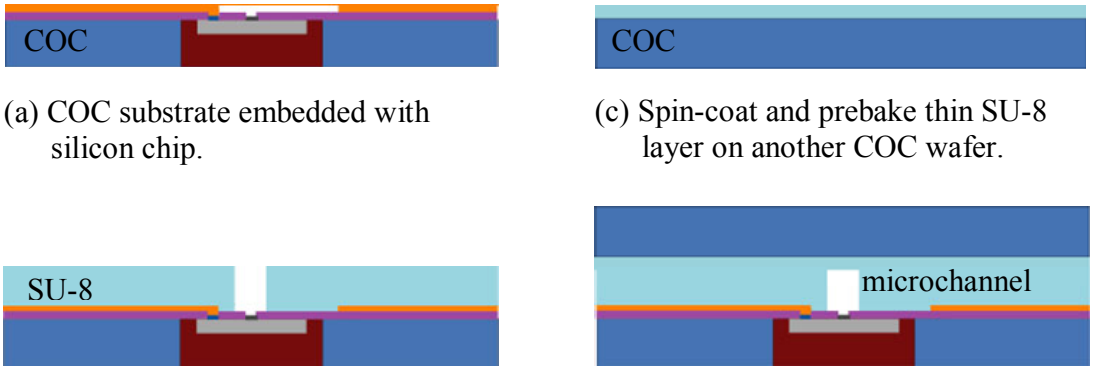

(a) COC substrate embedded with silicon chip.

(c) Spin-coat and prebake thin SU-8 layer on another COC wafer.

(b) Spin-coat, prebake, expose, postbake, and develop SU-8 to form microchannel.

(d) Bond the two wafers together.

Figure 2.8 Fabrication process of fabricating SU-8 microchannel on COC substrate embedded with silicon chip.

In summary, the silicon-in-plastic microfabrication involves integrating individual microfabricated silicon chips into a larger polymer substrate, where the silicon components provide functionality, and the plastic substrate provides system-level fluid handling. This technology leverages low-cost plastics for the large substrate, while limiting the high-cost silicon components to small chips which are seamlessly integrated into the plastic substrate. The silicon-in-plastic microfabrication technology provides an excellent fabrication platform for realizing the desired LOC or μTAS devices, using low-cost polymer substrates and simple polymer process techniques which are amenable to mass production. Two applications of the process are explored in this dissertation, as detailed in the following chapters.

Chapter 3

A Water-Based Chemical Monitoring System Using Silicon-in-Plastic Microfabrication Technology

3.1 Introduction

3.1.1 Monitoring System for Detection of VOCs in Water

There is a growing concern regarding the quality of water supplies, which are susceptible to both natural and man-made chemical contamination. Contamination by volatile organic compounds (VOCs) is of particular concern due to the potential for significant negative effects on human health. Many VOCs can cause potentially serious health effects, such as liver or nervous system problems, reproductive difficulties, and increased risk of cancer. For example, benzene causes aplastic anaemia and polycythaemia; dichloromethane produces carboxyhaemoglobin; toluene, styrene, trichloroethylene, tetrachloroethylene and dchloromethane are neurotoxic; styrene also produces mucuous membrane irritation [39]. The U.S. Environmental Protection Agency (EPA) currently sets maximum contaminant levels for safe

drinking water on 53 VOC contaminants. These VOCs arise mainly from combustion sources and motor vehicles, storage, distribution and transport of fuel, the oil and chemical industry, land fills and hazardous waste activities, metal industries, food and drink manufacturing, and agriculture [39].

A variety of detection methods have been applied for water analysis, such as gas chromatography/mass spectrometry (GC/MS), liquid chromatography/mass spectrometry (LC/MS), surface-wave acoustic sensors, and optical instruments [40-43]. But most of them rely on labor-intensive sample collection and laboratory analytical methods, which limits the quality, quantity, and frequency of data collected. For example, Looney and Falta [44] reported that the Department of Energy (DOE) Savannah River Site requires manual collection of nearly 40,000 groundwater samples per year, which can cost between $100 and $1000 per sample for off-site analysis. In addition, the integrity of off-site analyses can be compromised during sample collection, transport, and storage. Volatile organic compounds that are intended to be collected and analyzed may evaporate if the samples are exposed to the atmosphere when they are handled or stored. The concentrations measured using these ex-situ methods can therefore be lower than actual in-situ concentrations [40]. These factors have led to a need to develop new technology for in-situ VOCs monitoring of water systems that is highly sensitive, selective, and compact. In addition, the ideal technology would also be highly automated, low cost, and low power with potential applications to long-term distributed monitoring systems.

Several efforts have addressed the development of such sensing systems. For example, researchers at Sandia National Laboratories have developed an in-situ chemiresistor sensing system for real-time detection of VOCs in soil and groundwater, which employs an array of polymer-based microsensors (chemiresistors) packaged in a waterproof but vapor permeable housing designed to protect the sensor from the water-saturated conditions [40]. Ho et al. reported a surface acoustic wave (SAW) sensor for in-situ monitoring of VOCs in 2003, which consists of an input transducer, a chemically adsorbent polymer film, and an output transducer on a piezoelectric substrate [45]. The input transducer launches an acoustic wave that travels through the chemical film and is detected by the output transducer. A water-proofed package was designed for this SAW sensor to allow it to be used in water-saturated environment. Kohler et al. reported a test method which employs the commercial tin dioxide semiconductor gas sensor element in an immersion probe behind a gas permeable membrane for identification and quantitative determination of volatile organic solvents in water using the example five-component system ethanol, toluene, benzene, acetone, and ethylacetate [46]. Recently Vancura et al. reported a method to detect VOCs in liquid samples using a fully integrated CMOS resonant cantilever [47]. These cantilevers were coated with thin chemically sensitive polymer layers, and they were excited at their fundamental resonance frequency and acted as frequency-determining elements of the integrated feed back loop. The physisorption of VOCs in the sensitive polymer layer led to an increase of the cantilever mass, which caused a decrease of the cantilever resonance frequency. Electronic Sensor Technology (EST), a Division of Amerasia Technology Inc., developed a portable,

highly sensitive, rugged, vapor detector system (Model 4100 Trace Vapor Analyzer) which provides accurate vapor detection and analysis. This device utilizes a piezoelectric surface acoustic wave (SAW) resonator device coupled with capillary gas chromatography for detection. A similar microscale gas chromatography system for biomedical and environmental monitoring applications was also reported recently by Lu et al [48]. However, these devices rely on passive transport of gas from a water source, and do not support higher levels of integration for water delivery or vapor pressure control. Furthermore, the performance these devices was impacted by environmental temperature fluctuations.

3.1.2 Microsensors for VOCs Detection

In order to monitor the water supplies, sensing systems capable of measurement and analysis of VOCs are required. The key component of the sensing system is a microsensor which can be used to conduct identification and quantification of VOCs. Such microsensors fabricated using silicon technologies have been widely demonstrated for gas-phase organic solvent detection [39, 45, 49, 50]. Microsensors for VOCs detection may be categorized into four general groups: (1) chromatography and spectrometry; (2) electrochemical sensors; (3) mass sensors; and (4) optical sensors [41]. The categorization of these sensors is based primarily on the principal physics and operating mechanisms of the sensors.

Chromatography and spectrometry Chromatography relies on the separation of complex mixtures by percolation through a selectively adsorbing medium, with subsequent detection of compounds of interest. Gas chromatography can provide

superior discrimination capabilities with excellent precision, sensitivity, and reproducibility. The size of gas chromatographers ranges from large bench-top systems to portable hand-held systems. But the majority of these devices are not yet amenable to real-time, in-situ applications, and some of the devices are very expensive.

Electrochemical sensors Electrochemical sensors detect electrical signal changes (e.g., resistance) caused by interactions between an electrical current and a chemical medium. For example, conductometric sensors, polymer-absorption chemiresistors, catalytic bead sensors, and metal oxide semiconductors are widely used for chemical monitoring.

Mass sensors Mass sensors typically absorb the chemical of interest onto a surface, and the device detects the change in mass. The detection can be accomplished through changes in acoustic waves propagated along the surface (SAW devices) or by actual bending or a change in shape of the device as mass is accumulated (micro-cantilever devices). These devices are very sensitive to the presence of various volatile and semi-volatile chemicals.

Optical sensors Optical sensors include fiber optical sensors, colorimetry, and infrared sensors. These sensors rely on changes in electromagnetic radiation (e.g., visible, infrared) to detect and identify the presence of chemicals. The sensitivity of these sensors to VOCs can be good. But their application in long-term monitoring still requires testing.

For water monitoring, the gas sensor for such a system must be able to reproducibly distinguish solvents from the ambient water vapor, classify the response as representing the presence of a particular solvent, water vapor alone, a mixture, or an unknown solvent, and quantify the concentration of any measured VOC. In addition, the sensor should be low cost, provide continuous real-time monitoring capabilities, and be operated with minimal supervision.

Metal oxide semiconductor gas sensors are suitable sensors for in-situ gas sensing applications because of their low cost and low power consumption. The conductometric gas sensing mechanism in metal oxide semiconductors has been the focus of numerous investigations since the proposal of Seiyama in 1962 [51]. The first metal oxide semiconductor gas sensor was developed by Taguchi in 1969 [52]. The sensing material of the Taguchi sensor is tin dioxide (SnO_2). Since then, a variety of metal oxide semiconductor gas sensors have been investigated and commercially manufactured as detectors or alarms for combustible gases and toxic gases. Today, Taguchi sensors have captured 96% of the metal oxide semiconductor gas sensors market and the revenue for them is estimated to be $14.2 million in 1996 [53].

In the early 1990s, the opportunities of silicon micromachining led to the fabrication of new types of microhotplate devices and arrays for gas sensing [54]. Significant research on the use of microhotplates as a platform for gas sensors has been performed by NIST researchers [54-61]. Thin film microhotplate gas sensors have been the subject of considerable research as they offer the promise of high sensitivity,

good selectivity, compactness, and low power operation, combined with the low cost through MEMS system-level integration. Although other semiconducting oxides have been explored, tin dioxide (SnO_2) remains the most widely used material for this class of sensors. Microhotplate gas sensors consist of one or more microhotplates on a silicon chip. Each microhotplate is an individual gas sensor which contains a polysilicon resistor for heating, a metal plate for heat distribution, a semiconducting SnO_2 sensing film, and metal contacts to the SnO_2 for measuring the conductivity of the sensing film. For the devices used in the present work, the size of each sensor is about 100 μm on each side. The microhotplate structure allows rapid heating and cooling, with a fast thermal time constant (about 1 ms). This feature allows temperature modulation to be used to enhance the chemical selectivity of individual elements through the monitoring of adsorption/desorption kinetics which can differ between various molecular species [60]. Specially structured nanoparticle films have also been used to enhance both sensitivity and selectivity of SnO_2 gas sensors. For example, the detection of methanol in air at concentrations as low as 10 ppb has been reported using microhotplate sensors with nanopartical SnO_2 films [58].

3.1.3 Integrated Microfluidic Gas Sensor

In the present work, we report the application of silicon-in-plastic microfabrication technology to the development of an integrated microfluidic gas sensor for the monitoring of VOCs in water supplies. Since the cost per unit area for silicon-based sensor fabrication is significantly higher than for the microfluidic substrate, the silicon-in-plastic fabrication method provides the ability to use no more than the

necessary silicon area, and thereby offers the potential to substantially reduce overall system fabrication costs. The microfluidic system provides the required fluid routing, while offering several advantages for efficient solvent extraction such as large specific interface area, large ratio between interface area and channel volume, and short diffusion distance and time [62]. Furthermore, microfluidic systems can readily support integrated microheaters to control the liquid and vapor temperature, and thereby enhance the solvent concentration delivered to the gas sensor chip.

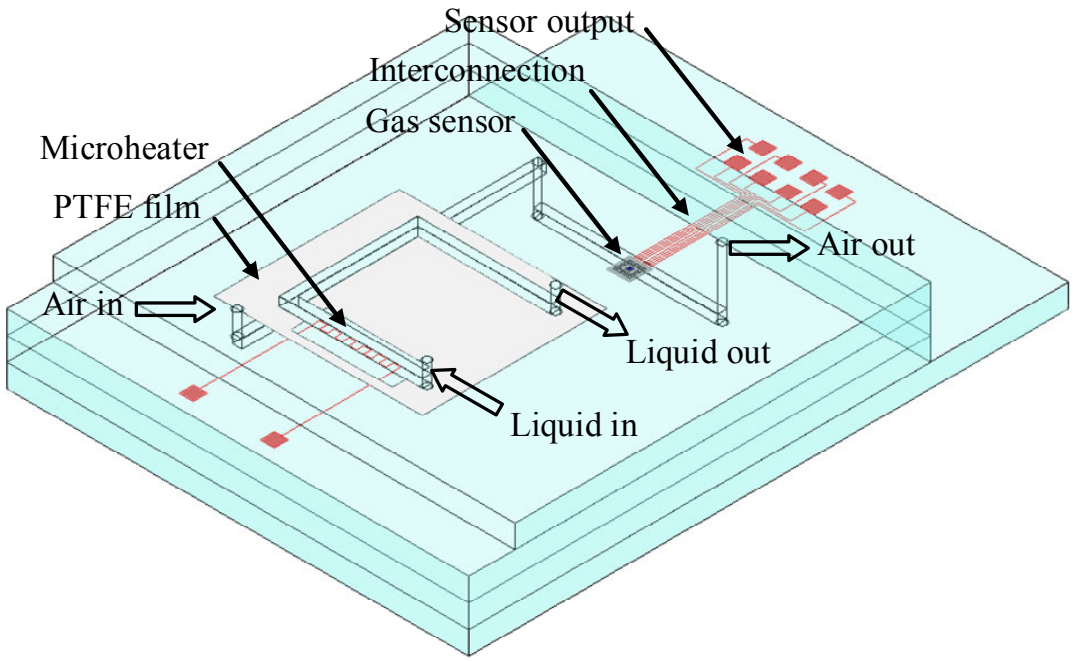

Figure 3.1 Device schematic of the water monitoring system.

The conceptual device schematic is shown in Figure 3.1. This device integrated microhotplate thin film gas sensor and polymer-base microfluidic network together. Compared to the precious water monitoring devices, it has the advantages of both the microhotplate thin film gas sensor and the polymer-base microfluidic devices.

3.2 Fabrication

3.2.1 Integration of Gas Sensor Chip into Polymer Substrate

The fabrication process, as outlined in Figure 3.2, is based on the fabrication process described in chapter 2. Briefly, a gas sensor chip is embedded into a polycarbonate plate using an epoxy (353ND, EPO-TEK) layer to level the exposed surfaces to within several microns. Parylene C is deposited as a passivation layer, while also serving to bridge small gaps which may occur between the sensor chip/epoxy/polycarbonate interfaces. Au/Cr layers are deposited and patterned to provide electrical interconnections and heaters for vapor pressure control. XeF_2 isotropic silicon etching is used to release the suspended microhotplates in-situ, after patterning of the parylene and Cr/Au layers. SnO_2 and TiO_2 sensing films are deposited on the microhotplates by chemical vapor deposition. The microfluidic network is formed in a second PC sheet by hot embossing and bonded to the substrate containing the sensor chip. Finally, conductive epoxy is applied at the connection pads through vias in the embossed sheet to provide electrical access to the system for vapor pressure control and microhotplate control and sensing. A photograph of a typical substrate fabricated using this approach is shown in Figure 3.3.

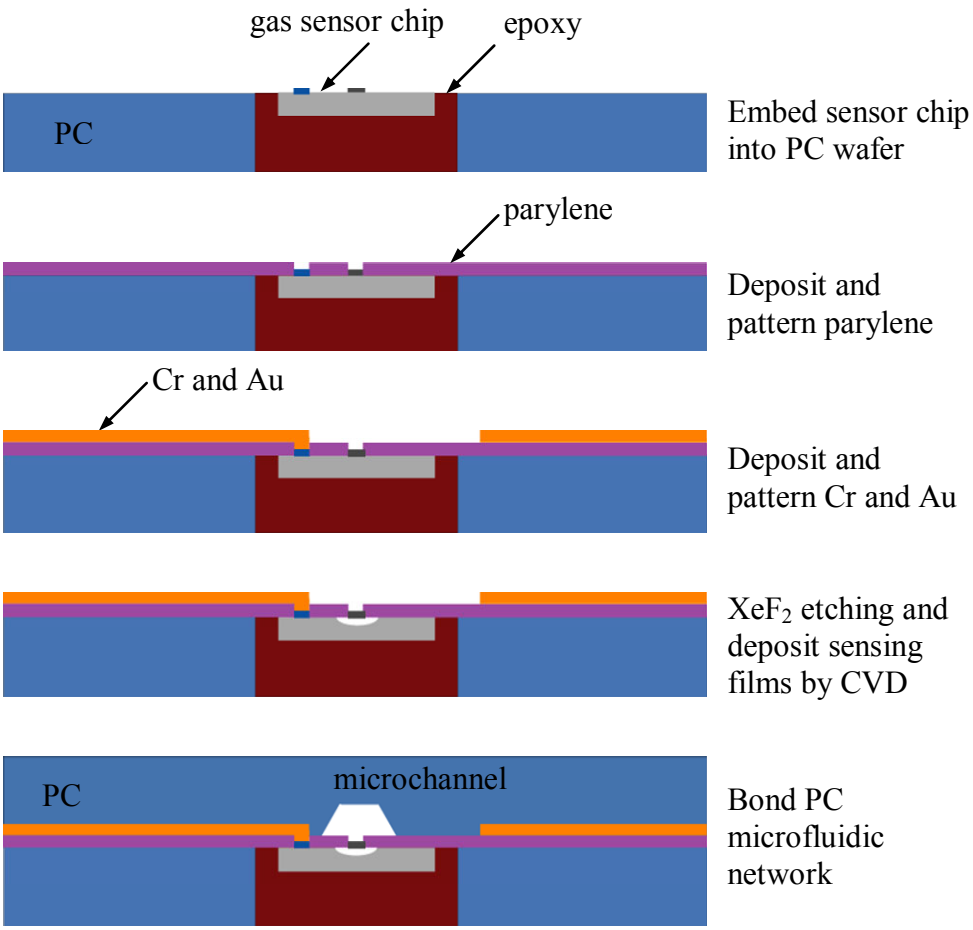

Figure 3.2 The fabrication process of the integrated microfluidic gas sensing system.

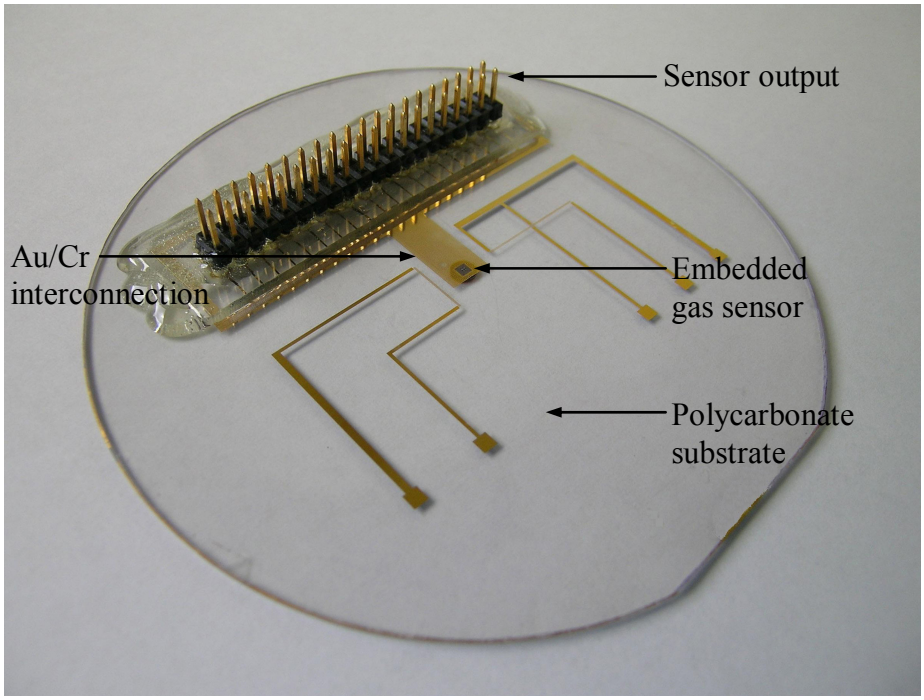

Figure 3.3 Photograph of a fabricated microfluidic substrate with integrated microhotplate gas sensor chip.

3.2.2 Sensing Films Formation

3.2.2.1 Microhotplate Structure

The integrated gas sensor chip used in this polymer system is a 4-element microhotplate gas sensor developed by NIST researchers [54]. Each chip is 1.6 mm square. A single microhotplate element is illustrated in Figure 3.4a. The most obvious features are the suspended plate, four support beams, and the etch pit. The device shown in Figure 3.4 also has four arrow-shaped top electrodes that are used for measuring the electrical characteristics (conductance) of deposited sensing film. The layer structure within the suspended plate, shown in Figure 3.4b, indicates other functionality within the basic microhotplate element. A serpentine polysilicon

element embedded in SiO_2 serves as a resistive heater. Above the heater, separated by an insulating layer of SiO_2, is a metal plate that serves to conduct heat (generated by applying a current through the polysilicon heater) more evenly across the device. The temperature coefficient of resistance of this metal plate can be calibrated to provide temperature measurements; similarly, one may extract a temperature from the measured polysilicon resistance. To provide for measurement of the electrical characteristics of sensing films, the surface electrodes directly contact the sensing film while being isolated from the heat distribution layer by a SiO_2 layer. The suspended microhotplates are typically ~100 μm across, with a mass of ~0.25 μg. The low mass of the suspended structure gives thermal time constants of a few milliseconds [54]. This property allows microhotplate gas sensors to be used in a temperature programmed sensing (TPS) operation mode, which can be used to increase selectivity of the sensor to different analytes.

The microhotplate platforms were manufactured at MIT-Lincoln Laboratory. The as-fabricated gas sensor chips are integrated into the PC substrate prior to the sacrificial release of the suspended microhotplate elements, since the released plate is easily damaged during the initial steps of the fabrication process. In-situ processing etching steps, which are performed at NIST, have been used to produce the suspended microhotplates. The etching steps involve various silicon etchants, including ethylene-diamine-pyrocatechol-water (EDP; anistropic) [63], XeF_2 (isotropic) [64], or tetramethyl ammonium-hydroxide (TMAH; anistropic) [65]. Among of these etching methods, EDP is a classic, but hazardous silicon etch, and it is not allowed in most

clean rooms [66]; TMAH is always used to produce the suspended structure at NIST, but it can damage the adhesion of parylene and cause the parylene layer peeled off; XeF2 etch is a non-plasma, isotropic dry etch process for silicon, and is suitable for post-processing CMOS integrated circuits [66]. In order to complete the microhotplate structure, XeF_2 isotropic silicon etching is used to produce the suspended microhotplates in-situ, after the parylene and Cr/Au layers have been patterned.

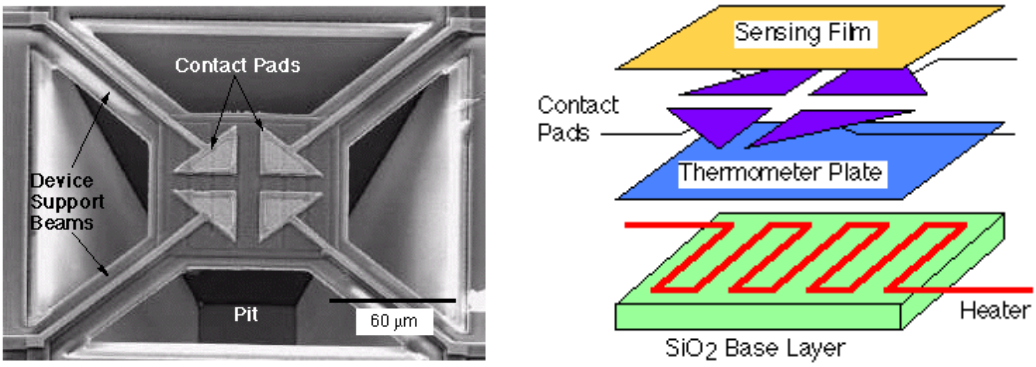

(a) (b)

Figure 3.4 (a) SEM image of a single on-chip microhotplate element, and (b) schematic of functional layers in a surface-micromachined microhotplate.

3.2.2.2 Sensing Films Formation

The sensing films of interest include oxides, metals and polymers. Typically, the films are deposited after silicon has been etched away to produce the thermally-isolated structures. A number of approaches have been used to deposit sensing

materials onto single microhotplate or arrays of microhotplate elements. These techniques utilizing local heating, local control of potential, lithography, and masking have been successfully demonstrated for registered deposition of SnO_2, ZnO, varied catalytic metals and polypyrole [59].

Chemical vapor deposition (CVD) has been used to deposit metal oxides on the microhotplates in a manner consistent with previous NIST microhotplate sensor work [56, 59]. The device was put into a low vacuum (milliTorr) system equipped with bubblers containing volatile precursor reagents. Titanium (IV) tetraisopropoxide (Aldrich) and anhydrous tin (IV) nitrate were the precursor materials used in the deposition of titanium oxide films and tin dioxide films, respectively. The finely powdered tin (IV) nitrate was stirred magnetically before each use in order to refresh the surface of the subliming precursor. The precursor was heated above room temperature to promote volatility. Following chamber evacuation, 10 mL/min Ar carrier gas was delivered through a bubbler bypass line until steady flow was achieved, after which the bubbler lines were opened and the bypass line closed, the precursor flow was allowed to equilibrate for 5 min, after which film growth commenced. Films of both oxides were grown on individual sensor element surfaces by heating the microhotplates to 375 °C while simultaneously monitoring film resistance. Growth times were typically from 5 to 10 min for SnO_2 and TiO_2 films, depending on the growth rate (monitored as function of film resistance), until SnO_2 films measuring on the order of 10 MΩ and TiO_2 films on the order of 30 kΩ were formed. Following film growth, the finished devices were removed from vacuum and

annealed at 400 °C in air for 30 min to complete film oxidation. Each device was produced with two equivalent SnO_2 sensor elements and two equivalent TiO_2 sensor elements in order to examine the reproducibility of film growth procedures and sensing performance. Representative examples of SnO_2 and TiO_2 films are shown in Figure 3.5.

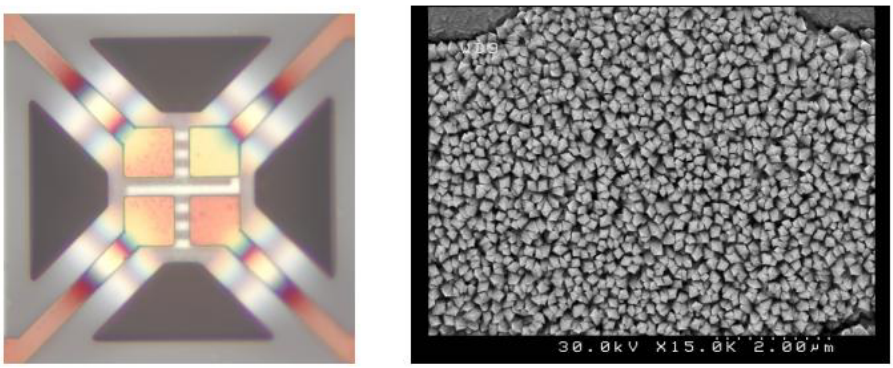

(a)

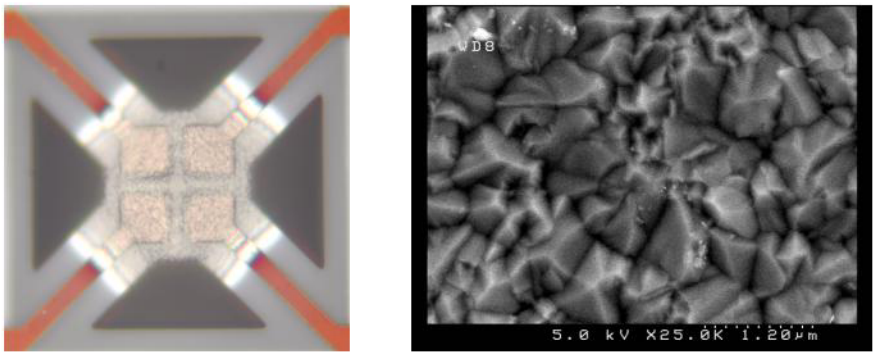

(b)

Figure 3.5 Optical (left) and SEM (right) images of (a) SnO_2 sensing film and (b) TiO_2 sensing film on a microhotplate.

3.2.3 Air-Liquid Two-Phase Flow

Gas-phase solvent extraction from the aqueous phase is a key requirement for the water monitoring system, since solvent sensing is ultimately performed in the gas-phase. In Clifford Ho's work, the sensor package is completely waterproof, but gas is allowed to diffuse through a GORE-TEX membrane that covers a small window to the sensor [40]. The NIST researchers did water vapor sensing using a gas bubbler. The water vapor can enter the airflow when dry air passed through water. Finally, the water vapor was delivered to the gas sensor by the airflow.

With the rapid development of microfabrication technology, solvent extraction can be carried out as chip-based technology. The advantage of the microspace for solvent extraction on a microchip is the scale merit of the small dimension itself, i.e., the large specific interface area, the large interface-to-volume ratio, the short diffusion distance and diffusion time [67]. Some solvent extraction systems on a microchip have been reported. Their difficulty is how to stabilize the interface of two fluids with a high specific interface area. Shaw and Ehrfeld reported a solvent extraction system where two microchannels fabricated on top and bottom plates made contact with a slight axis shift [67, 68]. Zhao and Aota reported a multistream flow system utilizing hydrophobic and hydrophilic patterning [69, 70]. Hibara, Sato, and Tokeshi reported a multiphase flow network which utilizes guide structure to stabilize the interface of fluids [71-73]. TeGrotenhuis reported a solvent extraction system using a porous polymer membrane to stabilize liquid/liquid interface [74]. This system utilized the hydrophobic property of the membrane to support the organic phase.

Air-liquid two-phase flow is also reported for disposable flow cytometer [75] and on-chip concentration of liquid samples [76]. However, to the best of our knowledge, no report has been done on on-chip solvent extraction by evaporation of the solvent in air-liquid two-phase flow microfluidic network. In this work, we demonstrated on-chip solvent extraction by evaporation of the solvent using an air-liquid two-phase flow system.

The architecture employed in this work consists of two micromachined channels separated by a porous membrane as shown in Figure 3.1. The design consists of two microchannels separated by a porous hydrophobic membrane. The microfluidic system was fabricated by hot embossing using a bulk-etched silicon template to form microchannels in the surfaces of two separate 1.5 mm thick polycarbonate (PC) substrates. The resulting microchannels are trapezoidal in cross-section and approximately 100 μm deep with a width at half-depth of 640 μm. A straight microchannel was fabricated in an upper PC layer, and a U-shaped microchannel was fabricated in a middle PC layer. A 50 μm thick polytetrafluoroethylene (PTFE) membrane with 70% porosity and 0.22 μm average pore size was thermally bonded between the upper and middle PC layers, creating a porous interface where the channels overlap. A close up picture of this PTFE membrane is shown in Figure 3.6. This membrane is highly hydrophobic, and compatible with strong acids and aggressive solvents. Next, a bottom PC layer was bonded to the composite structure using solvent bonding. The bottom PC layer contains a microchannel on the exposed

side, which is in fluid connection with the straight channel in the upper PC layer by aligned two 1.5 mm diameter holes premilled at the end of the middle and bottom microchannels before bonding.

This microchannel is used to deliver gas to the microhotplate sensor chip. The 3-layer PC microfluidic assembly was assembled using thermal and solvent bonding. However, the embedded sensor chip can be damaged by pressure and solvent, and thus the substrate containing the chip cannot be bonded to the 3-layer PC composite using these methods. Instead, the 3-layer structure was fixed to the bottom substrate containing the silicon sensor chip by mechanical clamping, with the microchannel in the bottom of the 3-layer structure aligned over the sensor elements. In the final assembly, the upper U-shaped channel delivers a continuous stream of water which passes over the middle microchannel with the PTFE membrane preventing the aqueous solution from entering the middle channel. Due to its native vapor pressure, solvent within the water passes through the membrane in the gas phase. A continuous flow of dry air is supplied to one end of the middle channel, which delivers the solvent to the gas sensor through the channels in the middle and bottom PC layers. A photograph of a fabricated water monitoring device using this approach is shown in Figure 3.7.

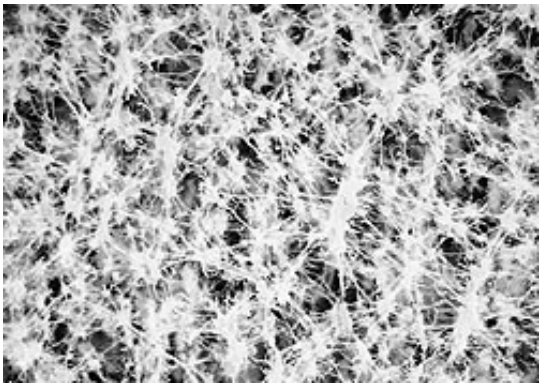

Figure 3.6 Device SEM image of PTFE membrane.

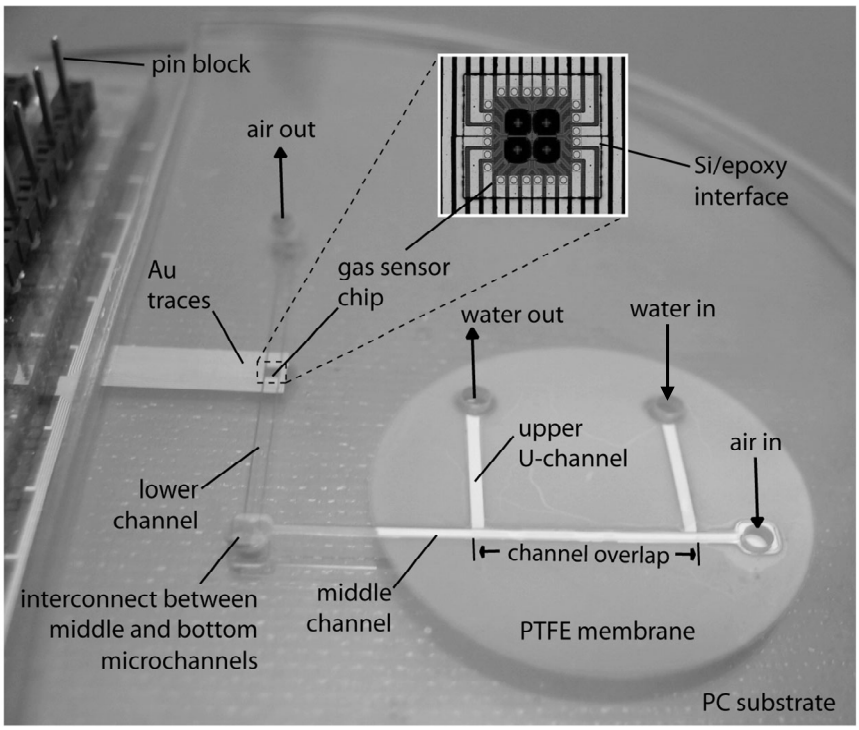

Figure 3.7 Photograph of a fabricated water monitoring device using silicon-in-plastic microfabrication.

3.3 Vapor Transport Model

3.3.1 Vapor Transport Model

In order to optimize the design of the air-liquid two-phase flow system, a vapor transport model is required. The theoretical performance of the air-liquid two-phase flow system, in which two fluids flow through microchannels separated by a porous PTFE membrane, can be determined by solving the convective-diffusion equations. Because the widths of the channels are much larger than the heights, sidewall effects may be neglected and the problem is reduced to two dimensions. Similar problems were considered and modeled in previous work. Yuan et al. reported an evaporation model of a thin liquid film [77], and TeGrotenhuis et al. reported a model of a microchannel contactor having two immiscible fluids flowing through rectangular channels separated by a porous plate [74]. A simple 2-D model of the vapor transport system is shown in Figure 3.8. The geometry is divided into three sections, liquid flow channel, air flow channel, and the porous membrane. Each section has its own transport equation with boundary conditions that allow the equations to be combined into a single mathematical model of the overall device.

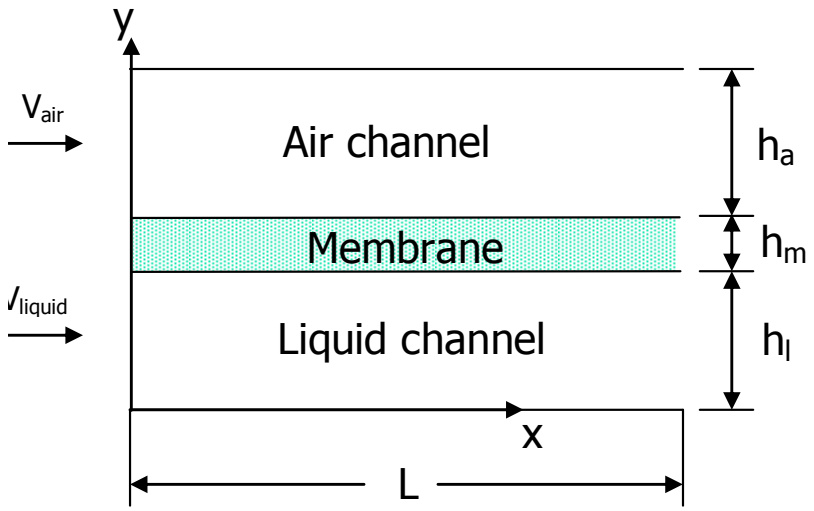

Figure 3.8 Air-liquid two-phase flow device geometry.

The air and liquid flow fields can be considered two-dimensional, steady, incompressible, and low Reynolds number flows, along two parallel microchannels. There is no flow along the length of the membrane, and no slip tangential to its surface. Dispersion in the flow direction is neglected in all three sections, because the liquid and air flow is much faster than dispersion of VOC molecules. To solve the velocity profiles of air and liquid flow, we recall the classical Navier-Stokes equation [78, 79]:

$$\frac{\partial \bar{u}}{\partial t} + \bar{u} \cdot \nabla \bar{u} = -\nabla P + F + \eta \nabla^2 \bar{u} \tag{3.1}$$

Where ρ is fluid density, $\bar{u}$ is the velocity field, P is the pressure, F is the body force, and η is the viscosity. The continuity equation is also applied:

$$\frac{d\rho}{dt} + \rho \nabla \cdot \bar{u} = 0 \tag{3.2}$$

We assume that the pressure is uniform across the height of each channel. For incompressible flow at low Reynolds numbers without a body force, the Navier-Stokes equation and continuity equation reduce to

$$\eta \nabla^2 \overline{u} = \nabla P \tag{3.3}$$

$$\nabla \cdot \overline{u} = 0 \tag{3.4}$$

By integrating equation (3.3) with no-slip condition, $u_{lx} = 0$ at $y = 0$ and $y = h_l$, we can determine the x-direction velocity profile for a rectangular liquid flow channel, $u_{lx}(x, y)$.

$$u_{lx} = \frac{3}{2} \frac{Q_l}{w h_l} \left(\frac{4y}{h_l} \right) \left(1 - \frac{y}{h_l} \right) \tag{3.5}$$

Where Q_l is the volumetric flow rate of the liquid, w is the channel width, and h_l is the height of the liquid flow channel. A similar velocity profile for the air flow channel is

$$u_{ax} = \frac{3}{2} \frac{Q_a}{w h_a} \left(1 - \left(\frac{2\left(y - h^*\right)}{h_a} \right)^2 \right) \tag{3.6}$$

where Q_a is the air volumetric flow rate, h_a is the height of the air flow channel, h_m is the thickness of the porous membrane, and $h^* = h_1 + h_a + h_m/2$. The liquid and air flows are plane Poiseuille flow, and the flow fields are simple two-dimensional parabolic flow profiles.

The general equation for Steady-Flow diffusion is

$$u_x \frac{\partial C}{\partial x} + u_y \frac{\partial C}{\partial y} - D \frac{\partial^2 C}{\partial y^2} = \dot{C}''' \tag{3.7}$$

Where C is the solvent concentration, D is the solvent diffusivity, and $\dot{C}'''$ is the rate of creation of solvent. Based on the assumptions stated above, there is no chemical reaction, then $\dot{C}''' = 0$. The gas molecule velocity in x direction is much larger than velocity in y direction, so that the transport term with the mean molecular velocity u_y can be neglected. The resulting mass transfer differential equations are

$$u_{lx} \frac{\partial C_l}{\partial x} = D_l \frac{\partial^2 C_l}{\partial y^2} \tag{3.8}$$

$$\frac{\partial^2 C_m}{\partial y^2} = 0 \tag{3.9}$$

$$u_{ax} \frac{\partial C_a}{\partial x} = D_a \frac{\partial^2 C_a}{\partial y^2} \tag{3.10}$$

for the liquid flow, the porous membrane, and the air flow respectively, where C is solvent concentration and D is solvent diffusivity for each of the respective phases.

Six boundary conditions are required for the three second-order differential equations. The air fills into the pores of porous membrane, because the PTFE membrane is very hydrophobic.

$$\frac{\partial C_l}{\partial y} = 0 \qquad \text{at} \quad y = 0, \tag{3.11}$$

$$D_l \frac{\partial C_l}{\partial y} = k\left(C_m\Big|_{y=h_l} - m_a C_l\Big|_{y=h_l}\right) \qquad \text{at} \quad y = h_l, \tag{3.12}$$

$$D_e \frac{\partial C_m}{\partial y} = D_l \frac{\partial C_l}{\partial y} \qquad \text{at} \quad y = h_l, \tag{3.13}$$

$$C_m = C_a \qquad \text{at} \quad y = h_l + h_m, \tag{3.14}$$

$$D_a \frac{\partial C_a}{\partial y} = D_e \frac{\partial C_m}{\partial y} \qquad \text{at} \quad y = h_l + h_m, \tag{3.15}$$

$$\frac{\partial C_a}{\partial y} = 0 \qquad \text{at} \quad y = h_l + h_m + h_a, \tag{3.16}$$

Where D_e represents an effective diffusion coefficient for the porous membrane that captures effects such as porosity and tortuosity. Equation (3.11) and (3.16) provide for zero flux through the solid channel walls. Equation (3.12) represents constant flux across the interface based on an interfacial mass transfer model. The parameter m_a is the equilibrium distribution coefficient which, for the present case of a liquid/air interface, is defined by the ratio of the equilibrium analyte concentration in the air channel to analyte concentration in the liquid channel at the liquid/membrane interface. This parameter is equivalent to the Henry's law constant for the solvent, which is a nondimensional constant defined as the ratio of partial pressure in the vapor phase to concentration in the liquid phase [80, 81]. The parameter k is an overall gas phase mass transfer coefficient defined by the mass transfer resistance across the liquid/air interface [81]. For the present case, k was assumed to be 0.1 cm/sec based on the mass transfer coefficient of six organic compounds with a Henry's law constant range from 3.33×10^{-7} to 3.67×10^{-3} to provided by Guo and Roache [82]. Equation (3.13) assumes continuity of flux on both sides of the liquid-air interface, and Equation (3.14) and (3.15) represent continuity and constant flux at the porous membrane on the air side.

The initial conditions for concurrent flow are

$$C_l = C_{l0} \qquad \text{at} \quad x = 0, \tag{3.17}$$

$$C_m = C_a = 0 \qquad \text{at} \quad x = 0. \tag{3.18}$$

The differential equation for the membrane is solved analytically to give a linear concentration profile through the membrane. Therefore, the partial derivative of concentration in the membrane can be replaced by

$$\frac{\partial C_m}{\partial y} = \frac{C_m\big|_{y=h_l+h_m} - C_m\big|_{y=h_l}}{h_m} \tag{3.19}$$

in the boundary conditions above, and the differential equation for the membrane, equation (3.9), is eliminated.

The two convective-diffusion equations for the air and water flow channels can be solved numerically using the Crank-Nicholson implicit method of finite differences [83]. The y-direction is nondimensionalized by the liquid channel height, h_l, and concentrations are nondimensionalized by the liquid initial concentration, C_{l0}. The x-direction is analogous to time and is nondimensionalized as

$$\tilde{x} = \frac{2}{3}\frac{D_l W}{Q_l h_l} x \tag{3.20}$$

A Sherwood number is defined for the interfacial mass transfer using liquid side diffusivity and liquid channel height for consistency,

$$Sh = \frac{D_l}{k h_l} \tag{3.21}$$

The other two diffusivities, D_a and D_m are scaled by the liquid diffusivity, D_l. The interfacial boundary condition, Equation (3.12), becomes

$$Sh\frac{\partial \widetilde{C}_l}{\partial \widetilde{x}} = \widetilde{C}_l\Big|_{\widetilde{x}=1} - m_s \widetilde{C}_m\Big|_{\widetilde{x}=1} \qquad \text{at} \quad \widetilde{x}=1 \tag{3.22}$$

The other boundary conditions are similarly nondimensionalized.

The effluent concentration of the flow is calculated by averaging over the flow profile at the end of the channel, which for the air flow becomes

$$C_{a-eff} = \frac{W}{Q_a}\int_{h_l+h_m}^{h_a+h_m+h_l} C_a(x=L)u_{ax}dy \tag{3.23}$$

This equation is nondimensionalized by the liquid influent concentration as well.

3.3.2 Numerical Solution Using Crank-Nicholson Implicit Method and Simulation Results Using FEMlab

A numerical simulation of effluent concentration was performed over a range of air and liquid flow rates for the case of methanol. Air and liquid diffusion coefficients of D_a = 0.159 cm^2/s and D_l = 1.9×10^{-5} cm^2/s [84] were used. The diffusion constant for methanol within the membrane, D_m, was estimated analytically using a model for gas diffusion in porous media [85].

$$D_m = D_a\varepsilon^{\frac{4}{3}} \tag{3.24}$$

where ε is the membrane porosity. Using this model with ε = 0.7 yields D_m = 0.079 cm^2/s. A 1 cm long, 100 μm deep intersection region was defined between the liquid and air microchannels. The results were normalized to the saturated vapor concentration of the liquid analyte as determined from the Henry's law constant for methanol, given on a mole fraction basis as 0.29 at 25 °C [86].

The air-liquid two-phase flow system with two different microchannel lengths has been simulated using FEMlab, as shown in Figure 3.9 and Figure 3.10. The simulation results of the air-liquid two-phase flow system with different air flow rates using FEMlab and Crank-Nicholson implicit method are shown in Figure 3.11. The deviation between FEMlab simulated results and the numerical results using Crank-Nicholson implicit method is less than 10% over the range of air flow rate.

As can be seen from section 3.1.1, the effluent vapor concentration of the air flow is dependant on several factors, such as the dimension of the microchannels, the air and liquid flow rate, the properties of the membrane, and the properties of the analytes. Based on the vapor transport model, these factors can be used to optimize system design to achieve the best performance. Of which the air and liquid flow rate can be easily controlled to change the effluent vapor concentration. Figure 3.12 gives the numerical results of effluent concentration with different air and liquid flow rate. As can be seen from Figure 3.12, the effluent vapor concentration is higher when the air flow is slower and the liquid flow is faster. But the liquid flow can not be very fast due to the pressure problems in the microchannel. The liquid can flow into the airflow channel through the membrane at higher flow rate. The detail of pressure control in microchannel will be described in section 3.4. Based on Table 3.1, the maximum liquid flow rate and minimum air flow rate were chosen to achieve the highest effluent vapor concentration. The channel length is another factor that can be modified to increase the effluent vapor concentration. The numerical results with different channel length are shown in Figure 3.13. The longer microchannel results in

higher effluent vapor concentration. However, very long straight microchannel is not acceptable due to the small dimension of the device. In order to make the microchannel longer to achieve higher effluent vapor concentration while keep the device small, serpentine channels can be fabricated in the air-liquid two-phase flow system. The properties of the analytes also can affect the effluent vapor concentration, such as Henry's Law constant and molecular diffusion coefficients of solvent in air and water. These parameters can be changed by changing the temperature of the analyte. In this design, an integrated microheater is used to control the temperature of the analyte flowing in the liquid channel to control the effluent vapor concentration in the air flow channel.

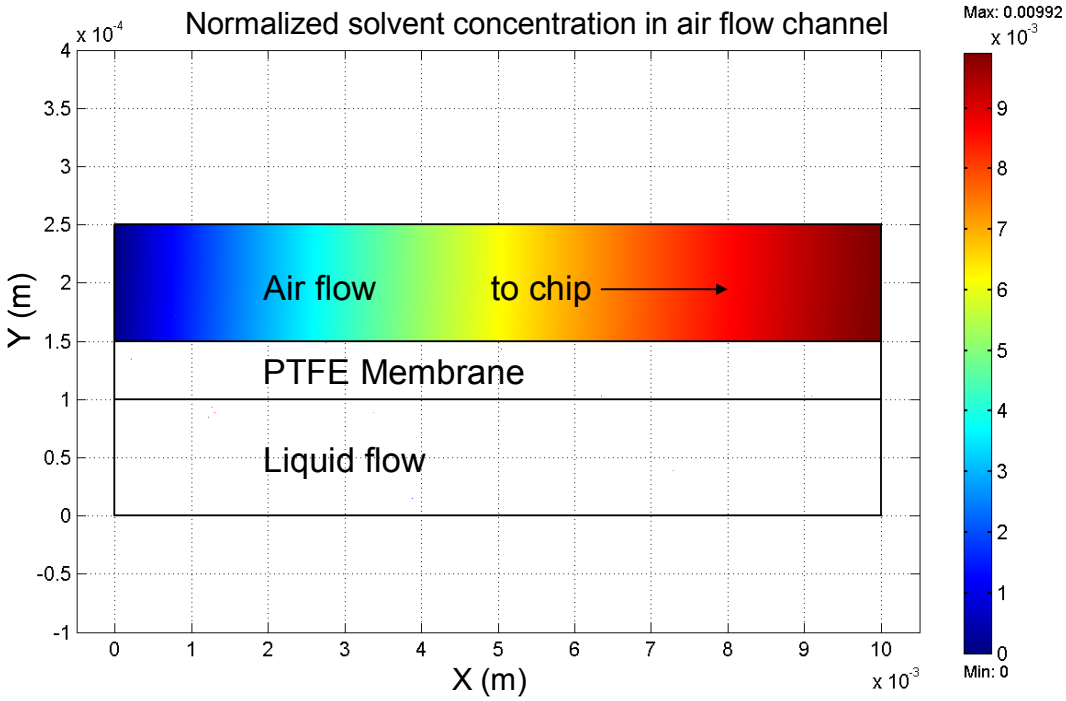

Figure 3.9 Simulation result for the air-liquid two-phase system with 1mm microchannel.

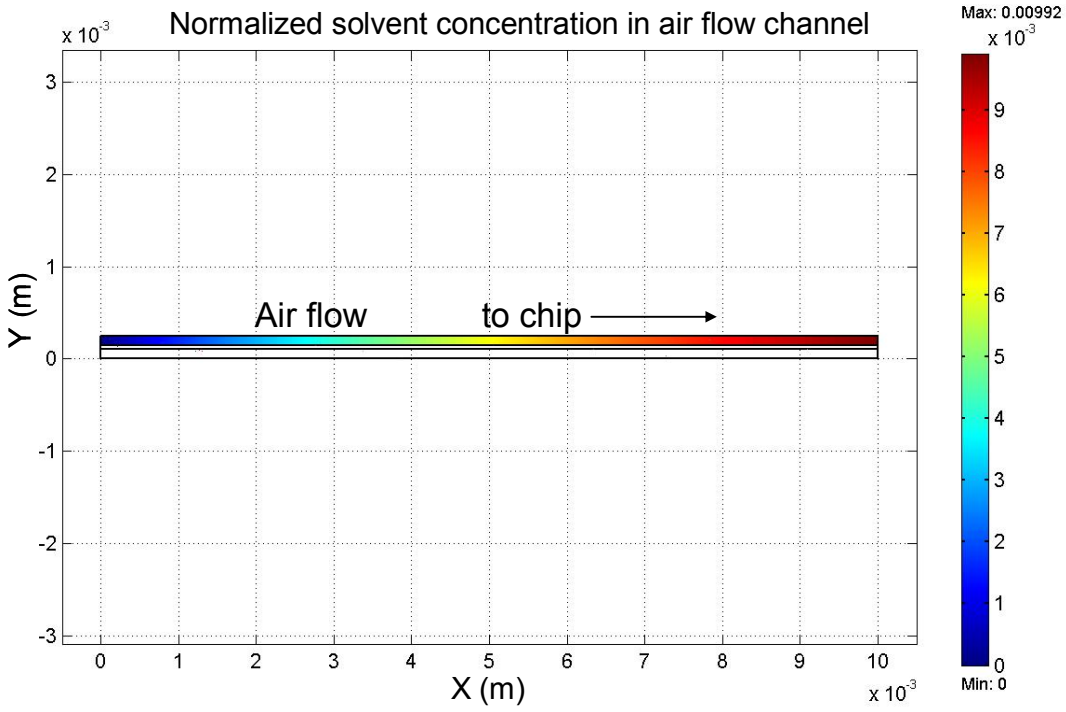

Figure 3.10 Simulation result for the air-liquid two-phase system with 10mm microchannel.

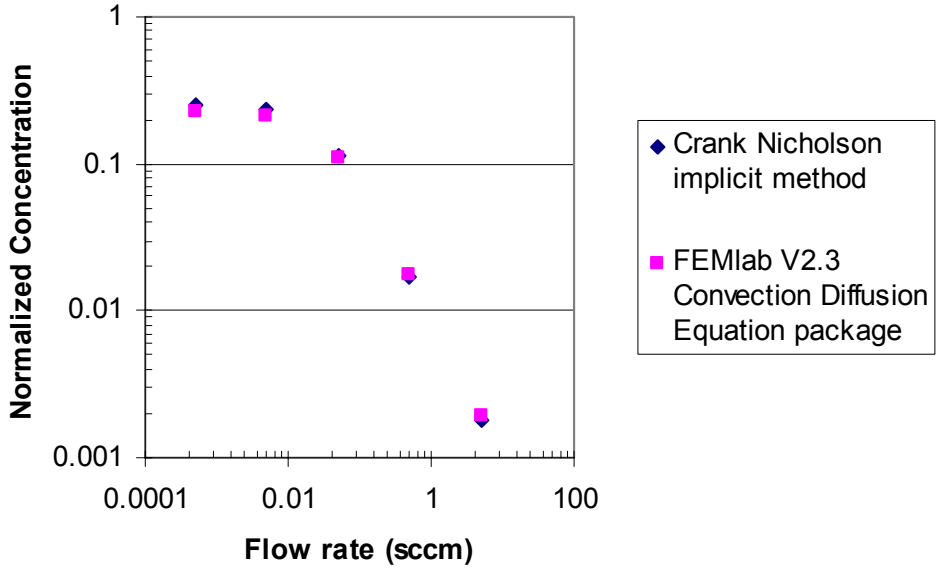

Figure 3.11 Simulation results for the air-liquid two-phase flow system with different air flow rates using FEMlab and Crank-Nicholson Implicit Method.

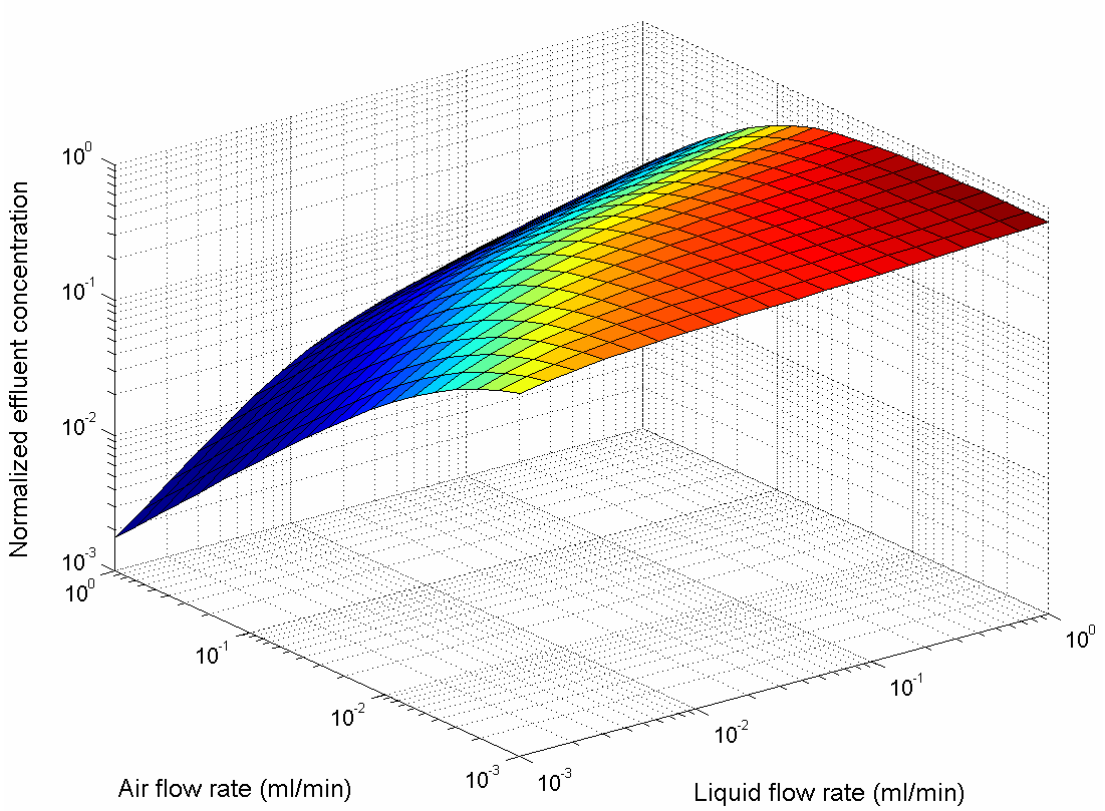

Figure 3.12 Numerical results of effluent concentration with different air and liquid flow rates.

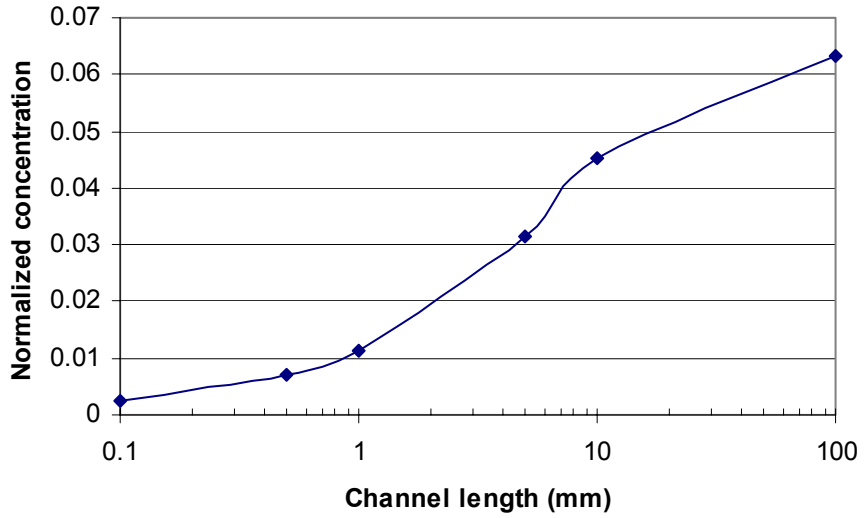

Figure 3.13 Simulation results for the air-liquid two-phase flow system with different channel lengths.

3.4 Experimental Results

3.4.1 Experimental Setup and Protocol

Testing of the water monitoring system for VOCs detection was performed at NIST. Delivery of gases to the microchannel of the device is computer controlled via a set of mass flow controllers and pressure-actuated valves. Two major types of experimental protocols were followed to test the sensors – fixed temperature sensing (FTS) and temperature programmed sensing (TPS). Both methods have been described in prior work at NIST [57, 58, 60]. During FTS, the sensor elements are monitored at a single temperature throughout the entire gas delivery program before sensor temperature is changed. The TPS program used in this work alternates the sensor temperature between a ramp value (from 60 °C to 480 °C in 29 equal steps) and a base value (200 °C) every 500 ms. In this way, 58 data points (29 corresponding to the ramp temperature and 29 to the base temperature) are collected for each sensor in 14.5 sec. After 5 sec at the base temperature, this temperature control pattern (Figure 3.14) is repeated throughout the analyte delivery program. For both FTS and TPS, a laptop computer is used to control the sensor temperature and measure the conductometric response of the gas sensor elements. This was accomplished through a signal conditioning unit which amplified the computer's analog-to-digital converter card voltages to the levels necessary to perform microhotplate heating for each device. The computer allowed for either FTS or TPS with separate heating profiles specified for each sensor element.

Figure 3.15 shows one complete FTS cycle for on-off exposures to methanol. The methanol was cycled through all three concentrations (25, 50, 100 ppm) at each temperature for four temperatures from 325 °C to 475 °C. Each sensor element exhibits a fast (on the order of second), low-noise, positive conductometric response when the analyte is introduced to the sensor element. The features shown here are typical of the sensors in this study, which exhibit conductance changes of up to an order of magnitude when exposed to the analyte concentration of 50 ppm. The baseline conductance of the SnO_2 films typically measures between 10^{-6} and 10^{-4} Siemens (S, equal to Ω^{-1}), while TiO_2 films conductance is far more variable from sample to sample (10^{-9} through 10^{-5} S). These substantial variations in baseline conductance can likely be attributed to a combination of events, including micro-variations in crystallite size, crack formation in identically produced sensing films, and variations in contact pad oxidation between sensors.

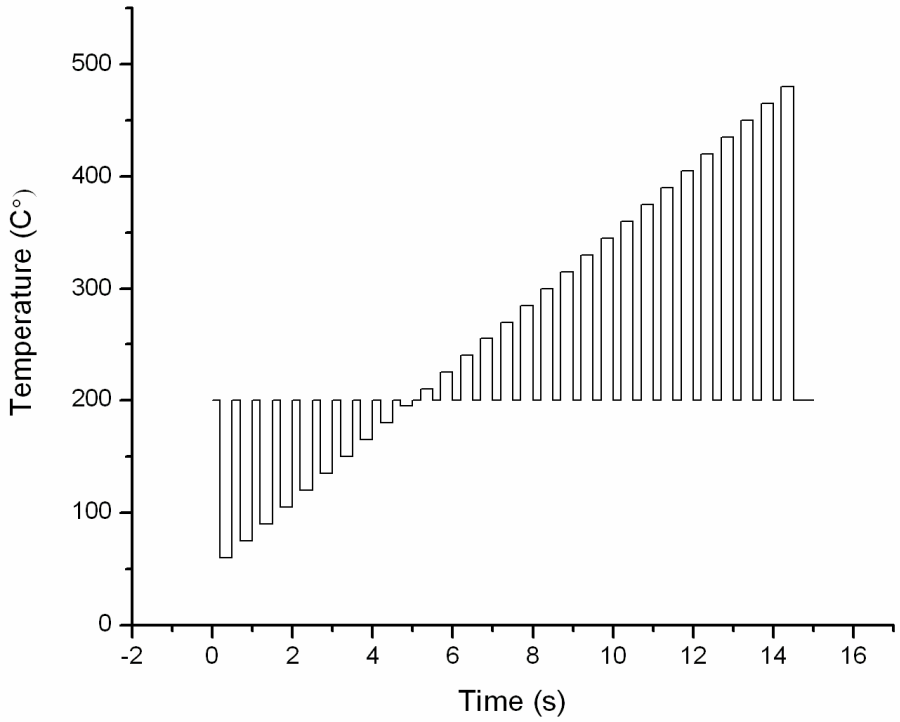

Figure 3.14 TPS temperature program.

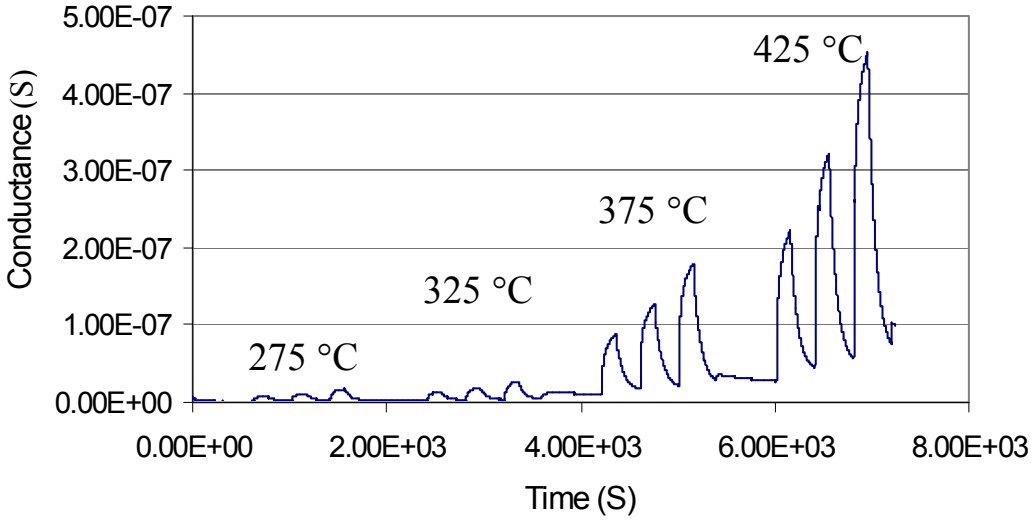

Figure 3.15 One complete FTS cycle for on-off exposures to 25, 50, 100 ppm methanol.

The equilibrium responses of the metal oxide films have been demonstrated to be non-selective due to the baseline drifting, but the transient (or kinetic) response is distinguishable. The temperature change in the hotplate element results in a transient response in the sensor films' conductance. The high structure specificity of kinetic information provides a basis for achieving identification as well as sensitivity by employing temperature programmed sensing (TPS) mode. Rapid temperature control (~1 ms time constants) of the microhotplate platform permits the collection of data containing mainly kinetic information [57, 60]. As described preciously, the TPS experiment sets the hotplate temperature to a ramp value between 60 °C and 480 °C for 200 ms, then returns to the baseline temperature (200 °C) for 300 ms, after which it applies the next ramp temperature. Figure 3.16a through 3.16d show a complete set of TPS signal traces for all two levels of analyte exposure and dry air. Each element is shown separately, as are the base and ramp temperature data. The patterns shown in Figure 3.16a through Figure 3.16d exhibit difference as concentration is increased. In some cases, these subtleties are difficult to discern with the unaided human eyes, but computer aided analysis can be used to identify these similar patterns. Recursive training and validation of artificial neural networks (ANNs) was used to both identify analytes and estimate their concentrations using the signal patterns in this study [87]. Another method for clarifying these patterns is to compute the time derivatives of the ratio of the data collected an each ramp temperature to the data collected at the corresponding base temperature. This treatment of the data also can reduce the effects of baseline drifting. In practice, a library of response patterns could be established,

the constant comparison of sensor response traces to the analytes library would allow the sensor to identify the presence of analytes and estimate their concentrations.

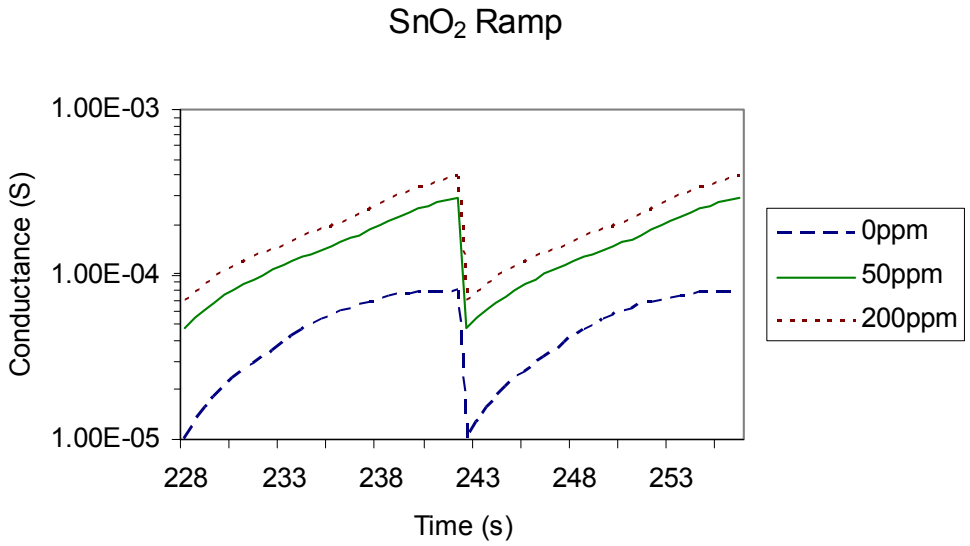

(a)

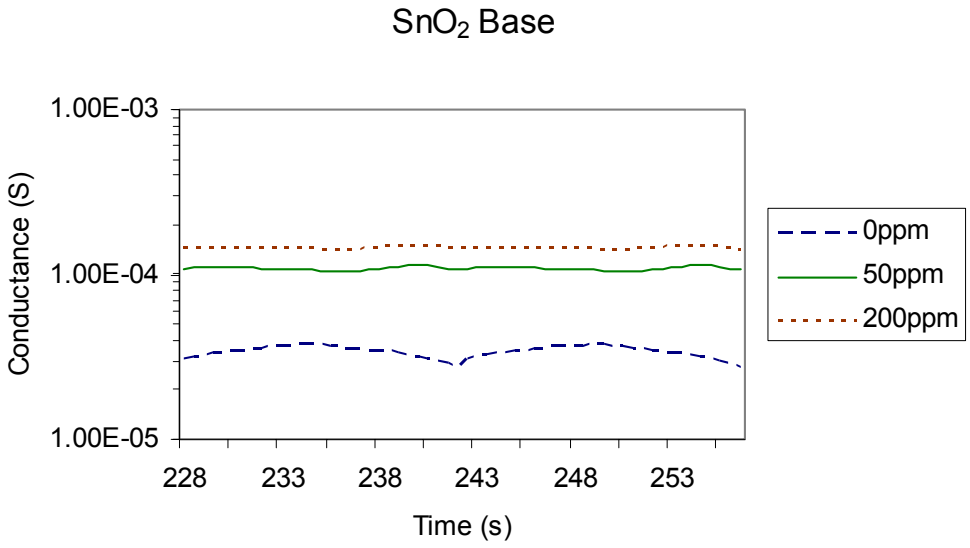

(b)

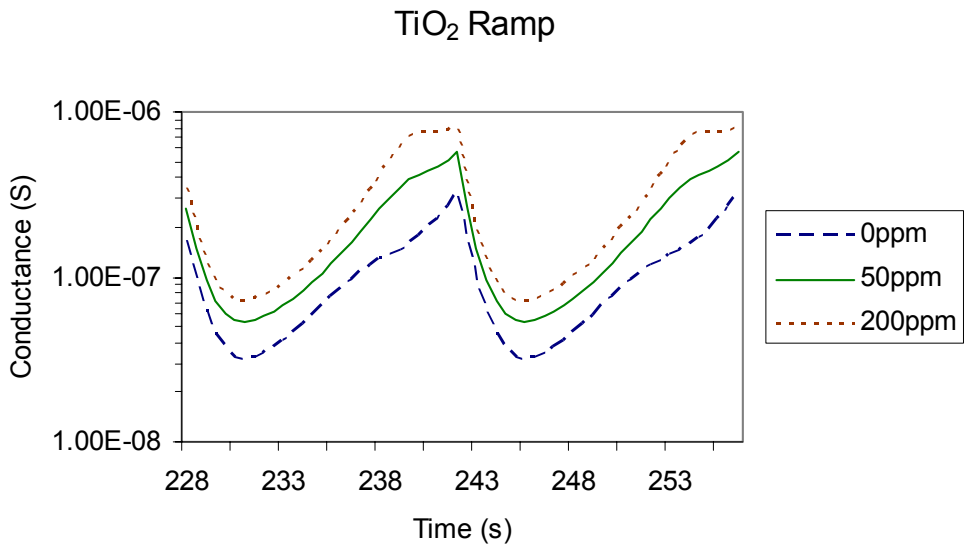

(c)

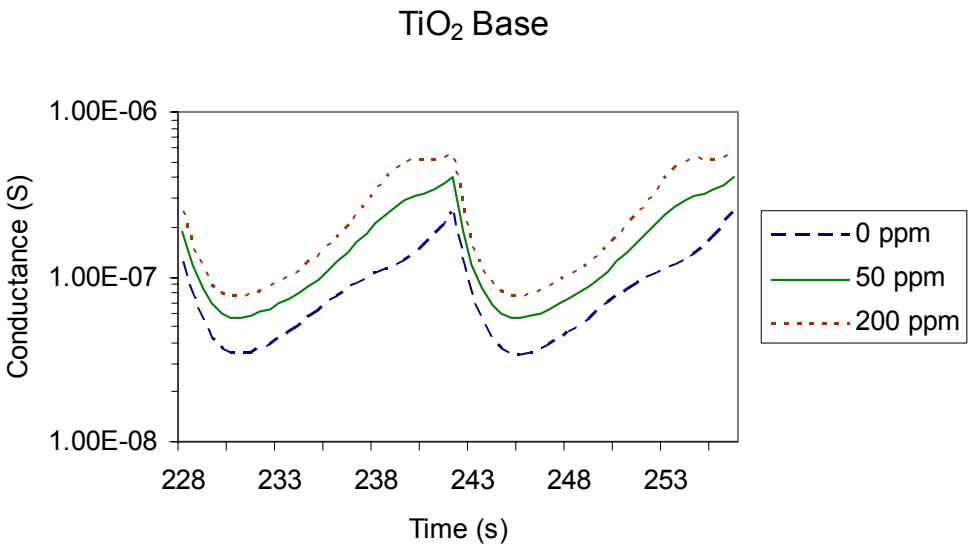

(d)

Figure 3.16 TPS traces (two cycles) for three tested concentrations of methanol exposure to SnO_2 and TiO_2 sensing films.

3.4.2 Characterization of Sensor Response at Different Flow Rates

All the sensing results shown in Figure 3.15 and Figure 3.16 were collected by performing FTS and TPS experiments using the integrated microfluidic gas sensor. The primary microchannel, which delivers the gas analyte to the sensor elements, is 800 μm wide, 120 μm deep and 2.8 cm long. The sensor elements are located in the center of the microchannel. Since the space velocity (related to the flow rate) of gas molecules can be precisely controlled in a wide range inside the microchannel, the relationship between gas flow rate and sensor response can be directly explored. The flow rate of the test gas may have some effects on the response of the microhotplate gas sensor since it may affect the heat and the mass exchange at the sensing film. Understanding how the sensor response signal is affected by gas flow rate is very important since the flow rate can potentially be used to increase sensor sensitivity and selectivity.

In initial work performed by Junhua Ding to explore the effect of gas flow rate on sensor performance [88], a Pd-doped sensor was operated in ethanol gas with constant concentration (~3000 ppm) but different flow rates, i.e. 2000, 1000, 500 sccm. All the responses were identical in the flow rate range of 500 – 2000 sccm. However, the gas sensor was mounted in a flow cell apparatus in Ding's experiment. Because the cross section area of this flow cell is about 1 cm^2, and the space velocity of gas molecules past the 100 μm wide microhotplate can not be controlled precisely, the testing results could be affected.

With the new microfluidic gas sensor, the cross section area of the microchannel is about 0.1 mm^2, and the gas flow rate can be varied from 0.5 sccm to 200 sccm. So the time for the gas molecules passing the 100 μm wide microhotplate could be from 0.5 μsec to 0.1 msec. In this experiment, dry air and 50 ppm methanol were used as gas analytes. The resulting sensor conductivity measurements under different gas flow rates are shown in Figure 3.17, with response normalized to the baseline value to reduce conductance drift. Figure 3.18a summarizes the relationship between flow rate and sensor response (ramp/base ratio) for both dry air and 50 ppm methanol. As can been seen from the TPS patterns, more reduction happened on the sensing film as flow rate was increased at lower temperature (< base temperature 200 °C), and more oxidation happened on the sensing film as flow rate was increased at higher temperature (> base temperature 200 °C). Figure 3.18b shows the ramp/base ratio difference between dry air and 50 ppm methanol at different flow rates. And the ramp/base ratio difference increased as the flow rate was increased. That means the sensitivity of the microfluidic gas sensor can be increased by increasing the gas flow rate inside the microchannel.

However the simulation results shown in Figure 3.12 gave different relationship between effluent concentration and air flow rate based on the air-liquid two-phase flow system. The effluent concentration of the air-liquid two-phase flow system can be increased by decreasing the air flow rate. As shown in Figure 3.18, the ramp/base ratio difference between dry air and 50 ppm methanol is small at flow rates below 10

sccm. According to the pressure analysis described in section 3.4.3, the air flow rate should be lower than 1 sccm to avoid the air flowing into the liquid channel. On the other hand, simulation results demonstrated that the effluent vapor concentration was strongly affected by the air flow rate at this flow rate range. In conclusion, the sensitivity of the water monitoring system can be increased by decreasing the air flow rate of the air-liquid two-phase flow system.

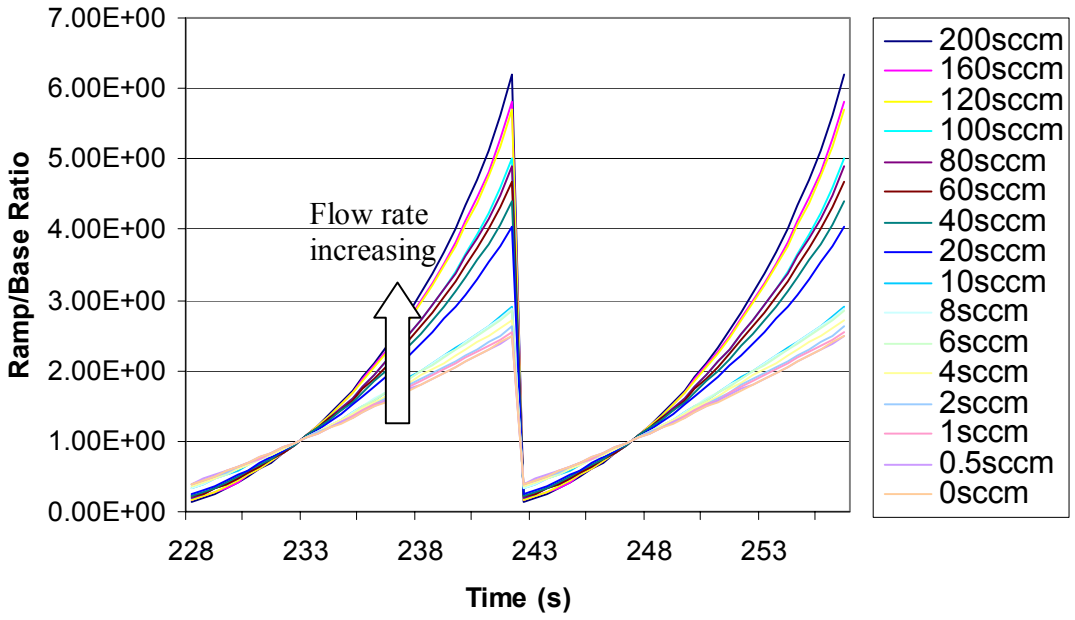

(a)

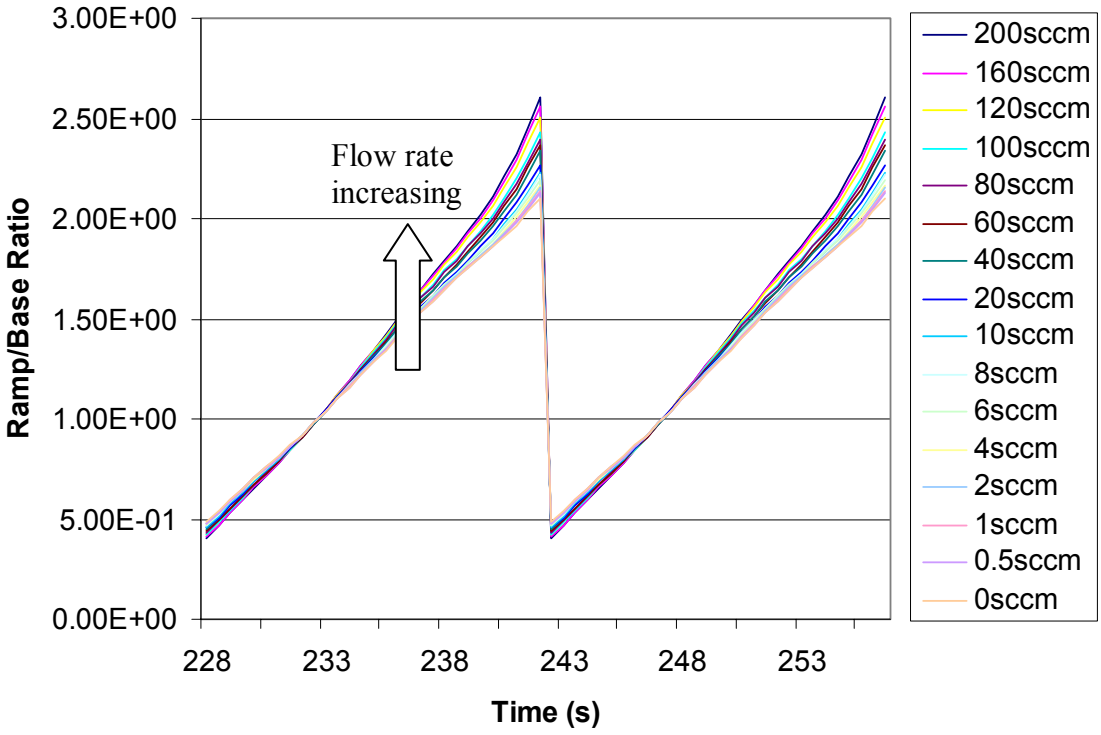

(b)

Figure 3.17 (a) TPS responses of SnO_2 film to dry air at flow rates from 0 to 200 sccm, and (b) TPS responses of SnO_2 film to 50 ppm methanol at flow rates from 0 to 200 sccm.

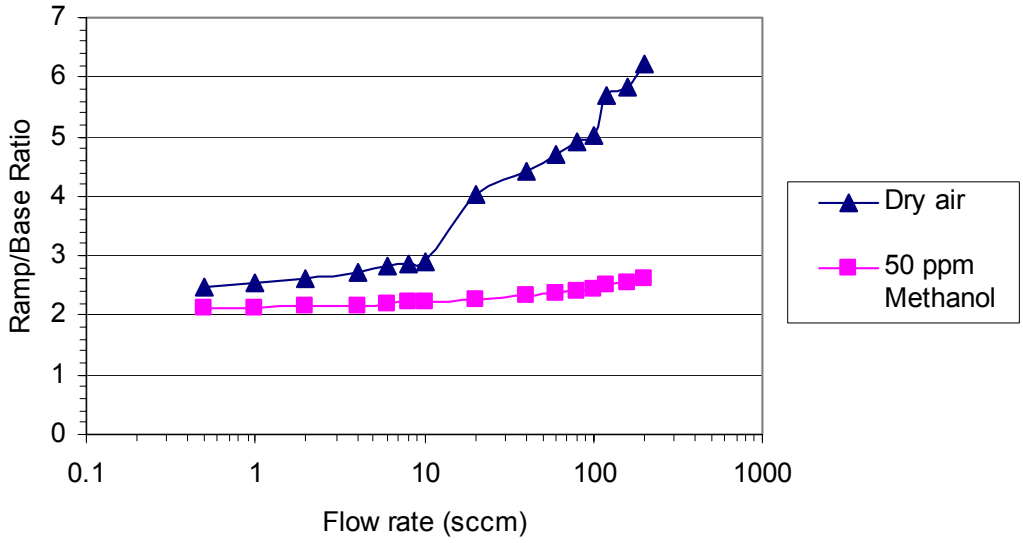

(a)

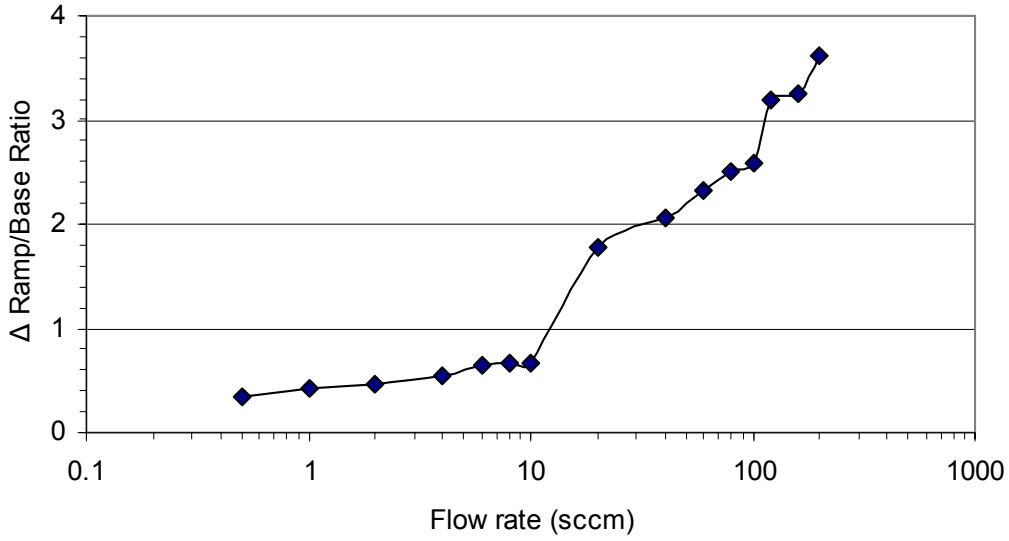

(b)

Figure 3.18 (a) Max value of ramp/base ratio for dry air and 50 ppm methanol at flow rates from 0.5 sccm to 200 sccm, and (b) max value of ramp/base ratio difference between dry air and 50 ppm methanol at flow rates from 0.5 sccm to 200 sccm.

3.4.3 Characterization of Air-Liquid Two-Phase Flow System

As described in Chapter 2, the air-liquid two-phase flow system was fabricated using polycarbonate substrates and PTFE membrane. The channels are separated by PTFE membrane with 70% porosity and 0.22 μm average pore size. For experimental characterization of the system, delivery of air and liquid to the microchannels of the device is achieved via two syringe pumps. The ability to stabilize the interface within the PTFE membrane is governed by Laplace equation [89], which dictates the maximum pressure drop across the membrane as

$$\Delta P = \frac{2\gamma \cos(\theta)}{r} \tag{3.25}$$

Where γ is the surface tension of the gas/liquid interface inside the pores, θ is the contact angle between the liquid and the membrane material, and r is the maximum pore size. Therefore, the pressures inside the microchannels must be carefully controlled to prevent breakthrough of the fluids through the holes in the membrane.

According to the theoretical models based on Bernoulli equation, the total pressure drop ΔP across the channel is expressed as [90]:

$$\Delta P = \frac{2f\rho\upsilon^2 L}{D} \tag{3.26}$$

$$f = 16/\mathrm{Re}$$

$$\mathrm{Re} = \rho\upsilon D/\mu$$

Where ρ is the density, υ is mean velocity of the fluid, f is friction factor of the fluid, L is the channel length, D is mean hydraulic diameter of the channel, Re is Reynolds number, and μ is viscosity of the fluids. The air and liquid flow rates must be carefully selected based on this analysis to keep the pressure drop across the membrane lower than the breakthrough value.

For this design, the parameters used in equation (3.24) and (3.25) and the breakthrough pressure and the pressure drop along the air and liquid channel are calculated and shown in Table 3.1.

Table 3.1 Parameters of two phase flow device for pressure computation.

Parameter	**Value**	**Units**	**Parameter**	**Value**	**Units**
γ	7.28×10^{-2}	N/m	μ_{air}	1.73×10^{-5}	$N\cdot S/m^{-2}$
θ	112	Degree	Re_{water}	$16.47v$	
r	0.22	μm	Re_{air}	$11.7v$	
ρ_{water}	999.93	Kg/m^3	f_{water}	$0.97/v$	
ρ_{air}	1.229	Kg/m^3	f_{air}	$1.37/v$	
D_1	164.7	μm	ΔP	2.479×10^5	Pa
D_2	181.6	μm	ΔP_{water}	$114.2L_{water}\times10^5$	Pa
μ_{water}	0.01	$N\cdot S/m^{-2}$	ΔP_{air}	$(436.5+16788\mathrm{L_{air}})v$	Pa

Liquid vapor tends to cool prior to reaching the gas sensor, leading to droplet formation in the air flow microchannel. Figure 3.19a shows that the liquid vapor

condensed to small liquid droplets on the PTFE membrane in the air flow channel. The liquid droplet formation is related to the air flow rate and liquid temperature. An experiment was performed to characterize the relationship between liquid vapor condensation and airflow rate and liquid temperature. In this experiment, two syringe pumps were used to deliver air and liquid to the microchannels of the air-liquid two-phase flow system respectively, a hotplate was used to control the temperature of the whole device, and the liquid vapor condensation in the air flow channel was monitored by a microscope. The number of liquid droplets per 1 mm channel length was counted as the level of liquid condensation.

The curve shown in Figure 3.19b exhibits that less condensation happens at constant temperature (28 °C) as the gas flow rate is increased. At flow rates above 3 sccm, no condensation is observed. The evaporation rate of liquid can be controlled by temperature. Higher temperature can cause more evaporation and increase the concentration of liquid vapor in the gas flow channel. Because the temperature in air flow channel is lower than the liquid temperature due to the fast continuous dry air flow, the vapor is intended to condense in the air flow channel. Figure 3.19c shows that more condensation happens at constant air flow rate (1 sccm) as the temperature is increased. More condensation was caused by higher vapor concentration in the channel. At room temperature (22 °C), almost no condensation is observed.

As demonstrated in Figure 3.19, the vapor concentration in the air flow channel is higher at higher liquid temperature and lower air flow rate, which is the same as the simulation results shown in section 3.3. Liquid temperature and air flow rate can be used to control the vapor concentration in the air flow channel. But the condensation in the air flow channel is not desired because it can cause several problems to the final water monitoring system. First, the solvent concentration in the air flow channel can be decreased due to the vapor condensation. The sensitivity of the monitoring system will be affected. Second, the small liquid droplets may accumulate in the air flow channel, and form a big liquid droplet finally. The air flow will bring this big liquid droplet to the hot microhotplate on the gas sensor, and the microhotplate could be damaged. In order to avoid this problem, all the liquid testing was performed at room temperature, because no condensation happened in the air flow channel at room temperature as shown in Figure 3.19c. If the liquid needs to be heated to increase the vapor concentration, the air also needs to be heated to the same temperature to avoid vapor condensation in the air flow channel.

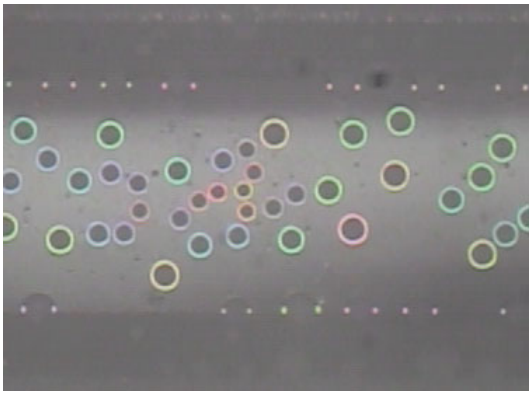

(a)

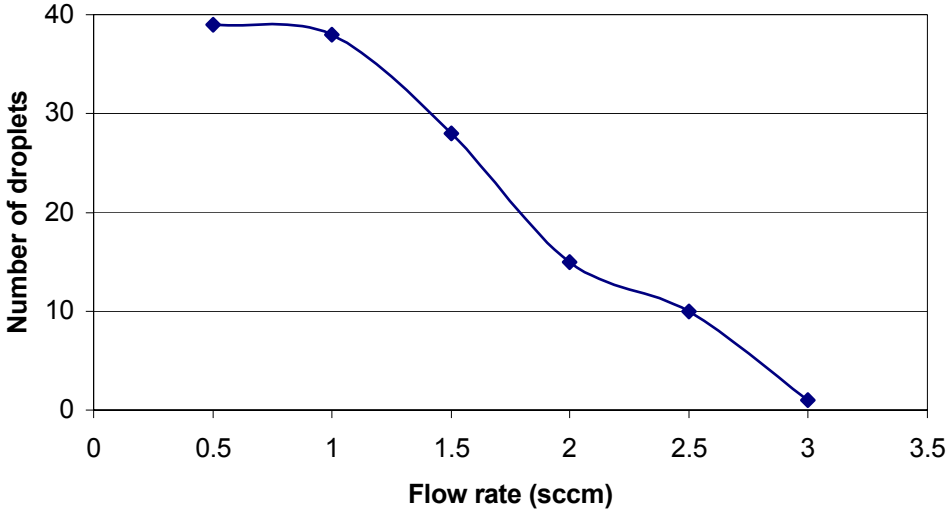

(b)

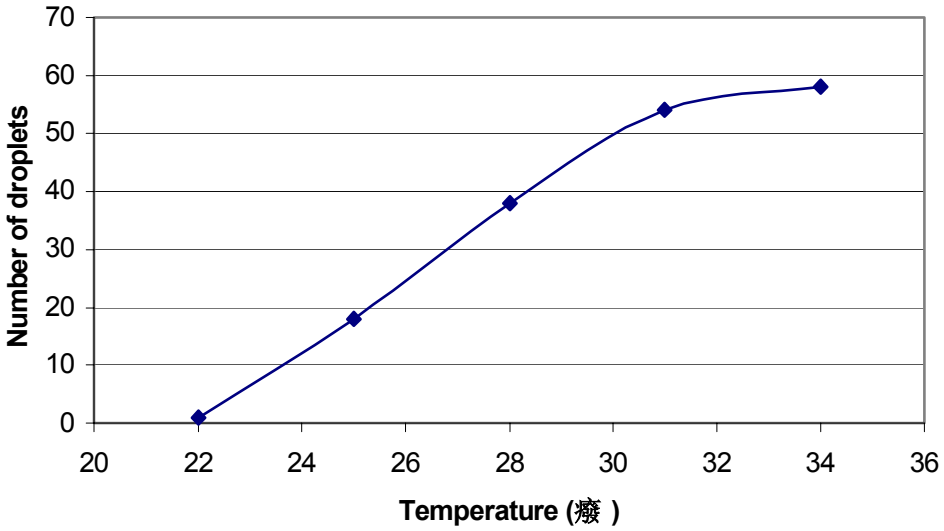

(c)

Figure 3.19 Characterization of the condensation with (b) different airflow rate and (c) different temperature.

3.4.4 Calibration and Sensitivity of the Water Monitoring System

3.4.4.1 Calibration of the Water Monitoring System

The water monitoring system was calibrated by sampling the known analytes with known concentration to the sensors. The experiment setup consists of a mass flow controller (MFC) providing dry air flow in gas channel, a syringe pump providing precise liquid flow in liquid channel, and a laptop computer to control the sensor temperature and measure the conductometric response of the gas sensor elements. The schematic of the experiment setup is shown in Figure 3.20. The analytes used in this experiment were methanol and DI water. According to equation 3.24 and 3.25, the flow rate of dry air is set to 0.5 sccm, and the flow rate of liquid is set to 20 μL/min. The air and liquid are pumped to their channels at the same time. Usually, it takes several minutes to stabilize the air/liquid interface. When the air/liquid interface had been stabilized, the TPS program was started. Four liquid analytes were tested in this experiment, which are DI water, 1, 10, and 100 ppm methanol in DI water. Figure 3.21 shows two complete TPS cycles of SnO_2 film to these four liquid analytes. The signal processing method used in this process is called running normalization, which normalizes each cycle with the final value, measured in the previous cycle. This method is used to reduce the conductance drifting of the sensing films. As can be seen from Figure 3.21, 1 ppm methanol can be successfully identified by this water monitoring system.

This system also demonstrates the ability to detect organic chemical contaminants listed by the U.S. Environmental Protection Agency, such as toluene and 1,2 dichloroethane. Figure 3.22 shows the TPS patterns of water, 10 ppm and 100 ppm toluene based on a SnO_2 sensor. Figure 3.23 shows the TPS patterns of water, 10 ppm, 100 ppm and 1000 ppm 1,2 dichloroethane based on a SnO_2 sensor. The sensitivity of the water monitoring system to toluene and 1,2 dichloroethane is not as good as which to methanol, but the small difference of the patterns can be identified by artificial neural networks (ANNs).

These calibrations also can be conducted under a variety of temperature conditions to provide a suite of training sets that can be used when the system is used under varying conditions in the field. In addition, the integrated thin film microheater can be used to heat the liquid in the microchannel to control the vapor pressure in airflow channel.

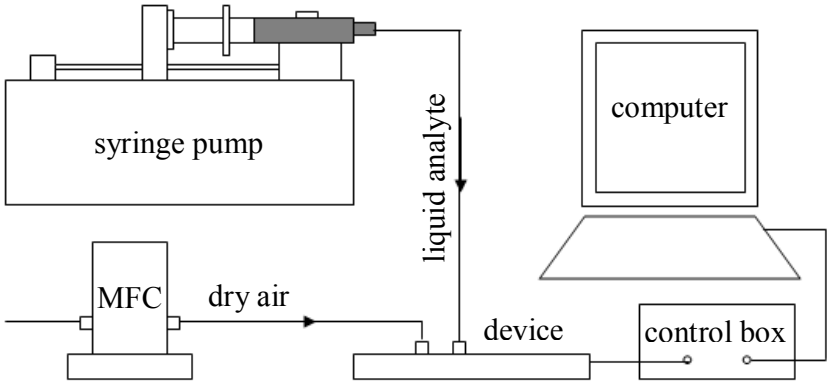

Figure 3.20 The schematic of experiment setup for water monitoring.

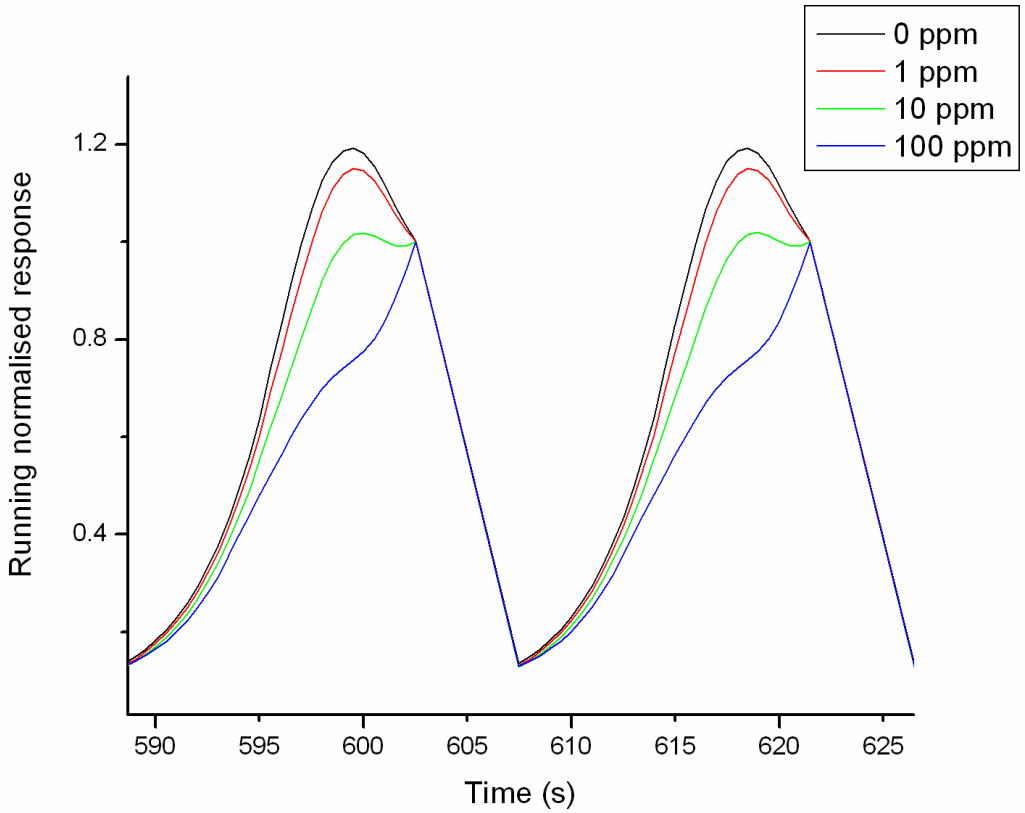

Figure 3.21 TPS responses of the fabricated water monitoring system to methanol at concentrations from 0 ppm to 100 ppm.

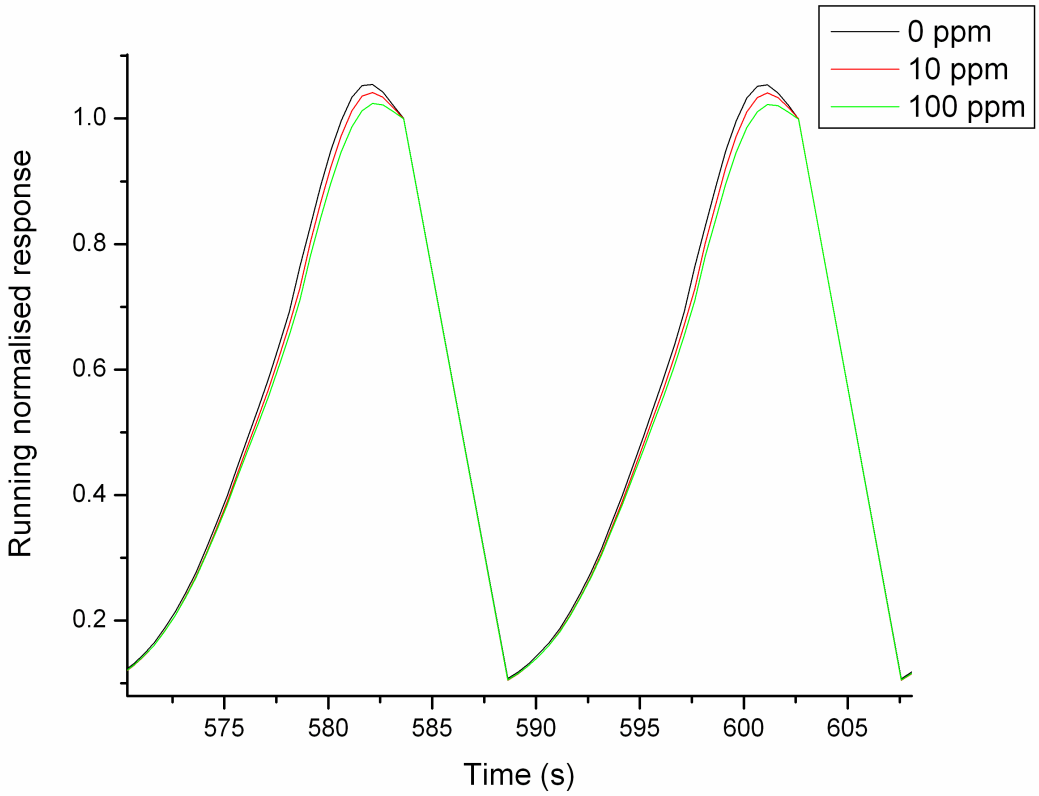

Figure 3.22 TPS responses of the fabricated water monitoring system to toluene at concentrations from 0 ppm to 100 ppm.

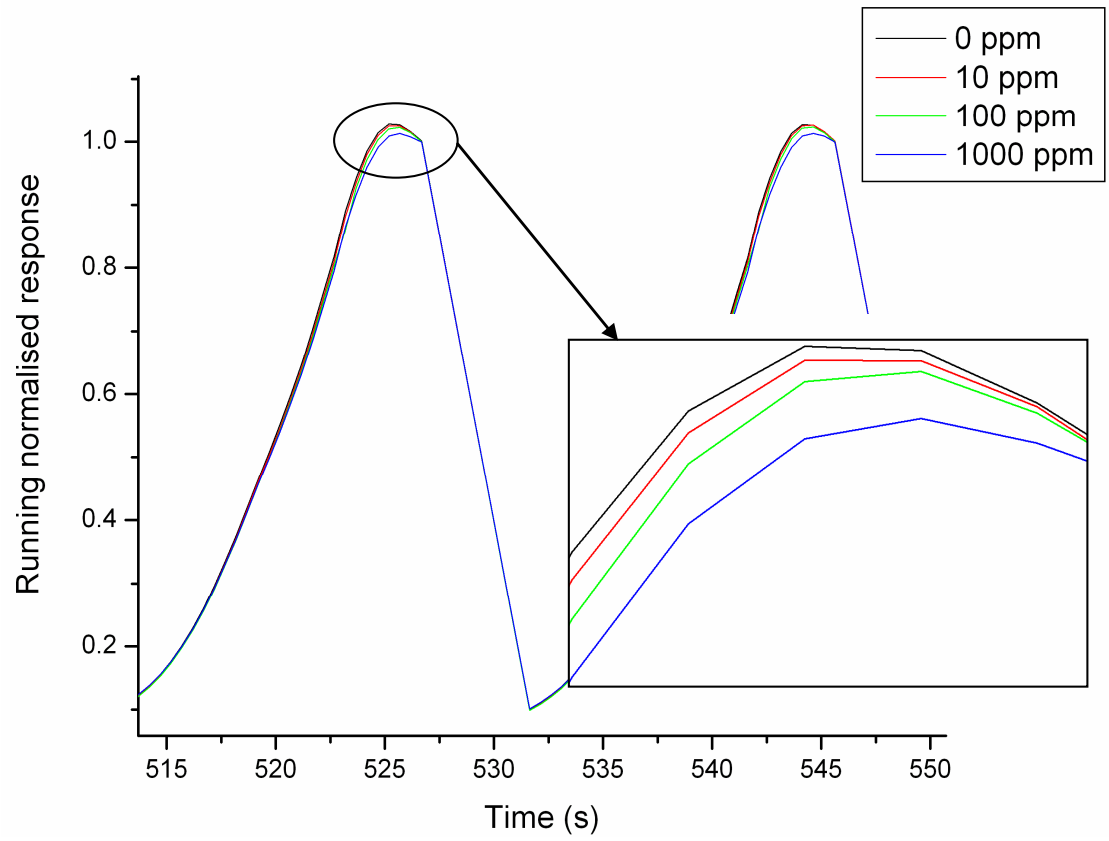

Figure 3.23 TPS responses of the fabricated water monitoring system to 1,2 dichloroethane at concentrations from 0 ppm to 1000 ppm.

3.4.4.2 Identification by Artificial Neural Network

As described previously, the microhotplate sensors can be operated in a rapid TPS mode, which allows us to measure reproducible response signatures. As can be seen from Figure 3.21, different response data were obtained from different liquid analytes, and the characteristic features within the signatures can be noted for the analytes identification and quantification.

Artificial neural networks (ANNs) can offer an efficient and rapid means of extracting valuable analytical data and then using them for recognition and classification [87]. ANNs have been used successfully for more than one decade to model nonlinear data by "learning" from known examples, and in many cases were proved better in processing complex data [87]. However, many ANN training algorithms need thousands of repeated presentations of the training examples to finally achieve small modeling errors. Large ANN models tend to get stuck in local minima during the training. The Guterman-Boger set of algorithms can easily train large-scale ANN models, as it starts from nonrandom initial connection weights, obtained by mathematical processing of the training data set [91]. In this study, the Guterman-Boger ANN modeling approach was applied to the methanol, toluene, and 1,2-dichloroethane TPS data measured using the integrated microfluidic platform. The data from a minimum of 25 TPS cycles for each analyte and analyte concentration were presented to the ANN as a 116-input vector (29 temperature steps on four sensors). The ANN was trained using 2/3 of the sensor data selected randomly, and the remaining 1/3 of the data was reserved as a validation data set. The random training and validation selection measures the consistency of the data within each analyte concentration value test. The resulting ANN model was applied to both the training and validation data sets. The estimated concentrations for each analyte are shown in Figure 3.24, Figure 3.26. Because the sensing films generally take about 1 min to reach equilibrium after being exposed to a new analyte concentration, the first 3 TPS cycles were removed from the these plots. However, these initial data points were used for the ANN training.

The average estimated concentrations are given in Figure 3.27 as a function of the known concentrations. The error bars in this figure represent +/- σ for the estimations at each concentration level. Due to the logarithmic axis, any non-positive concentration estimates are not shown in this figure. A summary of the estimated concentration error and standard deviation relative to the known concentrations is provided in Table 3.1. Predictions for methanol concentrations down to 10 ppm are quite good, with the concentration underestimated by 8%. When reducing the methanol concentration to 1 ppm, the estimation error increases to 40%, but with minimum deviation in the estimations. In contrast, the toluene estimation error is -3.6% at 10 ppm, but with a large standard deviation equal to 28.5% of the actual concentration level. The estimation error for 1,2-dichloroethane is even larger, with -62.2% error at 10 ppm and high variance in the data.

Based on the measured data, approximate detection limits for the fabricated system are 1 ppm for methanol, 10 ppm for toluene, and 100 ppm for 1,2-dichloroethane. The maximum contamination levels (MCLs) in drinking water have been set by the EPA-enforced Safe Drinking Water Act at 0.2 ppm for toluene, and 0.9 ppb for 1,2-dichloroethane [92]. Overall, the initial demonstrated detection limits of the prototype water monitoring system are approximately 2 orders of magnitude higher than the MCL for toluene, and around 5 orders of magnitude higher than the MCL for 1,2-dichloroethane. There are a number of reasons which can explain the relatively low sensitivity of the water monitoring system to both toluene and 1,2-dichloroethane.

First, the overall gas phase mass transfer coefficients *(k* in Eqn. 1) for toluene and 1,2-dichloroethane are substantially smaller than for methanol. Using an analytic model presented by Guo [82], k_{meOH} = 0.47 cm/sec, while values of *k* for toluene and 1,2-dichloroethane are around 200 and 10 times smaller, respectively. In addition, the diffusion coefficients for toluene and 1,2- dichloroethane are approximately 60% of the methanol coefficients, further reducing their steady-state effluent concentrations. Another important consideration for the polymer microfluidic system is that toluene and 1,2-dichloroethane are readily absorbed by the polycarbonate substrate, lowering their concentrations in both the liquid and vapor phases.

There are several system improvements which could be implemented to significantly enhance sensitivity. The properties of the analytes, such as Henry's law constant and solvent diffusion coefficients, play an important role in defining the effluent concentration, and these parameters can be increased simply by raising the temperature of the system. For example, the Henry's Law constants for toluene and 1,2-dichloroethane increase by about 1 order of magnitude between 25 °C and 100 °C [80, 81]. Thus it is possible to realize a substantial increase in gas-phase concentration by operating the sensor platform just below 100 °C. As revealed in Fig. 5, lower air flow rates will also increase the effluent concentration. Currently, the lowest gas flow rate is limited by the mass flow controller used in the experimental system. Lower flow rates could certainly be achieved by using an alternative pumping method. To avoid the potential for analyte loss due to absorption into the polycarbonate substrate, and alternative polymer with lower solvent absorption such as cyclic olefin copolymer could be used for the microfluidic system. Finally,

additional semiconducting oxide sensing films such as TiO_2 could be added to the microhotplates to provide additional response characteristics which may be used by the ANN for improving sensitivity.

Table 3.2 Summary of estimated concentration error (Δ) and standard deviation (σ) using the ANN model relative to the known concentration.

	1 ppm		10 ppm		100 ppm		1000 ppm	
	Δ	σ	Δ	σ	Δ	σ	Δ	σ
Methanol	40.1%	15.7%	-8.0%	2.4%	-0.4%	0.6%		
Toluene			-3.6%	28.5%	0.3%	2.9%		
1,2 DCA			-62.2%	214%	05.4%	24.2%	0.2%	2.4%

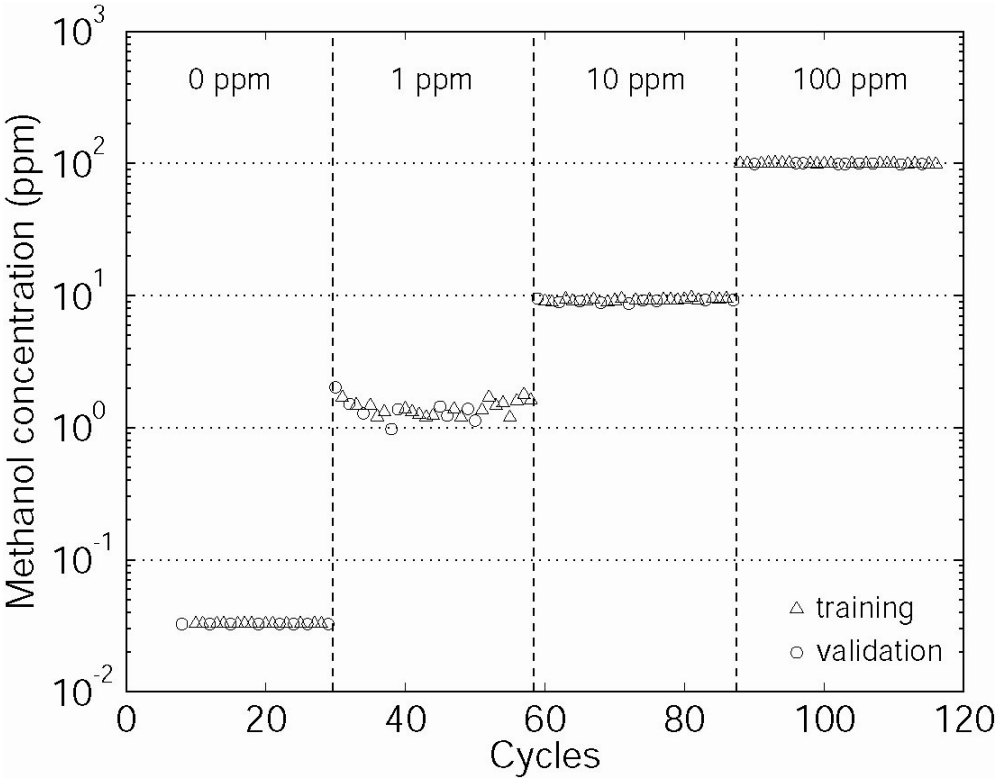

Figure 3.24 Prediction of methanol concentration by ANNs.

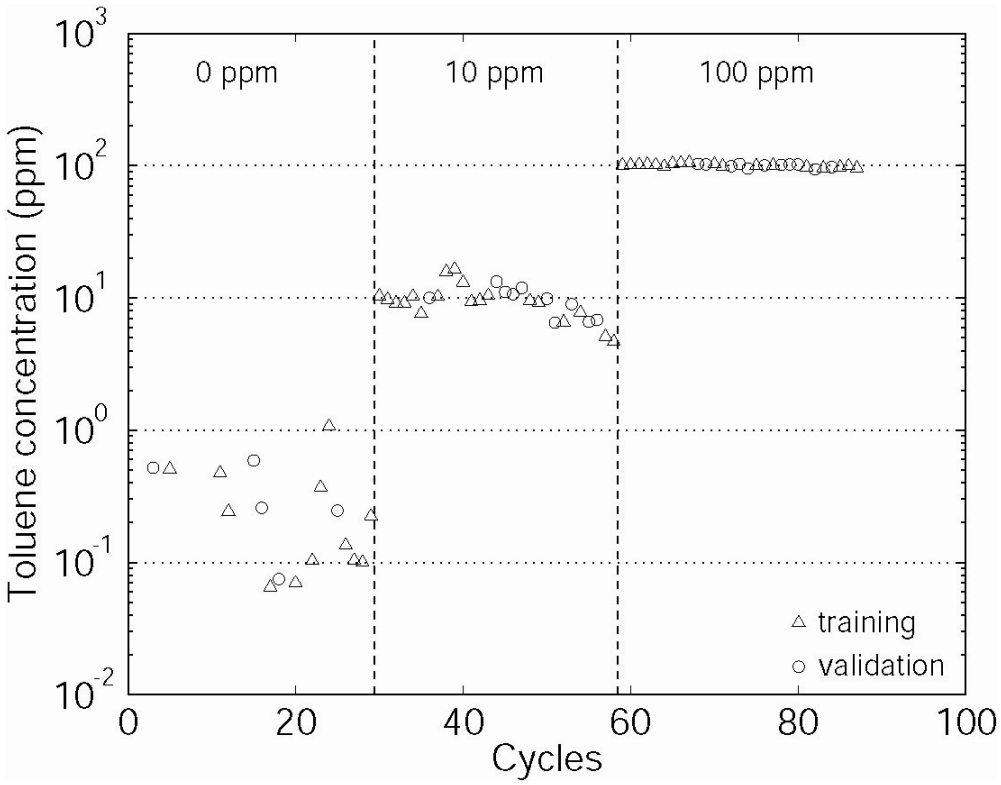

Figure 3.25 Prediction of toluene concentration by ANNs.

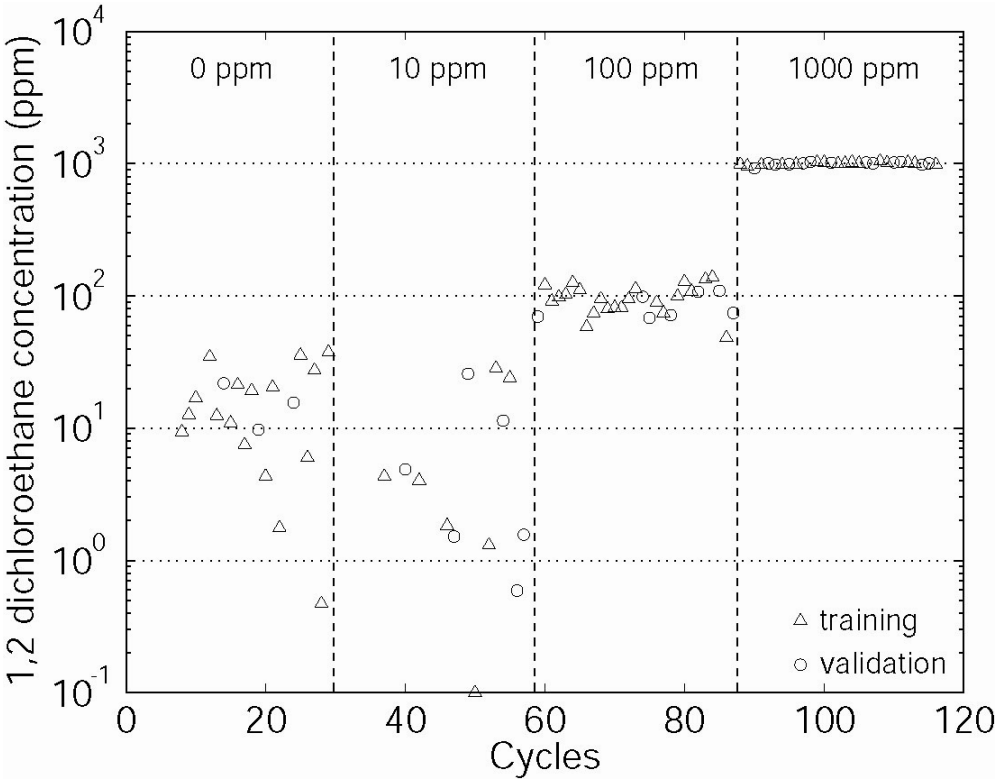

Figure 3.26 Prediction of 1,2 dichloroethane concentration by ANNs.

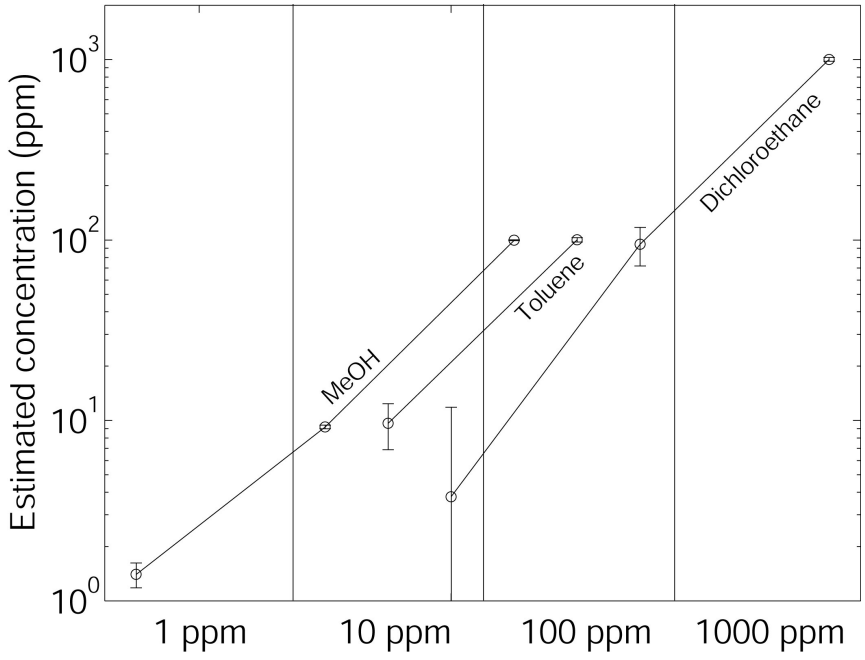

Figure 3.27 Summary of sensor performance for each VOC analyte. Error bars indicate standard deviations for the ANN data provided in Figure 3.24 – 3.26.

3.4.4.3 Sensitivity of the Water Monitoring System

The sensitivity of this device depends on the type of sensing film used in the integrated microhoplate gas sensor, the type of analytes, and the electronics used for measuring conductometric response signals. The noise level from electronics has been proved to be lower than 10^{-10} S. Since the SnO_2 film conductivity typically measures between 10^{-6} and 10^{-4} S, noise from the electronics interface does not substantially affect the sensing signal.

SnO_2–based gas sensors are considered to be good candidates for gas monitoring system due to their small size, low price, and good sensitivity. However, their response is characterized by irreproducibility and drift. Though SnO_2–based gas sensors have been extensively studied for four decades and there are thousands of publications and conference papers on them, no decisive breakthrough has been reported in improving the long-term stability of SnO_2–based gas sensors. This limitation can lower the sensitivity of the water monitoring system, because the conductance change could be covered by the drifting conductance. There are lots of reasons which may cause drift of metal oxide gas sensors including variation of humidity and pressure, changes of crystallite size, irreversible reaction with the gas phase, carbon deposition on the sensing film, deactivation of the catalyst, aging of the sensor heater, instability of the electrical contact, and interaction with an unsuitable sensing casing. However the reasons are not known in any detail. Therefore, no drift compensation model can be used in a pattern recognition algorithm [88]. Lots of methods have been explored to eliminate the drift of microhotplate gas sensors. Two

data process methods have been used to counteract the conductance drifting and to increase the sensitivity, repeatability and reliability of these devices. The first signal processing method is called running normalization, which normalizes each cycle with the final value, measured in the previous cycle. The second method involves the ratio between ramp conductance and base conductance.

Even if these data processing methods were used, the drift still can't be completely eliminated. In order to examine the drift problem of this water monitoring system, the water monitoring system was operated at TPS mode to DI water for one hour. The data was processed by the ratio between ramp conductance and base conductance method and running normalization. In order to show the baseline drifting in the one hour running, two cycles which come from the beginning and the end of the one hour running were picked up. Figure 3.28a, b, and c show the unprocessed data, the ramp conductance / base conductance ratio, and the running normalization respectively. The unprocessed data have big conductance drifting, and the running normalization can eliminate about 97% of the drifting.

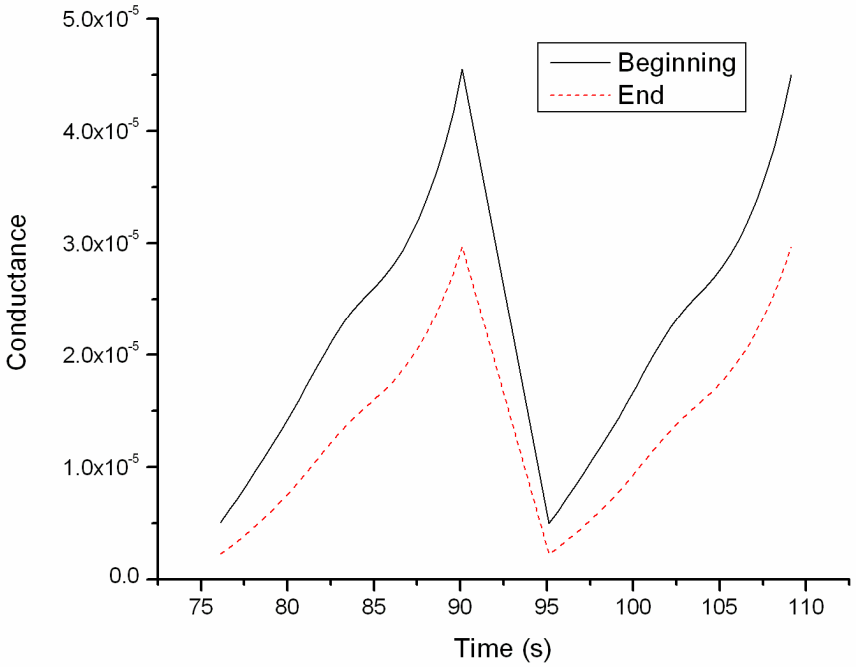
Conductance
5.0x10-5
4.0x10-5
3.0x10-5
2.0x10-5
1.0x10-5
0.0
75
80
85
90
95
100
105
110
Time (s)
Beginning
End

(a)

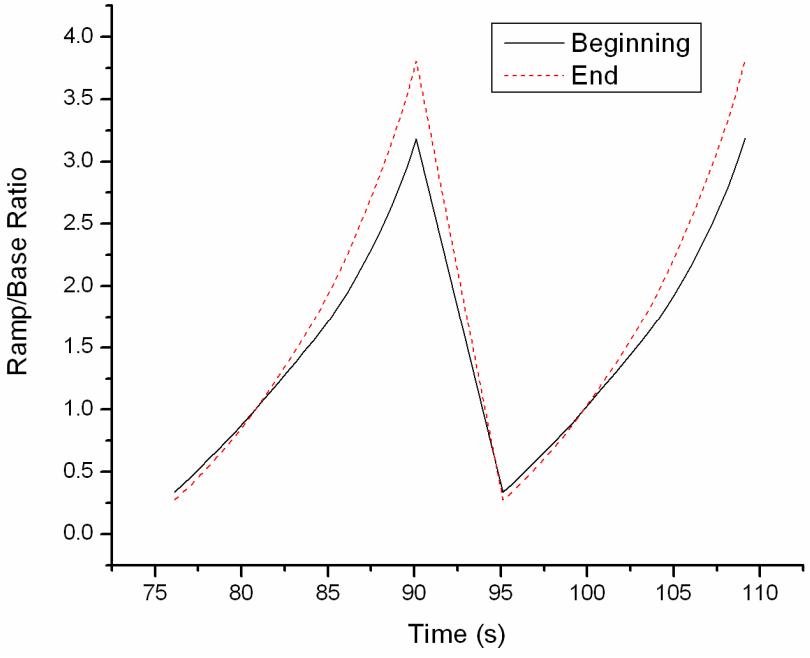
Ramp/Base Ratio
4.0
3.5
3.0
2.5
2.0
1.5
1.0
0.5
0.0
75
80
85
90
95
100
105
110
Time (s)
Beginning
End

(b)

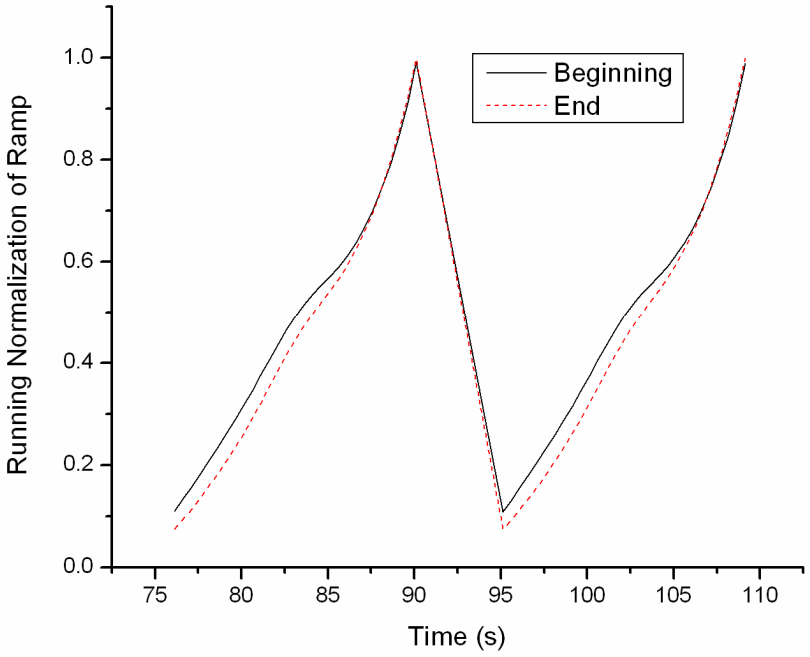

(c)

Figure 3.28 Drifting of (a) unprocessed data, (b) the ramp conductance / base conductance ratio, and (c) the running normalization.

Repeated tests were also conducted on the water monitoring system to test the reproducibility of this system. The same experiment was repeated at five different times in one day, and the time interval between two experiments is more than 30 min. Figure 3.29 shows the TPS patterns to DI water at five different times. As can be seen from Figure 3.29, the responses of the sensor are quite stable and reproducible to DI water.

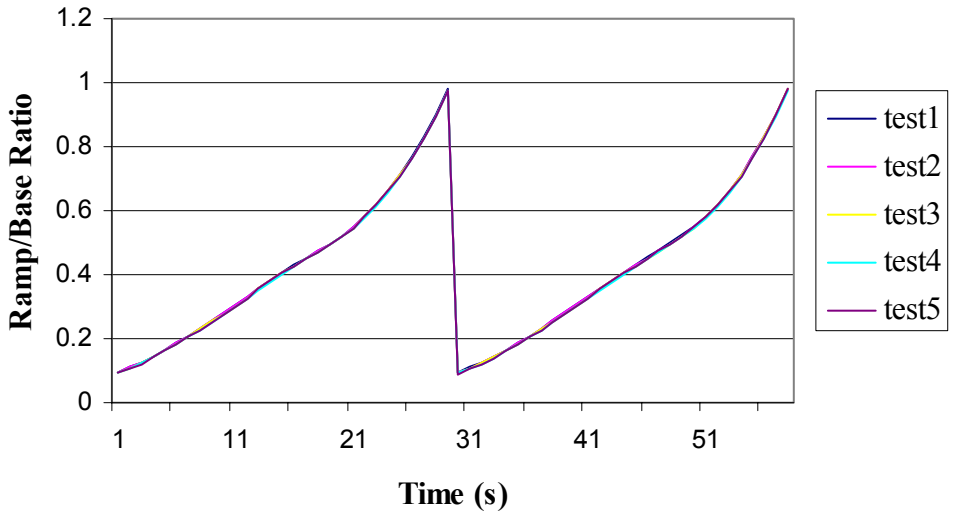

Figure 3.29 Repeated tests on the water monitoring system.

The properties of analytes are main reasons to affect the sensitivity of the water monitoring system. According to equation (3-12), the effluent analyte concentration in air flow is dependent on Henry's Law Constant of the analyte. The Henry's Law Constant is conventionally expressed as a ratio of partial pressure in the vapor (in various units such as Pa, atm, or torr) to the concentration in the liquid (also in various units such as mole fraction and mass or mole concentration or ratio). The Henry's Law Constants of some VOCs are listed in Table 3.3.

Table 3.3 Henry's Law Constants of some VOCs at 25 °C.

VOCs	solubility (mg/L)	Henry's Law Constants (atm-m 3 /mol)	MCL (mg/L)
Methanol	total	6.90E-06	
Benzene	1.75E+03	5.55E-03	0.005
Chlorobenzene	4.72E+02	3.70E-03	0.1
1,2-Dichlorobenzene	1.56E+02	1.90E-03	0.005
Endrin	2.50E-01	7.52E-06	0.002
Heptachlor epoxide	2.00E-01	9.50E-06	0.0002
Methoxychlor	4.50E-02	1.58E-05	0.04
Styrene	3.10E+02	2.75E-03	0.1
Toluene	5.26E+02	6.64E-03	1
m-Xylene	1.61E+02	7.34E-03	10

As can be seen from the Table 3.3, The Henry's Law Constants are different for different VOCs. Basically, the water monitoring system has higher sensitivity to the VOCs with larger Henry's Law constant. On the other hand, the sensing films have different sensitivity to different VOCs. So these two factors are the main reasons to affect the sensitivity of this device. Methanol is not on the list of maximum contaminant limit at EPA. It was used to as the initial testing analyte, because it is safe and easy to handle in the clean room at MML. Some VOCs in the EPS list, such

as toluene, benzene, and 1,1-Dichloroethylene have been tested using this water monitoring system.

3.5 Summary

A water monitoring system based on metal oxide microhotplate gas sensor has been developed to monitor and characterize volatile organic compounds (VOCs) in water supplies. This device employs a novel packaging to integrate discrete gas sensor chips into a larger polymer microfluidic substrate, including seamless fluidic and electrical interconnects between the substrate and gas sensor chip. In this study, an air-liquid two-phase flow system has been developed to provide solvent extraction for the water monitoring system. The air-liquid two-phase flow system consists of two micromachined polymer channels separated by a porous PTFE membrane. The theoretical performance of the air-liquid two-phase flow system was evaluated by solving the 2-D convective-diffusion equations. A detailed vapor transport model incorporating all relevant transport phenomena relating initial contaminant concentration in the source water to final gas concentration at the sensor film was developed. Using the model, transport physics can be simulated for a variety of chip geometries and flow conditions to optimize the system. This device can be used as a hand-held multimeter to provide in-situ manual analyses, or with a data processing and wireless system to provide long-term remote monitoring.

An experiment was performed to conduct the fundamental research on the relationship between gas sensor response and the gas flow rate. The results showed

higher sensitivity as the flow rate is increased. Characterization of the water monitoring system was performed using methanol as a test sample, while the integrated gas sensor was operated in a rapid temperature-programmed sensing (TPS) mode. In this study, a Guterman-Boger Artificial Neural Network (ANN) modeling approach has been applied to identify the small differences between TPS patterns. For concentrations above 10 ppm, the average measurements are within 15% of the actual values. This system also demonstrates the ability to detect organic chemical contaminants listed by the U.S. Environmental Protection Agency, such as toluene and 1,2 dichloroethane. The sensitivity of this device is mainly dependent on the integrated microhotplate gas sensor. The conductance drifting of the gas sensor seriously affected the sensitivity of these devices. Improved process methods are needed to increase the sensitivity, repeatability and reliability of these devices.

Chapter 4

Integrated UV Absorbance Detection of Proteins in a Polymer Microfluidic System

4.1 Introduction

4.1.1 Review of the Detection Methods for Protein Separation

Microfluidic systems have become more and more important in the field of analytical chemistry. Recently the analytical systems using microfluidics, called "micro total analysis systems" and "lab on a chip" have been extensively studied [93-97]. They performed a variety of analytical procedures, such as sample extraction, separation and detection on a small microchip. The microfluidic systems have great advantages over conventional systems, such as confined geometries, planar substrate, rapid separation, very small sample volumes, and low reagent consumption [98, 99]. But the miniaturization of analytical devices will also result in demanding on the highly sensitive detection systems. For example, the length scale of microchannel is as short as tens microns, which requires highly sensitive detector hardware. Some methods have been explored for microchip separation detection [99, 100]. This session briefly

describes five major detection methods for protein separation detection, which are absorbance detection, laser induced fluorescence, electrochemical detection, mass spectrometry and refractive index detection. The detection limits of these methods used in capillary zone electrophoresis instruments are shown in Table 4.1 [101].

Absorbance detection

UV absorbance detection is the most common detection method because it is most simple to use and most analytes can be observed with it. For proteins with functional groups, such as amino, alcoholic (or phenolic) hydroxyl, carbonyl, carboxyl, or thiol can be transformed into strong chromophores. Near UV spectroscopy is used to monitor protein chromophores that contain amino acids tryptophan (Trp), tyrosine (Tyr), and phenylalanine (Phe) residues. They have strong UV absorbance characteristics around 280 nm. The concentration of proteins can be measured through Lambert Beer's Law: $A = \varepsilon c l$, where A is the absorbance, ε is the extinction coefficient, l is the optical path length, and c is the concentration of the species. The photodetector measures transmitted light I, and the electronics converts this signal to a logarithmic relationship (A) which is proportional to concentration. Absorbance detectors are the most commonly used detectors for protein separations, particularly for capillary electrophoresis (CE) [100]. But the sensitivity of absorbance detectors is limited by the short optical path length of microchannel.

Laser induced fluorescence (LIF)

Fluorescence measures the emission energy after the molecule has been irradiated into an excited state. Many proteins emitted fluorescence in the range of 300 to 400

nm when excited at 250 to 300 nm from the aromatic amino acids (AAs). Only proteins with Phe, Trp, Tyr residues can be measured with the order of intensity Trp>> Tyr>> Phe. Due to the weak native fluorescence of protein, laser induced fluorescence usually requires pre- or postcolumn fluorescence labeling of the proteins to achieve very high sensitivity. Fluorescence detectors are probably the most sensitive among the existing detectors. The limits of detection of the best CE/laser-based systems are well below 10^{-13} M [102, 103], producing mass detection limits of less than 10 molecules [104].

Electrochemical detection

The electrochemical detector is also a popular liquid chromatographic detector. This detector is based on the measurements of the current resulting from oxidation/reduction reaction of the analyte at a suitable electrode. Since the level of the current is directly proportional to the analyte concentration. Electrochemical detection for CE can be divided into three main categories: potentiometric, conductimetric and amperometric [100]. Potentiometric detectors are based on classical ion-selective microelectrodes and have the ability to detect extremely small quantities of inorganic and organic ions in small probe volumes. The signal is produced when the ion of interest is transferred from the flowing sample stream into a lipophilic membrane phase of the detector. The presence of the analyte generates a change in the potential difference between the internal filling solution of the sensor and the sample stream. The potential difference is a measure of the ion's activity given by the Nernst equation and is directly related to the ion concentration. In

general, conductimetric detectors consist of two electrodes, in contact with the electrolyte solution, across which an electrical potential has been applied. When an analyte passes through the electrode gas, the conductivity between the electrodes changes by a quantity directly related to the concentration of the ionic analyte. Amperometric detection is based on electron transfer to or from the analyte of interest at an electrode surface that is under the influence on an applied DC voltage. The result of electron transfer is a redox reaction at the electrode that produces a current that is directly related to the analyte concentration.

Mass spectrometry

Mass spectrometry (MS) has become an important tool for the analysis of proteins. In its simplest form, MS sorts and measures the mass of individual ions (charged molecules). Ions can be formed from proteins using either electrospray (ES) or matrix-assisted laser desorption ionization (MALDI), each of which typically adds one proton (in the case of MALDI) or many protons (ES) to the protein. These positively charged protein ions can be analyzed directly to establish the protein's mass. CE-MS detection using chip CE has been studied by many researchers [105-107]. But the high cost and large size of the instrumental setup are sometimes incompatible with the concept of μ-TAS or Lab on a Chip [98].

Refractive index detection

Refractive index detectors are bulk property, nondestructive sensors that are mass-sensitive, and they are potential candidates for use as universal detectors in CE. The

detection principle involves measuring of the change in refractive index of the column effluent passing through the flow cell. The greater the RI difference between sample and mobile phase, the larger the imbalance will become. Thus, the sensitivity will be higher for the higher difference in RI between sample and mobile phase. On the other hand, in complex mixtures, sample components may cover a wide range of refractive index values and some may closely match that of the mobile phase, becoming invisible to the detector. Two basic types of RI detectors are on the market today, which are deflection detectors and reflective detectors. Both require the use of a two-path cell where the sample-containing side is constantly compared with the non-sample-containing reference side.

Table 4.1 Detection limits of methods used in capillary zone electrophoresis instruments.

Detection method	Mass detection limit (moles)	Concentration detection limit (molar)
UV absorbance	10^{-13} - 10^{-16}	10^{-5} - 10^{-7}
Fluorescence	10^{-15} - 10^{-21}	10^{-7} - 10^{-13}
Electrochemical	10^{-16} - 10^{-19}	10^{-8} - 10^{-11}
Radiochemical	10^{-18} - 10^{-19}	10^{-10} - 10^{-11}
Mass spectrometry	10^{-16} - 10^{-17}	10^{-8} - 10^{-9}

4.1.2 On-chip Absorbance Detection

Due to its label-free nature and relatively simple implementation, absorbance detection remains the most prevalent method for the analysis of proteins in microscale capillary separations. Direct absorbance measurements in the near UV range are often used due to strong absorbance characteristics around 280 nm for several protein chromophores, in particular the aromatic ring amino acids Trp, Tyr, and Phe. Direct absorption measurements made perpendicular to the flow through silica capillaries with inner diameters below 100 μm typically yield detection limits on the order of 10^{-5} to 10^{-6} M [103]. In order to improve measurement sensitivity, detection cells with longer pathlengths have been developed through the use of modified capillary geometries. However, as the path length increases, transmitted power decreases, eventually reducing the overall signal-to-noise ratio (SNR) as experimentally validated by Kutter et al. [108]. Furthermore, modified geometries providing longer optical pathlengths invariably lead to loss of effective separation resolution due to the larger minimum bandwidth defined by the optical pathlength [100], as well as the potential for band broadening introduced by geometric transitions between separation and detection volumes.

The limitation imposed by reduced separation efficiency becomes critical for absorbance detection in microfluidic separation platforms, where minimum bandwidths of separated species tend to be on the order of several hundred microns. For example, an average bandwidth of 150 μm has been reported for proteins separated by gel electrophoresis in a 2.5 cm long polycarbonate (PC) microchannel

[94]. Thus, there is a need for techniques to realize improvements in SNR without sacrificing the ability to resolve the higher efficiency separations offered by microfluidic systems. To this end, several approaches have been explored. Integrated optical components have been widely reported for improved optical coupling efficiency within small-volume microfluidic flow cells. For detection, both in-plane [109-111] and out-of-plane [112] fiber optic waveguides coupled to off-chip optical detectors have been used for absorbance measurements in microfluidic chips. To provide a higher level of integration while avoiding difficulties with optical fiber alignment, monolithic waveguides have also been used for small volume microfluidic absorbance detection [108, 113-115].

Further improvements in integration have been realized by directly coupling planar photodetectors into microfluidic systems, thereby eliminating the optical losses and fabrication complexity associated with fiber optic or monolithic waveguides. Fully integrated, monolithic systems combining photodetectors and microchannels within a single silicon substrate have been demonstrated by several groups[116, 117]. These platforms enable the placement of an optical detection element immediately adjacent to the volume of analyte being imaged, thereby eliminating the need for focusing optics to improve the collection efficiency. However, a significant disadvantage of this monolithic approach is the high fabrication cost, which is likely to prevent its practical use in disposable bioanalytical tools. Related work has focused on a hybrid approach, with optical detectors fabricated in a first substrate, and microchannels fabricated in a second substrate and aligned to the optics prior to bonding or assembly

of both layers [118-121]. While this approach simplifies the overall fabrication to some extent, processing costs associated with the photodetector substrate remain a significant limitation. To further reduce cost, Adams et al. used a commercially available CMOS imaging chip as an optical detector substrate, with a small polydimethylsiloxane (PDMS) layer containing microfluidic channels aligned to the active side of the CMOS chip [122]. While the maximum microchannel length used in this work was constrained by the small size of the CMOS chip, the concept of using an off-the-shelf silicon photodetector chip combined with a separate microfluidic substrate represents an intriguing solution for realizing low cost absorbance detection in a microfluidic platform.

In the present work, the idea of combining commercial silicon photodetectors with polymer microfluidics is extended using a new approach in which bare photodetector dies are seamlessly integrated into a larger polymer microfluidic substrate. This silicon-in-plastic approach offers several benefits. First, compared to previous demonstrations involving monolithic or hybrid integration of microchannels with custom-fabricated optical detection substrates, fabrication costs are lower. Since the cost per unit area for photodiode fabrication is significantly higher than for the microfluidic substrate, the ability to use no more than the necessary silicon area substantially reduces fabrication expense. Second, unlike previous demonstrations involving the placement of a microfluidic layer on top of a small silicon chip [122], the size of the microfluidic substrate is not limited when using the silicon-in-plastic approach. A conceptual schematic of the proposed system is shown in Figure 4.1.

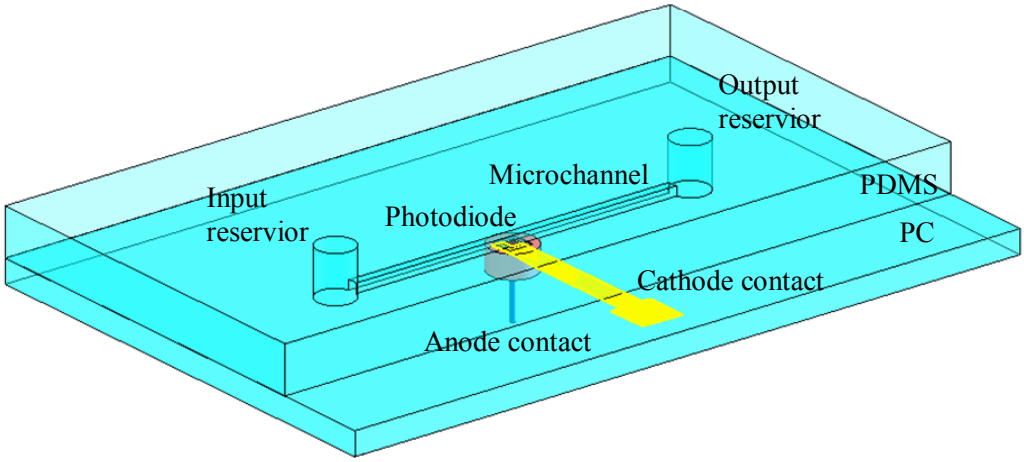

Figure 4.1 Device schematic of the integrated UV absorbance detection system.

Absorption measurements from fabricated microfluidic substrates containing integrated photodiode chips are demonstrated using bovine serum albumin (BSA) as a model protein. With a noise floor below 10^{-4} absorption units (AU), detection limits for BSA are achieved at concentrations ranging from 15 nM using a device with a detection cell volume of 14 nL, to 121 nM with a detection cell volume of only 0.5 nL.

4.2 Fabrication

4.2.1 Photodetectors

Silicon p-n junction photodiodes (UVG-series, International Radiation Detectors (IRD), Torrance CA) tuned for detection in the 160 to 600 nm wavelength range were purchased as bare dies approximately 1.6 mm x 1.6 mm in size. Unlike conventional p-n junction photodiodes, these photodiodes do not have a doped dead-region in front and have zero surface recombination resulting in near theoretical quantum

efficiencies to UV and visible photons. The UVG series photodiodes are fabricated by a ULSI (Ultra Large Scale Integrated Circuit) compatible process and their structure is shown in Figure 4.2. The typical spectral response of UVG-series photodiodes with a 700 Å oxynitride window as reported by the manufacturer is shown in Figure 4.3. The peaks and valleys above 160 nm are caused by the interaction of the complex index of refraction of silicon with the index of refraction and thickness of the oxynitride according to the standard interference relations of optics. Additional details of the photodiode fabrication and performance are available in the literature [123, 124]. The active area of all UVG products has at least 7 orders of magnitude dynamic range from 0.00063 mm^2 to 100 mm^2. Photodiodes with different active areas, namely $(160\ \mu m)^2$, $(70\ \mu m)^2$ and $(25\ \mu m)^2$, were used in this study.

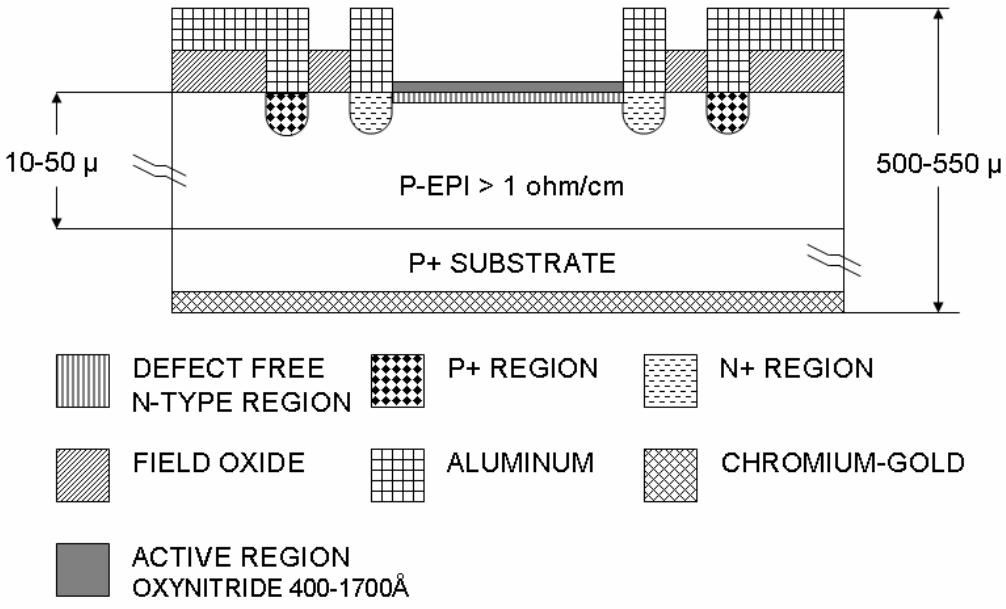

Figure 4.2 Structure of the UVG serials photodiodes.

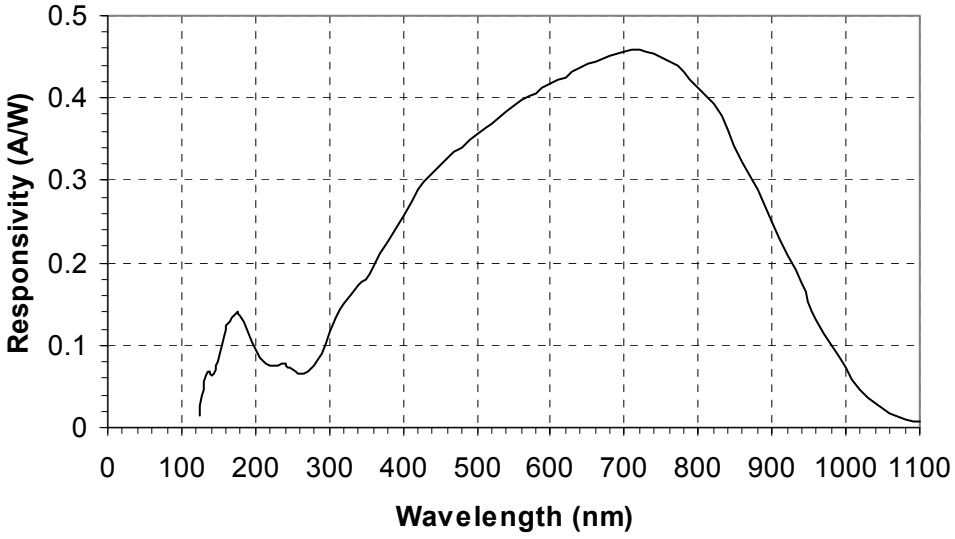

Figure 4.3 The typical spectral response of UVG series photodiodes.

4.2.2 Material Selection

In addition to material properties, such as melting point and melt viscosity, required for mass production using injection molding or embossing technologies, optical properties such as light transparency at the desired wavelength range are very important characteristics. For peptide and protein detection, the chip material should ideally be transparent in the wavelength range of 214 – 280 nm. Rohr et al. summarized the UV-spectral of quartz, glass, and several commercial polymers [125]. Their UV-spectra are shown in Figure 4.4. While quartz is transparent well into the deep-UV, most polymers are opaque in below 300 nm and therefore not suitable for the present application. Among the available synthetic polymers commonly used for fabricating microfluidic systems, PDMS and cyclic olefin copolymer (COC) exhibit the best transparency between 220 – 300 nm. PDMS was used in the present study due to ease of fabrication.

The spectral response of integrated photodiode was tested using a commercial variable-wavelength ultraviolet absorbance detector with a deuterium lamp as the UV source. The typical spectral output of deuterium lamp is shown in Figure 4.5. The normalised spectral responses of an integrated photodiode without PDMS microchannel and with a 2.1 mm thick layer of PDMS bonded to the detector surface are shown in Figure 4.6.

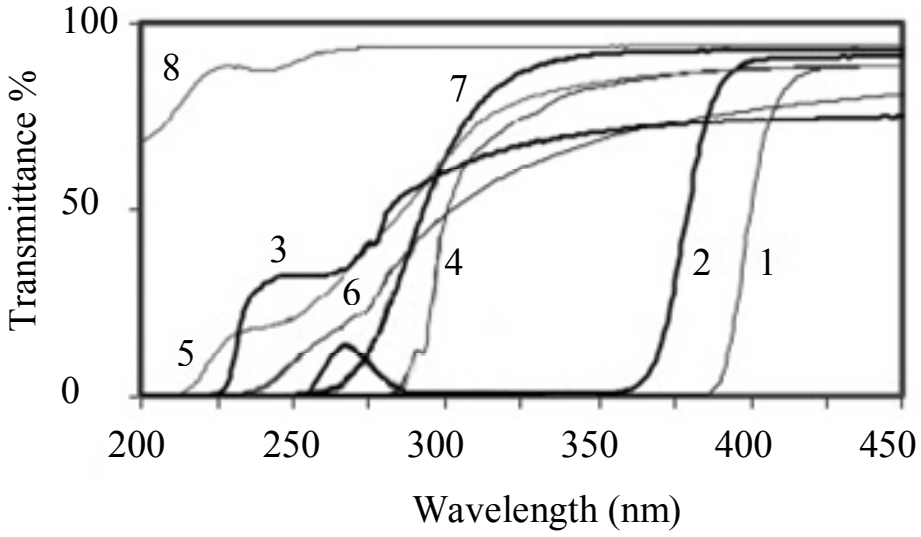

Figure 4.4 UV-spectra of polycarbonate (1), poly(methyl methacrylate) (2), polydimethylsiloxane (3), polystyrene (4), cyclic olefin copolymer (5), hydrogenated polystyrene (6), Borofloat glass (7), and quartz (8).

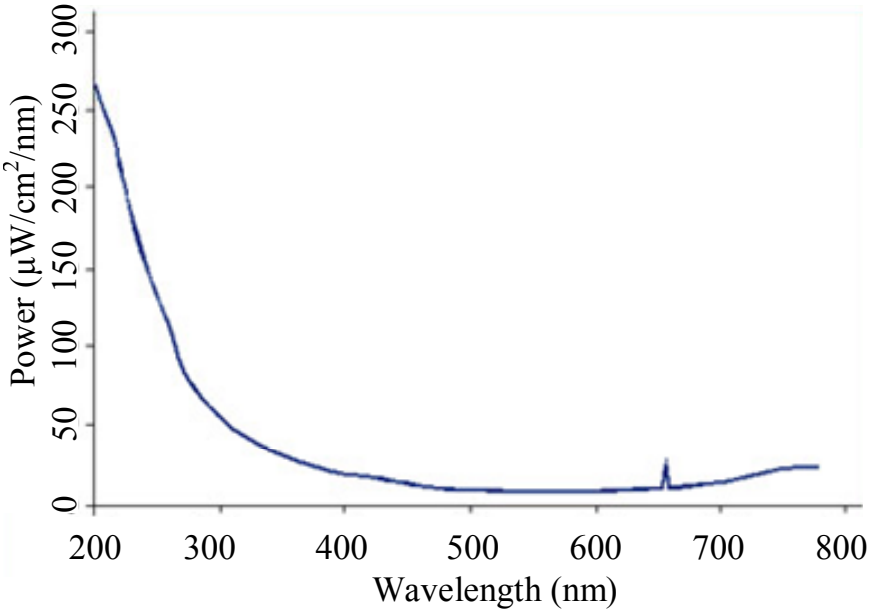

Figure 4.5 The typical spectral output of deuterium lamp.

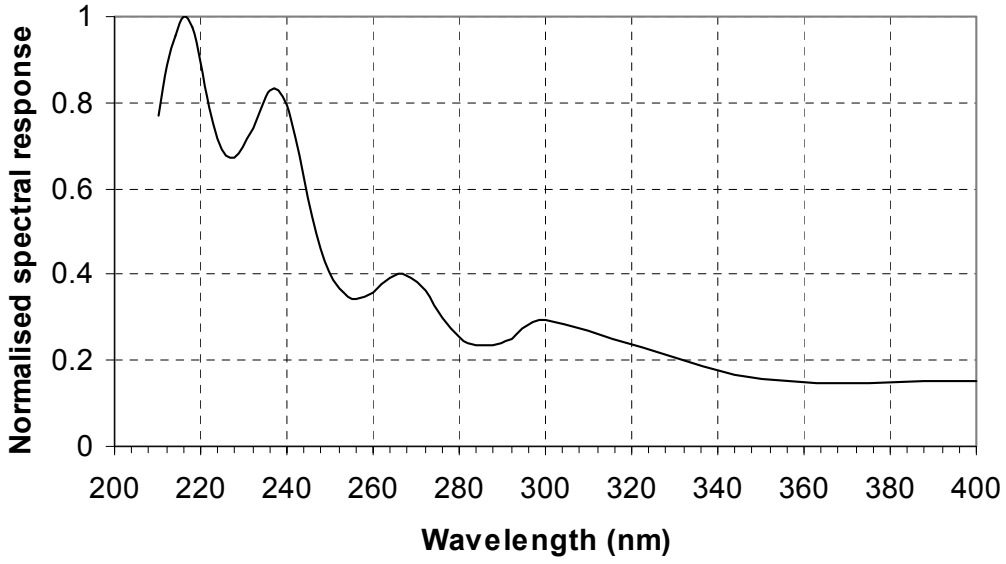

(a)

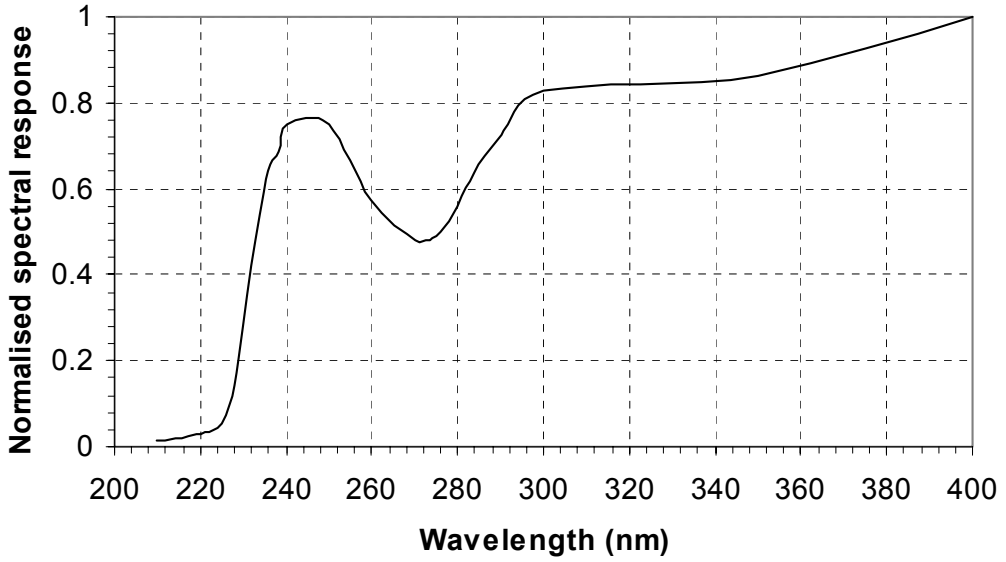

(b)

Figure 4.6 The normalised spectral response of the integrated UV absorbance detection system bonded (a) without PDMS microchannel and (b) with PDMS microchannel.

Despite the benefits of PDMS fabrication, this material suffers from several key drawbacks. PDMS exhibits a high permeability for both gases and, in some cases, analytes. It suffers from poor mechanical properties including low elastic modulus and low tensile strength which can lead to poor mechanical robustness and low geometric stability. The ionic nature of the siloxane backbone in PDMS makes it susceptible to hydrolysis, and long-term exposure to water is capable of breaking the siloxane bond, especially at a pH lower than 2.5 or higher than 11. It is well known that PDMS suffers from limited life span for devices requiring stable surface charge for electroosmotic flow, and in general possesses low solvent stability. Thus, although PDMS offers a simple and attractive approach for microfluidic fabrication, it may not be suitable for all situations, particularly when a wide range of pH levels or long-term exposure to solution is required as in many proteomic applications [126].

COC is a commercial engineering polymer with the similar UV transparency to PDMS. In addition, COC has excellent chemical resistance, good temperature stability, low water absorption, and low gas permeability. COC only dissolves in solvents such as toluene and hexane that are seldom used in proteomic applications. These properties make COC one of the best candidate materials to be used in future development. However, both PDMS and COC strongly absorb UV below 220 nm. They are not suitable microfluidic materials for the device which is designed to detect peptide (UV absorption at 214 nm). As can be seen from Figure 4.4, only quartz is

transparent at this UV range. In the future design, quartz can be used as the microfluidic channel material for peptide detection.

4.2.3 Silicon-in-Plastic Fabrication

The fabrication process developed for integration of bare photodiode chips into a polymer microfluidic substrate is shown in Figure 4.7. The process is a modified version of the previously discussed procedures described in Chapters 2 and 3. Briefly, a short wire is connected to the backside (anode contact) of the photodiode chip by conductive epoxy. A round mold hole large enough to accommodate the photodiode chip is milled through a polycarbonate (PC) substrate. The photodiode chip is temporarily placed face-down on a flat layer of cured PDMS (Sylgard 184; Dow Corning, Midland, MI), and the milled PC substrate is positioned over the chip with the chip located inside the milled mold hole. The PDMS provides for easy mold removal while also forming a seal against the surface of the chip. The assembly is placed in a vacuum chamber and the mold hole is filled with epoxy (353ND; Epoxy Technology, Billerica, MA). Casting in vacuum prevents air bubbles from being trapped at the edge of the chip, which appear as large pits when the mold is removed. Filling the mold under vacuum is accomplished by placing a syringe into the vacuum chamber with epoxy at the syringe tip positioned at the mold hole, and a defined volume of air at the back of the syringe. After the epoxy is cured for 12 hr at room temperature, followed by 12 hr at 50 °C, the PDMS is removed. The epoxy serves to secure the chip within the PC substrate, while leveling the chip face to within several microns of the PC surface.

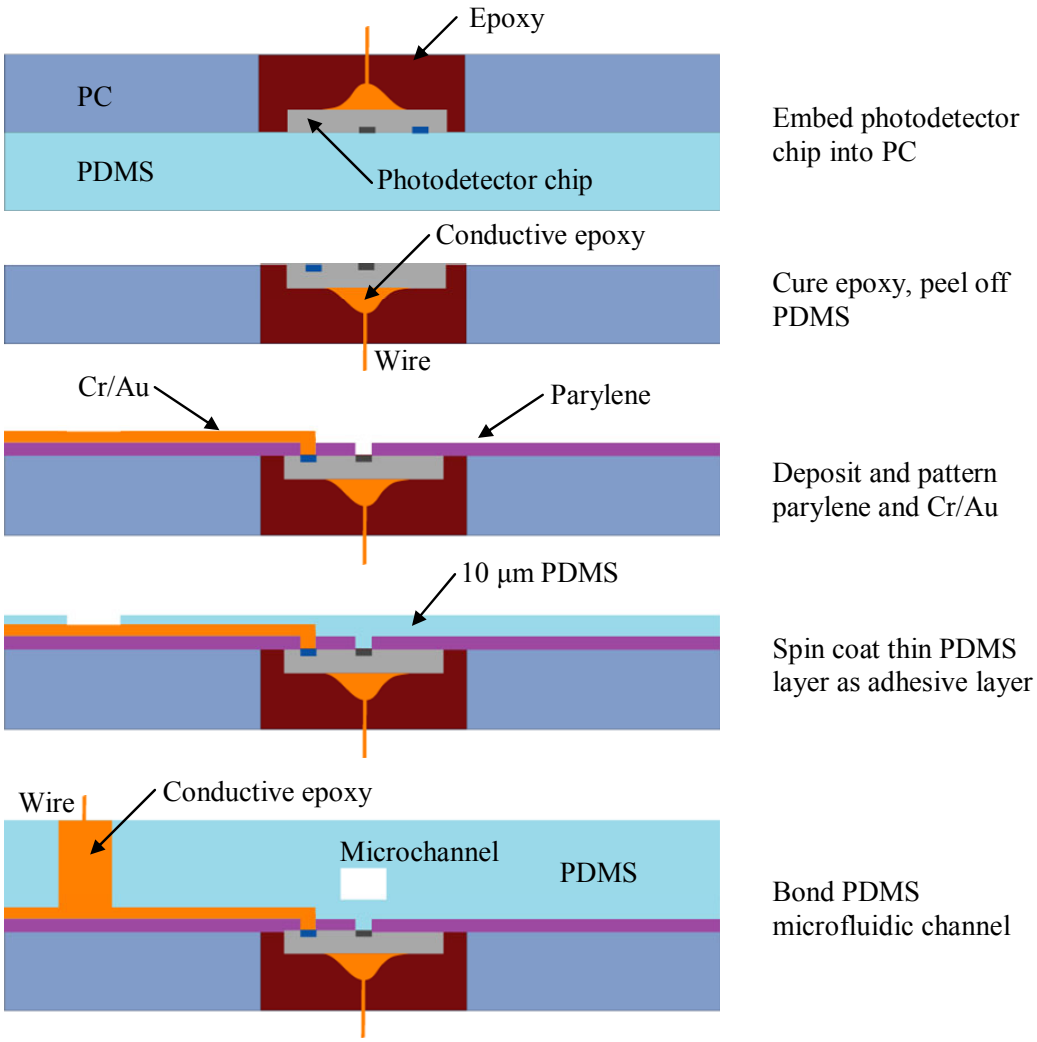

Figure 4.7 Fabrication process for the microfluidic absorbance detection platform.

Although the epoxy layer can level the silicon chip surface to within several microns of the PC surface, small gaps can form at the silicon/epoxy/polycarbonate interfaces due to thermal mismatch and epoxy shrinkage during curing. These gaps, which are on the order of several microns deep, can cause several problems during the metal deposition process. First, the sidewall of the bare photodiode die is exposed semiconducting silicon, and deposited metal which touches the sidewall can potentially shunt the active area contact to ground. Second, open circuits can form

due to incomplete metal coverage over the gap. To overcome this problem, a ~6 μm layer of parylene C is deposited to passivate the sidewalls and bridge small gaps prior to metal deposition. Parylene C covering the active area of the photodiode is removed by oxygen plasma etching using a Cr/Au mask. After the parylene layer is patterned, the mask metals are stripped, and new Cr (200 Å) and Au (5000 Å) layers are deposited and patterned to provide interconnections from the cathode contact on the photodiode to a connection pad on the PC substrate.

Next, a 10 μm thick layer of PDMS is spun onto the substrate and partially cured as an adhesive layer. The microfluidic channel was formed by micromolded PDMS from an SU-8 template. The PDMS layer was bonded to the substrate, with the active area of the photodetector located inside the microchannel using a microscope and manual aligner. After the PDMS structure was fully cured (50 °C for 8 hr), conductive epoxy was applied to make contact to the cathode and anode interconnects. A photograph of completed device fabricated using this approach is shown in Figure 4.8.

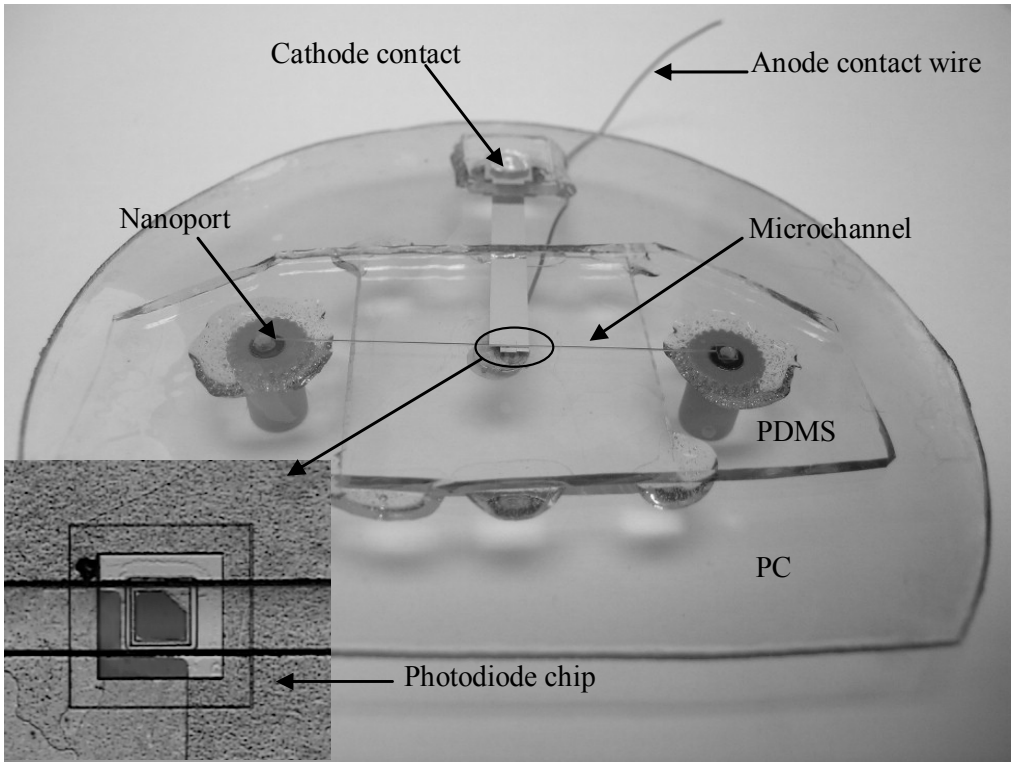

Figure 4.8 Photograph of a fabricated microfluidic substrate with integrated photodetector chip.

4.3 Experimental

4.3.1 Photodiode Amplifier Design

Photodiode junctions convert the photon energy of light into an electrical signal by releasing and accelerating current-conducting carriers within the semiconductor. The magnitude of the current generated by photodiodes corresponds directly to the light intensity [127]. However, most electronic instrumentation accommodates voltage rather than current signals. Current to voltage conversion is needed to amplify and convert small current signal to voltage signal. There are two ways to use the

photodiodes, the photovoltaic mode and the photoconductive mode. In photovoltaic mode, there is no voltage across the photodiode. Its advantage is linear output, low noise and no dark current. In photoconductive mode, there is a voltage across the photodiode, which lower its capacitance. Less capacitance allows a faster amplifier while maintaining stability.

In this study, the current generated by the integrated photodiode chip is very small (< 1 nA), due to the very low output light intensity of the UV source and the small active area of UVG photodiodes. Because current protein detection does not require very fast amplifier, a zero-biased photovoltaic circuit is developed specifically for use with the integrated UVG serials photodiodes. The electrical schematic of the amplifier circuit is shown in Figure 4.9. A monolithic electrometer operational amplifier with very low input bias current, AD549 (Analog Devices), was used as the OP AMP in this circuit. The 50 GΩ feedback resistor was FA series high value thick film resistor bought from HY-MEG Corporation. But the long interconnecting traces and cables can pick up significant amounts of noise from electromagnetic interference and mechanical vibration. In order to reduce noise, the circuit board was specifically designed to make the electrical connections as short as possible, the circuit board was located into an electromagnetic shielded box, and the electromagnetic shielded cable was used in this design.

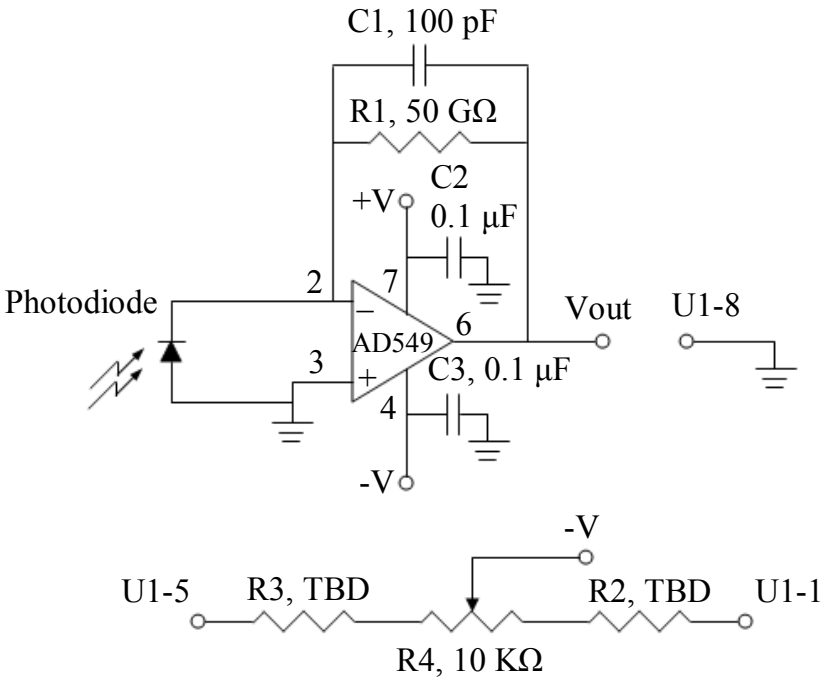

Figure 4.9 The electrical schematic of the amplifier circuit.

4.3.2 Experimental Setup

A schematic of full test setup is shown in Figure 4.10. Bovine serum albumin (BSA) was used as a model protein, with 10 mM Tris (hydroxymethyl) buffer used to dilute protein sample. Both BSA and Tris buffer stock solutions were purchased from Sigma (St. Louis, MO). Diluted protein sample and Tris buffer were loaded into two syringe pumps (Harvard Apparatus, Holliston, MA), which were connected to the input reservoir of the microchannel through a capillary T connector and nanoport fittings (Upchurch Scientific, Oak Harbor, WA). A computer running MatLab was used to provide external control of the individual syringe pumps through an RS232 interface.

A commercial variable-wavelength ultraviolet absorbance detector with a deuterium lamp (Spectroflow 757; Applied Biosystems, Foster City, CA), was modified for use as the UV source. The wavelength range for detection is from 190nm to 365nm. The standard flow cell and the original photodiodes were removed from the instrument, and the microfluidic substrate was placed vertically on a 3D stage, with the integrated photodiode aligned with the UV output. The chip surface was positioned 6 mm from the terminal optics for the absorbance detector's UV output. Both the Spectroflow 757 and the 3D stage were fixed on a vibration isolation table to reduce noise. All testing was performed in a dark room.

The small current signal generated by the integrated photodiode was amplified and converted to a voltage signal by a transimpedance amplifier interface described previously. The voltage output data was captured using an Agilent data acquisition unit (Agilent 34970A, data acquisition/switch unit) with a sampling rate of 1 sec. The computer and data acquisition system were located outside the dark room to further reduce noise. A picture of experimental setup is shown in Figure 4.11.

Proteins have two absorbance peaks in the UV region, one between 215-230 nm, where peptide bonds absorb, and another at about 280 nm due to light absorption by aromatic amino acids (tyrosine, tryptophan and phenylalanine). The absorptivity constant for a particular protein at 280 nm depends on its composition. Proteins that contain a higher percentage of aromatic amino acids have higher absorptivities at 280 nm than those with fewer. As demonstrated in Figure 4.12, BSA absorbs UV light

with two distinct peaks. The peak centered on 280 nm is the result of absorbance by the aromatic ring portion of their structure. The peak at 230 nm is caused by absorbance of peptide and carboxylic acid moieties in the compounds [128]. Because BSA has higher UV absorbance at 230 nm, all the testing was performed at 230 nm excitation to get higher sensitivity.

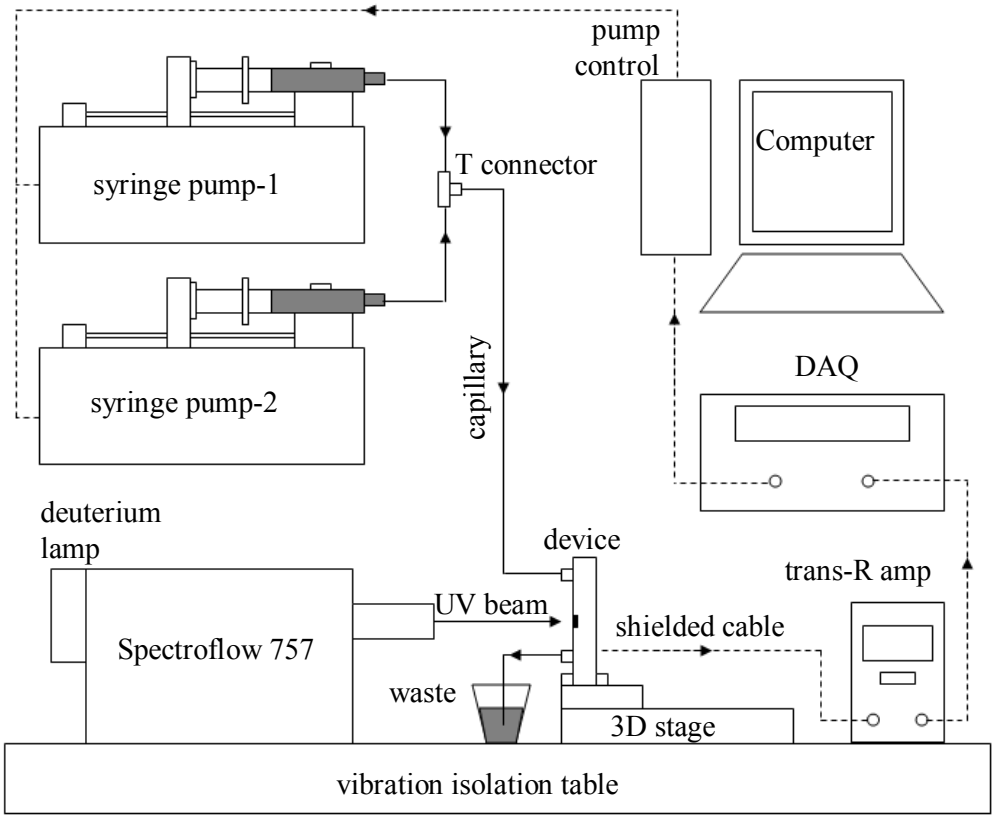

Figure 4.10 Schematic of the testing apparatus used for data collection.

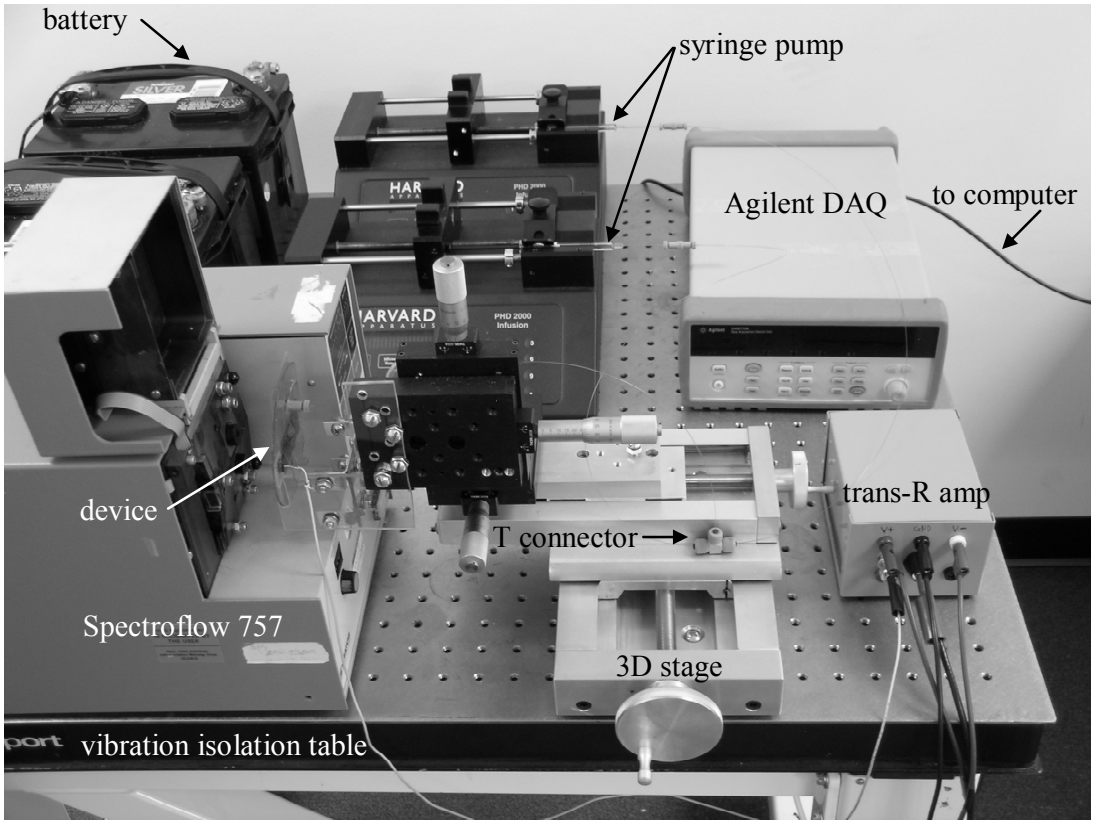

Figure 4.11 A picture of experimental setup.

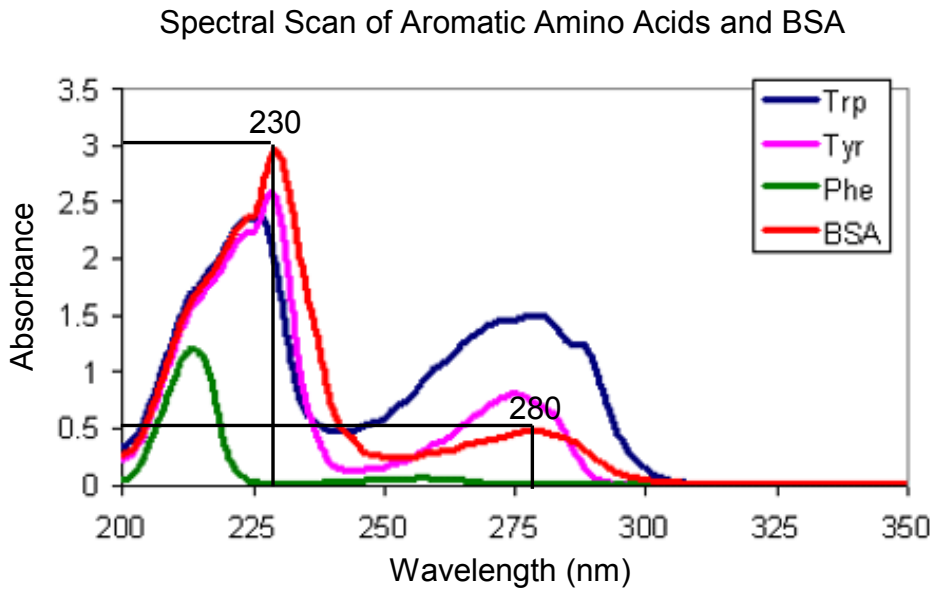

Figure 4.12 Absorbance spectral scans of aromatic amino acids and bovine serum albumin (BSA).

4.3.3 Experimental Protocol

Before each experiment, BSA sample was pumped through the capillary, which connected the BSA sample syringe to the T-connector, to set the interface of BSA sample and Tris buffer at the T-connector. Then the microchannel was flushed with Tris buffer for 10 min. Following warm up of the deuterium lamp for at least 5 min, Tris and BSA were alternately pumped through the channel for 10 min at a flow rate of 5 μL/min. This cycle was repeated 3 times. The schematic of the flow cycles for this experiment is shown in Figure 4.13. The BSA samples with concentrations ranging from 0.001 – 1 mg/mL were tested by using this experimental setup. A 10 min Tris buffer flush in the microchannel was performed between changes in BSA concentration.

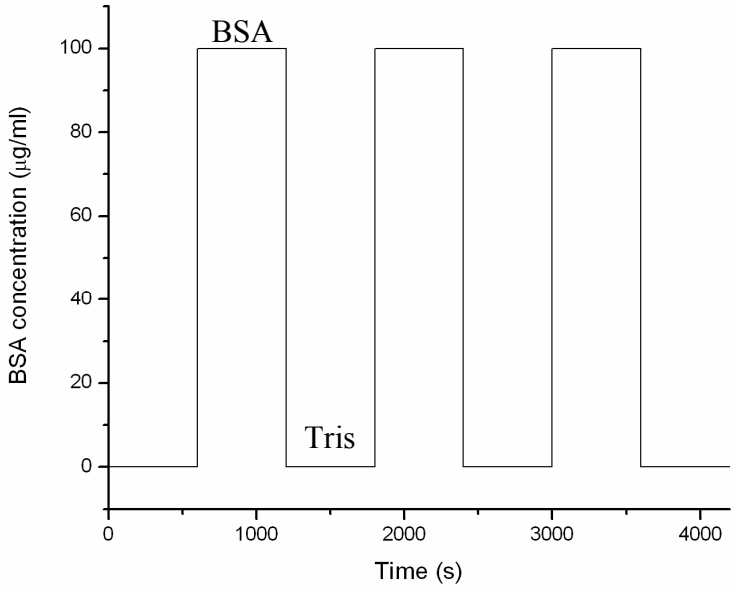

Figure 4.13 Schematic of analyte flow cycles

4.4 Results and Discussion

Four devices with different photodiode chip sizes and different microchannel dimensions were fabricated and tested. Table 4.2 summarizes the design parameters for the four devices. In this table, the detection cell volume is defined as the product of the channel width, channel depth, and PD width, while the detector volume is defined as the product of the channel depth and the square of the PD width. The limit of detection (LOD) for each design, set at 3 times the noise level and discussed in the following, are also given in the table. The mass LOD is specified as a range defined by the product of the concentration LOD and either the minimum or maximum detection volume. The upper limit of detection was constrained by protein precipitation, observed at concentrations above 50 mg/mL. While not evaluated for each test, the dynamic range, given by the ratio of the predetermined precipitation limit to the concentration LOD, is also provided in Table 4.2.

Table 4.2 Summary of design parameters and characterization results for four different detection platform designs.

		Design 1	Design 2	Design 3	Design 4
Channel dimension	width	200 µm	500 µm	200 µm	90 µm
	depth	185 µm	400 µm	60 µm	215 µm
Active area of photodiode chip		$(160\ \mu m)^2$	$(70\ \mu m)^2$	$(70\ \mu m)^2$	$(25\ \mu m)^2$
Detection volume	minimum	4.74 nL	1.96 nL	0.29 nL	0.13 nL
	maximum	5.92 nL	14.0 nL	0.84 nL	0.48 nL
Limit of Detection BSA @ 230 nm	concentration	2 µg/mL (30.1 nM)	1 µg/mL (15.2 nM)	15 µg/mL (227.3 nM)	5 µg/mL (75.8 nM)
	mass	9.5 – 11.8 pg (144 – 179 amol)	2.0 – 28.0 pg (30 – 212 amol)	4.3 – 12.6 pg (66 – 191 amol)	0.6 – 2.4 pg (9.8 – 36 amol)
Dynamic range		25,000	50,000	3,300	10,000

A typical time-domain signal from the transimpedance amplifier (design 2, 100 μg/mL BSA) is shown in Figure 4.14. The integrated photodiode exhibits a current response when the BSA sample was introduced to the microchannel. The output signal from the transimpedance amplifier is about 0.25 V, and the noise level is about 0.8 mV.

Figure 4.15 exhibits the processed time-domain data traces showing normalized changes in measured absorbance for three analyte concentrations (BSA at 100, 10, and 1 μg/mL) using chip design 2. As evident from this figure, BSA can be detected at 1 μg/mL (15.2 nM) using a photodiode chip with a 70 μm × 70 μm active area. This is substantially lower than the μM detection limits typically offered by capillary-based UV absorbance detectors with equivalent optical pathlengths [100, 103]. Furthermore, by reducing the detection volume using a photodetector chip with a smaller active area of 25 μm × 25 μm, a mass LOD as low as 9.8 amol (0.6 pg) was achieved (see Table 4.2). This detection limit is 2–3 orders of magnitude smaller than commercial UV absorbance detectors, and rivals many fluorescence-based detection methods which typically offer mass LODs on the order of 1–10 pg.

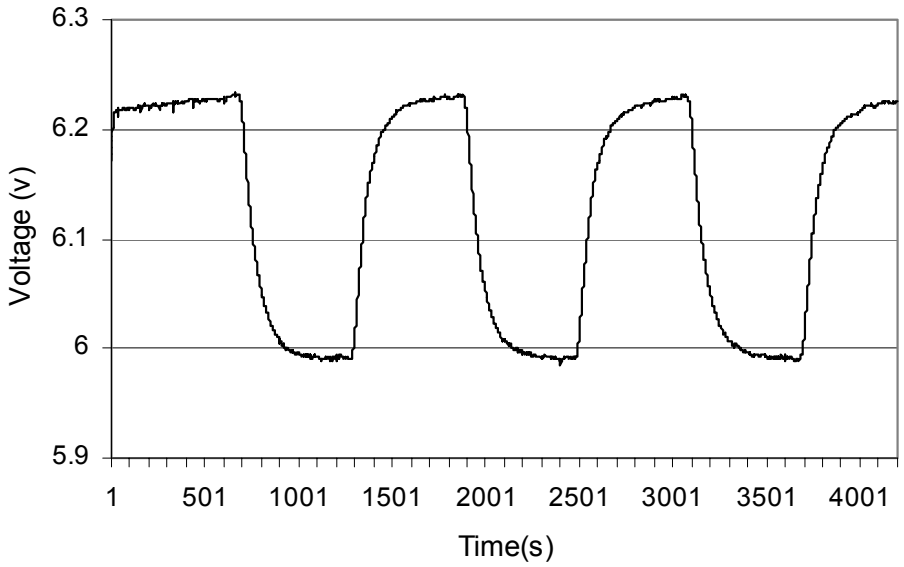

Figure 4.14 A typical time-domain data trace (design 2, 100 μg/mL BSA).

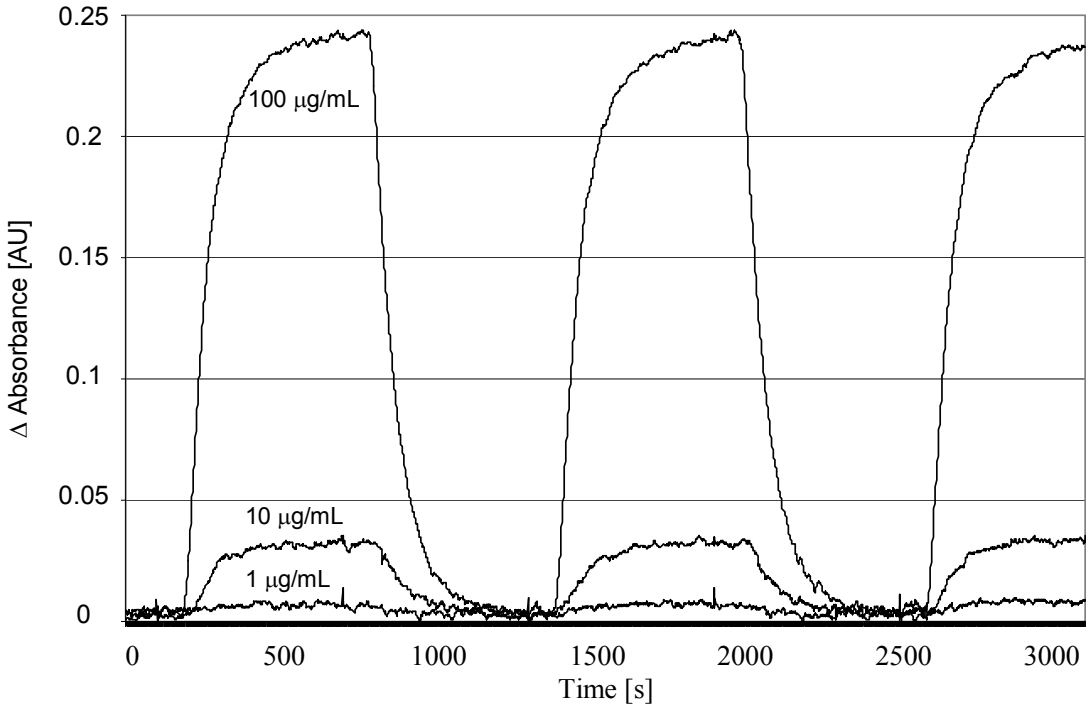

Figure 4.15 Processed time-domain data traces showing normalized changes in measured absorbance for three analyte concentrations (BSA at 100, 10, and 1 μg/mL) using chip design 2 (see Table 4.2). The BSA solutions were pumped at 5 μL/min, with flow switch on/off each 600 sec.

The results of the BSA dilution measurements for each design are shown in Figure 4.16. In this figure, the data points are average absorption measurements performed over 3 on/off cycles, with error bars reflecting +/-1 σ for each set of measurements. As can be seen from Figure 4.16, all designs exhibit the expected linearity between absorbance and analyte concentration, with some deviation at low concentrations. The detection limits for each design are summarized in Table 4.2.

Based on the Lambert-Beer relation, $A = log(I_o/I) = \varepsilon cl$, where A is the absorbance, I_o is the intensity of the incident light, I is the intensity of the transmitted light, ε is the analyte's molar extinction coefficient, l is the optical path length, and c is the analyte concentration [112], the sensitivity of the detection system can be increased linearly by increasing the optical path length. The four designs used in this study have different channel depths ranging from 60 μm to 400 μm. While designs with deeper channels generally offer lower detection limits, the relationship is not linear for several reasons. First, the terminal optics in the UV source are designed for focusing into a cylindrical flow cell rather than a planar chip, and thus the emitted light is not collimated. Second, the UV source spot size is larger than the active area of the photodiode chips, while at the same time the active area is smaller than the width of the microchannels, both by varying amounts depending on the specific design. Because of these factors, different amounts of optical scatter are expected from the four designs, thereby influencing the ultimate sensitivity of each detection system. In addition, the integrated photodiodes with smaller active area usually generate small output signal, but the background noise mainly from the electronics is the same. So

the signal-to-noise ratio of the integrated photodiodes with smaller active area tends to be small, which will affect the detection limit.

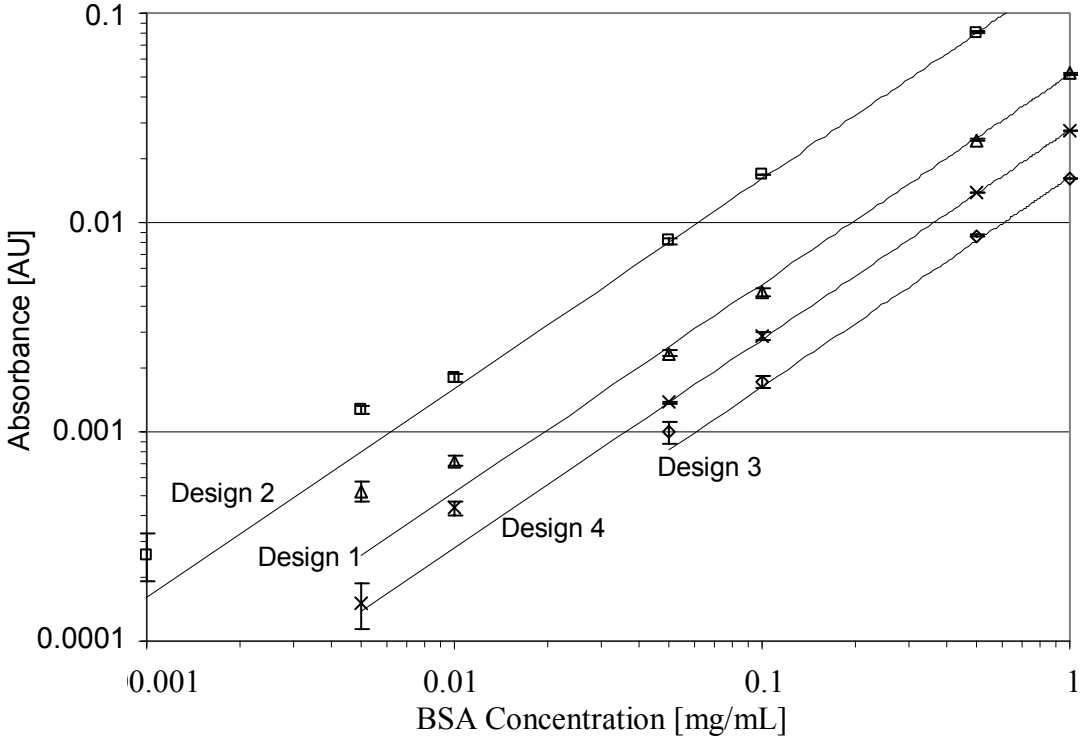

Figure 4.16 Calibration curves for all tested chip designs. Data points are average absorption measurements performed over at least 3 on/off cycles, with error bars reflecting +/-1 σ for each set of measurements.

In commercial UV absorbance detectors designed for nanoscale liquid chromatography (nano-LC), UV is illuminated across the width of a capillary to achieve detection volumes in the low nL range. For the integrated microfluidic system, the photodiode is located directly against the microchannel, enabling

exceptionally small detection volumes. Assuming an ideal case in which collimated light passes through the microchannel and optical dispersion may be neglected, the minimum detection volume is given by the product of channel height and active area of the photodiode. In practice, the UV illumination is not perfectly collimated, and optical dispersion and reflection from the channel surfaces may influence detection sensitivity. Reflections from the channel sidewalls are likely to be particularly significant. Thus, an upper limit on the maximum detection volume is given by the product of the channel height, channel width, and length of the photodiode active area. Both minimum and maximum detection volumes are provided in Table 4.2 for each design.

In UV absorbance cells used for nano-LC, larger detection volumes generally imply lower spatial resolution due to longer path lengths along the axis of the capillary. For the integrated photodiode detectors, the spatial resolution is defined purely by the length of the active area oriented along the microchannel axis. This feature enables exceptionally high spatial resolution through the use of detectors with active areas as small as $(25\ \mu m)^2$. For maximum sensitivity and minimum detection volume, the ideal device would possess a deep and narrow microchannel, and a photodiode with an active area matched to the microchannel width. This design approach can provide high sensitivity due to the longer optical path length (deep channel), small detection volume due to the small width of the channel (narrow channel), and high special resolution due to the small active area of the integrated photodiode.

4.5 Summary

The ability to integrate UV photodiodes into polymer microfluidic systems enables the fabrication of UV absorption detectors with sub-nL detection volumes and excellent detection limits. As demonstrated in Table 4.3, the mass detection limit of this fabricated detection platform is one order lower than the standard capillary cell, and the minimum detection volume (0.13 nL) is much smaller than the smallest capillary flow cell volume (3 nL) that Dionex Corporation can provide.

Table 4.3 Comparison of the detection limit and minimum detection volume between standard capillary flow cell and the integrated polymer-based detection platform.

Detection Platform	Mass detection limit (moles)	Concentration detection limit (molar)	Minimum detection volume (nL)
Capillary cell	10^{-13} - 10^{-16}	10^{-5} - 10^{-7}	3 (Dionex)
Present work	10^{-16} - 10^{-17}	10^{-7} - 10^{-8}	0.13-14

Because the silicon-in-plastic technology allows photodiodes to be seamlessly combined with microfluidic channels with no interface gaps, the integrated detectors may potentially be used for monitoring protein separations without resolution loss due to sample dispersion when passing through the detection region. Furthermore, the low detection volume and high spatial resolution of the detectors is uniquely suited to effective monitoring of microfluidic separations. Further improvements in minimum detectible signal can be realized through the use of a differential measurement

approach and improved interface electronics. With the emergence of low-cost silicon LEDs operating in the mid-UV range, it may also be possible to combine both excitation and detection in a fully integrated, low power analytical tool.

Chapter 5

Conclusions and Future Work

5.1 Conclusions

The presented silicon-in-plastic microfabrication method involves seamlessly integrating individual microfabricated silicon chips into a larger polymer substrate, where the silicon components provide enhanced system functionality, and the plastic substrate provides low-cost fluid handling. This technology employs simple polymer processing techniques that are amenable to mass production. Many polymer materials have been used in this study to form the microfluidic networks, including PC, COC, PDMS, polyimide and parylene. Two microfluidic systems using this silicon-in-plastic microfabrication technology are developed and discussed. These systems are "Water-Based Chemical Monitoring System" and "Integrated UV Absorbance Detection System".

The water monitoring system based on microhotplate gas sensor and polymer microfluidics was designed to monitor and characterize volatile organic compounds (VOCs) in water supply systems. In this study, on-chip solvent extraction was

achieved by evaporation of the solvent using an air-liquid two-phase flow system, which consists of two microfabricated polymer channels separated by a porous hydrophobic polytetrafluoroethylene (PTFE) membrane. The theoretical performance of the air-liquid two-phase flow system was evaluated by solving 2-D convective-diffusion equations. A detailed vapor transport model incorporating all relevant transport phenomena relating initial contaminant concentrations in the source water to final gas concentration at the gas sensor was developed. By using the model, transport physics can be simulated for a variety of chip geometries and flow conditions to optimize the system design. Characterization of the water monitoring system was performed by using methanol as a test analyte, while the integrated gas sensor was operated in a rapid temperature-programmed sensing (TPS) mode. In this study, a Guterman-Boger artificial neural network (ANN) modeling approach has been applied to identify the small differences between TPS patterns, which can not be identified by human eyes. This system also demonstrated the ability to detect organic chemical contaminants listed by the U.S. Environmental Protection Agency, such as toluene and 1,2 dichloroethane. Since the space velocity (related to the flow rate) of gas molecules can be precisely controlled in a wide range inside the microchannel, this system was used to perform research on the relationship between the flow rate and sensor response.

The silicon-in-plastic microfabrication was also used to integrate UV photodetectors into polymer microfluidic systems without interface gaps. The integrated detectors can be used for monitoring protein separations without resolution loss due to sample

dispersion when passed through the detection region. Detection platforms fabricated using this approach exhibit excellent detection limits down to 1.5×10^{-8} M for bovine serum albumin (BSA) as a model protein. The integration of photodetector inside the microchannel enables the UV absorption detectors sub-nL detection volumes. Furthermore, the low detection volume and high spatial resolution of the detectors are uniquely suited to effective monitoring of microfluidic separations.

5.2 Significant Contributions

The work presented in this dissertation is novel in the polymer-based integrated microfluidics areas. The significant contributions of this work are:

- The development of silicon-in-plastic microfabrication technology, which can be used for a range of applications in BioMEMS and microfluidics areas.
- The development of micro scale solvent extraction system using low-cost polymer substrates and PTFE membranes.
- Demonstration of a water contaminant monitoring system based on polymer microfluidics and microhotplate gas sensors.
- Development of a new vapor transport model based on air-liquid two-phase flow system.
- Demonstration of an integrated UV absorbance detection system based on polymer microfluidics and commercial photodetectors with substantially enhanced performance over existing capillary and microfluidic detectors.

5.3 Future Work

Although functional silicon chips have been seamlessly integrated into polymer-based microfluidic system using silicon-in-plastic microfabrication, there are several areas

in the fabrication process which need to be improved. As can be seen from Figure 2.2, the surface of silicon chip is within several microns of the polymer substrate due to the shrinkage of epoxy. There are a variety of epoxies that can be used in this fabrication. Optimization work needs to be performed to choose the optimal epoxies with low curing shrinkage, high glass transition temperature and good chemical resistance, which can level the surfaces of silicon chip and polymer substrate to within 1 μm. In addition, the electrical interconnection to polymer devices in this study relied on silver filled conductive epoxy, which is subject to oxidation and changes in electrical properties with time and temperature. Simple and reliable interconnection similar to the printed circuit boards needs to be developed.

With the microfluidic gas sensing device, the fundamental research on the relationship between gas flow rate and sensor response was performed. The flow rate of the gas analyte may have some effects on the response of the microhotplate gas sensor since it may affect the heat and the mass exchange of the heterogeneous catalytic reaction on the sensing film [88]. In order to explain the experimental phenomena, a theoretical model regarding the velocity of gas molecules passing across the sensing film needs to be developed. The fabricated water monitoring system was characterized using methanol as the testing sample. But the U.S. Environmental Protection Agency (EPA) lists 53 organic contaminants and their maximum contaminant levels (MCLs) for safe drinking water. Using the optimized system, several available solvents in EPA's list will be tested on the water monitoring system.

For the integrated UV absorbance detection system, further improvements in minimum detectable signal can be realized through the use of a differential measurement approach and improved interface electronics. And the protein separation channels can be bonded to this UV absorbance detection platform to conduct CE or Gel electrophoresis. With the emergence of low-cost silicon LEDs operating in the mid-UV range, it may be possible to combine both excitation and detection in polymer-based microfluidic system to increase the UV intensity, eliminate the need for UV transparent layers, and miniaturize the whole bioanalysis system. Despite the benefits of PDMS fabrication methods, the material suffers from several key drawbacks. COC may be preferred for future development due to its optical clarity, excellent chemical resistance, low water absorption, and low gas permeability.

Another interesting direction for future work involves the integration of piezoelectric microbeam resonators with polymer microfluidics for biosensing applications. Microresonators have been shown to be a good candidate as a mechanical filter in radio communication systems. Some piezoelectric resonators based on ZnO [129, 130], PZT [131], and AIN [132, 133] have been reported. Recently the piezoelectric microbeam resonators are being investigated as sensitive mass detectors for applications such as chemical and biological sensing [47, 134-137]. The binding of biomelocules can be measured through resonant frequency shifts due to the mass loading, or beam deflection due to surface stress changes. The major advantage of such detectors is that the sensitivity of the devices is sufficient to detect the binding of

a single large biomolecule without labeling. Furthermore, such devices can be incorporated in optically accessible microchannels to realize very high sensitive, inexpensive and extremely small microsensors.

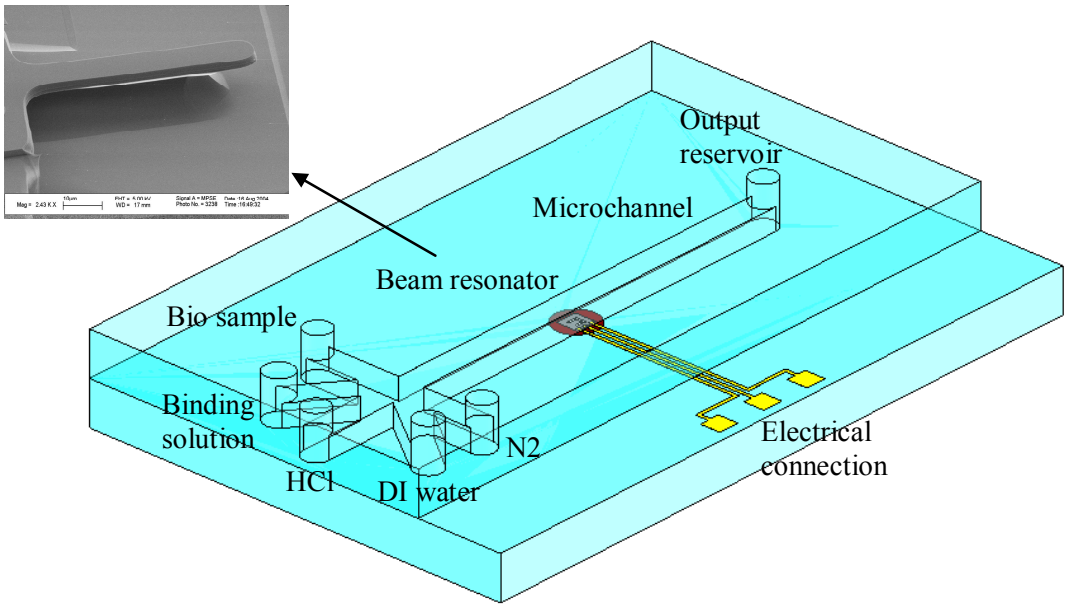

Figure 5.1 Device schematic of the integrated biomolecule detection system using piezoelectric AlGaAs microbeams and polymer microfluidics.

Using silicon-in-plastic microfabrication techonology, the microbeam resonator and microfluidic networks can be fabricated on a polymer microchip. The schematic of the integrated biomelocule detection system is shown in Figure 5.1. The detection system includes two functional components, piezoelectric AlGaAs microbeam [138], and polymer based microfluidic network. Initial test was performed on 100 μm AlGaAs doubly clamped beam using Olego-thiol (OT) as the sample biomelocule. The testing results are shown in Table 5.1. The fully integrated device is still under development. In the future design, an array of microbeams with specific binding

surface can be integrated into LOC devices. The number of bound molecules on each microbeam is quantified as proportional to the measured frequency shift with a proportionality constant determined experimentally and verified by modeling of the mechanical response of the system.

Table 5.1 Initial test results on a 100 μm AlGaAs doubly clamped beam using oligo-thiol (OT) as a binding melocule.

Beam #	f_r (kHz) without OT binding	f_r (kHz) with OT binding
1	841	837.5
1	841	837.5

BIBLIOGRAPHY

1. S. C. Terry, J. H. Jerman and J. B. Angell, "Gas-Chromatographic Air Analyzer Fabricated On A Silicon-Wafer," *IEEE Transactions on Electron Devices*, vol. ED-26, No. 12, pp. 1880-1886, 1979.
2. A. Manz, N. Graber and H. M. Widmer, "Miniaturized Total Chemical-Analysis Systems - A Novel Concept For Chemical Sensing," *Sensors and Actuators B-Chemical*, vol. 1, No. 1-6, pp. 244-248, 1990.
3. H. Becker and C. Gartner, "Polymer Microfabrication Methods for Microfluidic Analytical Applications," *Electrophoresis*, vol. 21, No. 1, pp. 12-26, 2000.
4. B. N. Johnson, K. Handique, T. S. Sammarco, J. R. Webster, P. F. Man, S. N. Brahmasandra, D. T. Burke, C. H. Mastrangelo and M. A. Burns, "Microfabricated Components for Integrated Chemical Analysis," in *Proceedings of the Symposium on Microstructures and Microfabricated Systems IV*, Boston, MA, USA, pp. 43-53, 1998.
5. L. W. Lin, "Microscale Thermal Bubble Formation: Thermophysical Phenomena and Applications," *Microscale Thermophysical Engineering*, vol. 2, No. 2, pp. 71-85, 1998.
6. J. H. Tsai and L. Lin, "A Thermal Bubble Actuated Micro Nozzle-Diffuser Pump," in *Proceedings IEEE 14th IEEE International Conference on Micro Electro Mechanical Systems*, Interlaken, Switzerland, pp. 409-412, 2001.
7. R. Zengerle, S. Kluge, M. Richter and A. Richter, "A Bidirectional Silicon Micropump," in *Proceedings IEEE 8th Annual International Conference on Micro Electro Mechanical Systems*, Amsterdam, Netherlands, pp. 19-24, 1995.
8. P. W. Barth, "Silicon Microvalves for Gas Flow Control," in *Proceedings of the International Solid-State Sensors and Actuators Conference - TRANSDUCERS '95*, Stockholm, Sweden, pp. 276-277, 1995.

9. L. Smith and B. Hok, "A Silicon Self-aligned Non-reverse Valve," in *Proceedings of the International Solid-State Sensors and Actuators Conference -TRANSDUCERS '91*, San Francisco, CA, USA, pp. 1049-1051, 1991.

10. M. A. Roberts, J. S. Rossier, P. Bercier and H. Girault, "UV Laser Machined Polymer Substrates for The Development of Microdiagnostic Systems," *Analytical Chemistry*, vol. 69, No. 11, pp. 2035-2042, 1997.

11. L. J. Guerin, M. Bossel, M. Demierre, S. Calmes and P. Renaud, "Simple and Low Cost Fabrication of Embedded Micro-channels by Using a New Thick-film Photoplastic," in *Proceedings of International Solid State Sensors and Actuators Conference (Transducers '97)*, Chicago, IL, USA, pp. 1419-1422, 1997.

12. R. Pethig, J. P. H. Burt, A. Parton, N. Rizvi, M. S. Talary and J. A. Tame, "Development of Biofactory-on-a-chip Technology Using Excimer Laser Micromachining," *Journal of Micromechanics and Microengineering*, vol. 8, No. 2, pp. 57-63, 1998.

13. P. Renaud, H. van Lintel, M. Heuschkel and L. Guérin, "Photo-polymer Microchannel Technologies and Applications," in *Micro Total Analysis Systems 1998*, Banff, Canada, pp. 17-22, 1998.

14. K. Ikuta, S. Maruo, Y. Fukaya and T. Fujisawa, "Biochemical IC Chip Toward Cell Free DNA Protein Synthesis," in *Proceedings IEEE 11th Annual International Conference on Micro Electro Mechanical Systems*, Heidelberg, Germany, pp. 131-136, 1998.

15. P. F. Man, D. K. Jones and C. H. Mastrangelo, "Microfluidic Plastic Capillaries on Silicon Substrates: A New Inexpensive Technology for Bioanalysis Chips," in *Proceedings IEEE The 10th Annual International Workshop on Micro Electro Mechanical Systems*, Nagoya, Japan, pp. 311-316, 1997.

16. L. Martynova, L. E. Locascio, M. Gaitan, G. W. Kramer, R. G. Christensen and W. A. MacCrehan, "Fabrication of Plastic Microfluid Channels by

Imprinting Methods," *Analytical Chemistry*, vol. 69, No. 23, pp. 4783-4789, 1997.

17. F. Rosenberger, E. Jones, C. Lee and D. L. DeVoe, "High Pressure Thermal Bonding for Sealing of Plastic Microstructures," in *Micro Total Analysis Systems 2002*, Nara, Japan, pp. 404-406, 2002.
18. J. C. McDonald, D. C. Duffy, J. R. Anderson, D. T. Chiu, H. K. Wu, O. J. A. Schueller and G. M. Whitesides, "Fabrication of Microfluidic Systems in Poly(dimethylsiloxane)," *Electrophoresis*, vol. 21, No. 1, pp. 27-40, 2000.
19. K. P. Kamper, J. Dopper, W. Ehrfeld and S. Oberbeck, "A Self-filling Low-cost Membrane Micropump," in *Proceedings IEEE Eleventh Annual International Workshop on Micro Electro Mechanical Systems*, Heidelberg, Germany, pp. 432-437, 1998.
20. Y. Su and L. Lin, "Localized Plastic Bonding for Micro Assembly, Packaging and Liquid Encapsulation," in *Proceedings 14th IEEE International Conference on Micro Electro Mechanical Systems*, Interlaken, Switzerland, pp. 50-53, 2001.
21. L. J. Kricka, P. Fortina, N. J. Panaro, P. Wilding, G. Alonso-Amigo and H. Becker, "Fabrication of Plastic Microchips by Hot Embossing," *Lab On A Chip*, vol. 2, No. 1, pp. 1-4, 2002.
22. C. Jiang, S. O'Neill and W. Hai-Sheng, "Application of Solvent Bonding Technique to Achieve a Highly Reliable Low-cost CATV PIN Package," in *Proceedings of the SPIE - The International Society for Optical Engineering*, Dallas, TX, USA, pp. 153-160, 1998.
23. T. Thorsen, S. J. Maerkl and S. R. Quake, "Microfluidic Large-Scale Integration," *Science*, vol. 298, No. 5593, pp. 580-584, 2002.
24. C. Kimball, *Integrated Temperature Measurement and Control in Polymer Microfluidic Systems*, Ph. D. thesis, Department of Mechanical Engineering, University of Maryland, College Park, 2003.
25. J. R. Webster, M. A. Burns, D. T. Burke and C. H. Mastrangelo, "Monolithic capillary electrophoresis device with integrated fluorescence detector," *Analytical Chemistry*, vol. 73, No. 7, pp. 1622-1626, 2001.

26. P. Sethu, H. Yu, P. Grodzinski and C. H. Mastrangelo, "Fabrication of Genetic Analysis Microsystems Using Plastic Microcasting," in *Solid-State Sensor and Actuator Workshop*, Hilton Head Island, SC, USA, pp. 175-178, 2000.
27. K. Uchiyama, W. Xu, J. M. Qiu and T. Hobo, "Polyester Microchannel Chip for Electrophoresis - Incorporation of A Blue LED as Light Source," *Fresenius Journal of Analytical Chemistry*, vol. 371, No. 2, pp. 209-211, 2001.
28. L. Zhu, D. C. Meier, C. Montgomery, S. Semancik and D. L. DeVoe, "A Water-Based Chemical Monitoring System Using Integrated Silicon-in-Plastic Microfabrication," in *Micro Total Analysis Systems 2005*, Boston, MA, pp. 482-484, 2005.
29. L. Zhu, C. Kimball, N. Sniadeck, M. Beamesderfer, S. Semancik and D. L. DeVoe, "Integrated Microfluidic Gas Sensor for Water Monitoring," in *Micro Total Analysis Systems 2003*, Squaw Valley, CA, pp. 1231-1234, 2003.
30. T. H. Wang, S. M. Ho, K. M. Chen and A. Hung, "Temperature Effect On Pl Cu Interface," *Journal of Applied Polymer Science*, vol. 47, No. 6, pp. 1057-1064, 1993.
31. D. J. Liaw and P. Chang, "Synthesis and Characterization of Polycarbonates Based on Bisphenol S by Melt Transesterification," *Journal of Polymer Science Part A-Polymer Chemistry*, vol. 35, No. 12, pp. 2453-2460, 1997.
32. J. I. Kroschwitz and M. Howe-Grant, *Encyclopedia of Chemical Technology, Fourth Edition: Supplement Volume: Aerogels to Xylylene Polymers*, New York: Wiley, 1998.
33. R. D. Tacito and C. Steinbruchel, "Fine-Line Patterning of Parylene-n by Reactive Ion Etching for Application as an Interlayer Dielectric," *Journal of The Electrochemical Society*, vol. 143, No. 6, pp. 1974-1977, 1996.
34. E. Meng and T. Yu-Chong, "Parylene Etching Techniques for Microfluidics and BioMEMS," in *Proceedings 18th IEEE International Conference on Micro Electro Mechanical Systems*, Miami Beach, FL, USA, pp. 568-571, 2005.

35. D. F. Weston, T. Smekal, D. B. Rhine and J. Blackwell, "Fabrication of Microfluidic Devices in Silicon and Plastic Using Plasma Etching," *Journal of Vacuum Science & Technology B*, vol. 19, No. 6, pp. 2846-2851, 2001.

36. D. L. Pugmire, E. A. Waddell, R. Haasch, M. J. Tarlov and E. Locascio, "Surface Characterization of Laser-ablated Polymers Used for Microfluidics," *Analytical Chemistry*, vol. 74, No. 4, pp. 871-878, 2002.

37. M. Heckele, W. Bacher and K. D. Muller, "Hot Embossing - The Molding Technique for Plastic Microstructures," *Microsystem Technologies*, vol. 4, No. 3, pp. 122-124, 1998.

38. S. Li, C. B. Freidhoff, R. M. Young and R. Ghodssi, "Fabrication of Micronozzles Using Low-temperature Wafer-level Bonding with SU-8," *Journal of Micromechanics and Microengineering*, vol. 13, No. 5, pp. 732-738, 2003.

39. A. Szczurek, P. M. Szecowka and B. W. Licznerski, "Application of Sensor Array and Neural Networks for Quantification of Organic Solvent Vapours in Air," *Sensors and Actuators B-Chemical*, vol. 58, No. 1-3, pp. 427-432, 1999.

40. C. K. Ho and R. C. Hughes, "In-situ Chemiresistor Sensor Package for Real-time Detection of Volatile Organic Compounds in Soil and Groundwater," *Sensors*, vol. 2, No. 1, pp. 23-34, 2002.

41. C. K. Ho, M. T. Itamura, M. Kelley and R. C. Hughes, "Review of Chemical Sensors for In-Situ Monitoring of Volatile Contaminants," SANDIA, *SANDIA REPORT* 2001.

42. S. D. Richardson and T. A. Ternes, "Water analysis: Emerging contaminants and current issues," *Analytical Chemistry*, vol. 77, No. 12, pp. 3807-3838, 2005.

43. S. D. Richardson, "Water analysis," *Analytical Chemistry*, vol. 73, No. 12, pp. 2719-2734, 2001.

44. B. B. Looney and R. W. Falta, *Vadose Zone Science and Technology Solutions*, Columbus, OH: Battelle Press, 2000.

45. C. K. Ho, E. R. Lindgren, K. S. Rawlinson, L. K. McGrath and J. L. Wright, "Development of a Surface Acoustic Wave Sensor for In-situ Monitoring of Volatile Organic Compounds," *Sensors*, vol. 3, No. 7, pp. 236-247, 2003.

46. H. Kohler, J. Rober, N. Link and I. Bouzid, "New Applications of Tin Oxide Gas Sensors - I. Molecular Identification by Cyclic Variation of The Working Temperature and Numerical Analysis of The Signals," *Sensors and Actuators B-Chemical*, vol. 61, No. 1-3, pp. 163-169, 1999.

47. C. Vancura, Y. Li, J. Lichtenberg, F. Josse and A. Hierlemann, "Detection of Volatile Organic Compounds in Liquid Environments Using Fully Integrated CMOS Resonant Cantilevers," in *Micro Total Analysis Systems 2005*, Boston, pp. 1170-1173, 2005.

48. C. Lu, W. Tian, W. H. Steinecker, A. Guyon, M. Agah, M. C. Oborny, R. D. Sacks, K. D. Wise, S. W. Pang and ZellersE.T., "Functionally Integrated MEMS Micro Gas Chromatograph Subsystem," in *Micro Total Analysis Systems 2003*, Squaw Valley, pp. 411-414, 2003.

49. H. Nanto, N. Dougami, T. Mukai, T. Ogawa, E. Kusano and A. Kinbara, "Smart Chemical Sensor using Polymer-film-coated Quartz Resonator for Hydrocarbon and Organic Solvent Gases," in *Proceedings of the SPIE - The International Society for Optical Engineering*, Boston, MA, USA, pp. 260-265, 1999.

50. R. Mehandru, B. Luo, B. S. Kang, J. Kim, F. Ren, S. J. Pearton, C. C. Pan, G. T. Chen and J. I. Chyi, "AlGaN/GaN HEMT Based Liquid Sensors," *Solid-State Electronics*, vol. 48, No. 2, pp. 351-353, 2004.

51. T. Seiyama, A. Kato, K. Fujiishi and M. Nagatani, "A New Detector For Gaseous Components Using Semiconductive Thin Films," *Analytical Chemistry*, vol. 34, No. 11, pp. 1502-1507, 1962.

52. N. Taguchi, Patent No. S45-38200, Japan.

53. F. a. S. Inc., "Sensor Market' 94: a Strategic Assessment of the International Market for Sensors," 1994.

54. S. Semancik, R. E. Cavicchi, M. C. Wheeler, J. E. Tiffany, G. E. Poirier, R. M. Walton, J. S. Suehle, B. Panchapakesan and D. L. DeVoe, "Microhotplate

Platforms for Chemical Sensor Research," *Sensors and Actuators B-Chemical*, vol. 77, No. 1-2, pp. 579-591, 2001.

55. J. S. Suehle, R. E. Cavicchi, M. Gaitan and S. Semancik, "Tin Oxide Gas Sensor Fabricated Using Cmos Micro-Hotplates And Insitu Processing," *IEEE Electron Device Letters*, vol. 14, No. 3, pp. 118-120, 1993.
56. S. Semancik, R. E. Cavicchi, K. G. Kreider, J. S. Suehle and P. Chaparala, "Selected-area Deposition of Multiple Active Films for Conductometric Microsensor Arrays," *Sensors and Actuators B-Chemical*, vol. 34, No. 1-3, pp. 209-212, 1996.
57. S. Semancik and R. Cavicchi, "Kinetically Controlled Chemical Sensing Using Micromachined Structures," *Accounts of Chemical Research*, vol. 31, No. 5, pp. 279-287, 1998.
58. R. E. Cavicchi, R. M. Walton, M. Aquino-Class, J. D. Allen and B. Panchapakesan, "Spin-on Nanoparticle Tin Oxide for Microhotplate Gas Sensors," *Sensors and Actuators B-Chemical*, vol. 77, No. 1-2, pp. 145-154, 2001.
59. R. E. Cavicchi, J. S. Suehle, K. G. Kreider, B. L. Shomaker, J. A. Small, M. Gaitan and P. Chaparala, "Growth Of Sno2 Films On Micromachined Hotplates," *Applied Physics Letters*, vol. 66, No. 7, pp. 812-814, 1995.
60. R. E. Cavicchi, J. S. Suehle, K. G. Kreider, M. Gaitan and P. Chaparala, "Fast Temperature-Programmed Sensing For Micro-Hotplate Gas Sensors," *IEEE Electron Device Letters*, vol. 16, No. 6, pp. 286-288, 1995.
61. D. C. Meier, C. J. Taylor, R. E. Cavicchi, E. W. V, M. W. Ellzy, K. B. Sumpter and S. Semancik, "Chemical warfare agent detection using MEMS-compatible microsensor arrays," *IEEE Sensors Journal*, vol. 5, No. 4, pp. 712, 2005.
62. M. Tokeshi, T. Minagawa and T. Kitamori, "Integration of a Microextraction System on a Glass Chip: Ion-Pair Solvent Extraction of Fe(II) with 4,7-diphenyl-1,10-phenanthrolinedisulfonic Acid and Tri-n-octylmethylammonium Chloride," *Analytical Chemistry*, vol. 72, No. 7, pp. 1711-1714, 2000.

63. K. E. Bean, "Anisotropic Etching Of Silicon," *IEEE Transactions On Electron Devices*, vol. 25, No. 10, pp. 1185-1193, 1978.

64. F. I. Chang, R. Yeh, G. Lin, P. B. Chu, E. Hoffman, E. J. J. Kruglick, K. S. J. Fister and M. H. Hecht, "Gas-phase Silicon Micromachining with Xenon Difluoride," in *Proceedings of the SPIE - The International Society for Optical Engineering*, Austin, TX, USA, pp. 117-128, 1995.

65. M. Paranjape, A. Pandy, S. Brida, L. Landsberger, M. Kahrizi and M. Zen, "Dual-doped TMAH Silicon Etchant for Microelectromechanical Structures and Systems Applications," *Journal of Vacuum Science & Technology A-Vacuum Surfaces and Films*, vol. 18, No. 2, pp. 738-742, 2000.

66. J. T. A. Kovacs, *Micromachined Transducers Sourcebook*. McGraw-Hill Boston, MA: WCB/McGraw-Hill, 1998.

67. J. Shaw, R. Nudd, B. Naik, C. Turner, D. Rudge, M. Benson and A. Garman, "Liquid/Liquid Extraction Systems Using Micro-Contactor Arrays," in *Micro Total Analysis Systems 2000*, Dordrecht, Netherlands, pp. 371-374, 2000.

68. W. Ehrfeld, V. Hessel and H. Löwe, *Microreactors: New Technology for Modern Chemistry*, Weinheim; Chichester: Wiley-VCH, 2000.

69. B. Zhao, J. S. Moore and D. J. Beebe, "Surface-directed Liquid Flow Inside Microchannels," *Science*, vol. 291, No. 5506, pp. 1023-1026, 2001.

70. A. Aota, M. Nonaka, A. Hibara and T. Kitamori, "Micro Counter-current Flow System for Highly Efficient Extraction," in *Micro Total Analysis Systems 2003*, Squaw Valley, CA, pp. 441-444, 2003.

71. M. Tokeshi, T. Minagawa, K. Uchiyama, A. Hibara, K. Sato, H. Hisamoto and T. Kitamori, "Continuous-Flow Chemical Processing on A Microchip by Combining Microunit Operations and A Multiphase Flow Network," *Analytical Chemistry*, vol. 74, No. 7, pp. 1565-1571, 2002.

72. K. Sato, A. Hibara, M. Tokeshi, H. Hisamoto and T. Kitamori, "Integration of Chemical and Biochemical Analysis Systems into a Glass Microchip," *Analytical Sciences*, vol. 19, No. 1, pp. 15-22, 2003.

73. A. Hibara, M. Nonaka, H. Hisamoto, K. Uchiyama, Y. Kikutani, M. Tokeshi and T. Kitamori, "Stabilization of Liquid Interface and Control of Two-phase

Confluence and Separation in Glass Microchips by Utilizing Octadecylsilane Modification of Microchannels," *Analytical Chemistry*, vol. 74, No. 7, pp. 1724-1728, 2002.

74. W. E. TeGrotenhuis, R. J. Cameron, M. G. Butcher, P. M. Martin and R. S. Wegeng, "Microchannel Devices for Efficient Contacting of Liquids in Solvent Extraction," *Separation Science and Technology*, vol. 34, No. 6-7, pp. 951-974, 1999.
75. D. Huh, Y. C. Tung, H. H. Wei, J. B. Grotberg, S. J. Skerlos, K. Kurabayashi and S. Takayama, "Use of Air-liquid Two-phase Flow in Hydrophobic Microfluidic Channels for Disposable Flow Cytometers," *Biomedical Microdevices*, vol. 4, No. 2, pp. 141-149, 2002.
76. M. Tokeshi, K. Kanda, A. Hibara and T. Kitamori, "On-chip Concentration of Liquid Samples Using an Air-liquid Two-phase Flow," in *Micro Total Analysis Systems 2002*, Nara, Japan, pp. 356-358, 2002.
77. Z. X. Yuan, X. T. Yan and C. F. Ma, "A Study of Coupled Convective Heat and Mass Transfer from Thin Water Film to Moist Air Flow," *International Communications in Heat and Mass Transfer*, vol. 31, No. 2, pp. 291-301, 2004.
78. F. M. White, *Viscous Fluid Flow*. 2nd ed. New York: McGraw-Hill, 1991.
79. G. K. Batchelor, *An Introduction to Fluid Dynamics*, Cambridge, U.P.: Cambridge University Press, 1967.
80. *Perry's chemical engineers' handbook, 7th Ed.*, New York: McGraw-Hill, 1997.
81. W. L. Lyman, W. F. Reehl and D. H. Rosenblatt, *Handbook of chemical property estimation methods: environmental behavior of organic compounds*, Washington, DC: American Chemical Society, 1990.
82. Z. Guo and N. F. Roache, "Overall mass transfer coefficient for pollutant emissions from small water pools under simulated indoor environmental conditions," *Annals Of Occupational Hygiene*, vol. 47, No. 4, pp. 279-286, 2003.

83. J. Crank, *The Mathematics of Diffusion*. second ed. Oxford, [Eng]: Clarendon Press, 1975.

84. C. L. Yaws, *Handbook of transport property data: viscosity, thermal conductivity, and diffusion coefficients of liquids and gases*, Houston, Tex.: Gulf Pub. Co., 1995.

85. R. J. Millington, "Gas Diffusion In Porous Media," *Science*, vol. 130, No. 3367, pp. 100-102, 1959.

86. C. L. Yaws, *Chemical properties handbook: physical, thermodynamic, environmental, transport, safety, and health related properties for organic and inorganic chemicals*, New York: McGraw-Hill, 1999.

87. Z. Boger, D. C. Meier, R. E. Cavicchi and S. Semancik, "Rapid Identification of Chemical Warfare Agents by Artificial Neural Network Pruning of Temperature-programmed Microsensor Databases," *Sensor Letters*, vol. 1, No. 1, pp. 86-92, 2003.

88. J. Ding, *Signal Processing and Dynamic Modeling of Microhotplate Gas Sensors*, Ph. D. thesis, Department of Chemical Engineering, University of Maryland, College Park, 2000.

89. W. S. Winston Ho and K. K. Sirkar, *Membrane Handbook*, New York, NY: Van Nostrand Reinhold, 1992.

90. S. Bendib and O. Francais, "Analytical Study of Microchannel and Passive Microvalve: Application to Micropump Simulator," in *Proceedings of the SPIE - The International Society for Optical Engineering*, Adelaide, SA, Australia, pp. 283-291, 2001.

91. H. Guterman, "Application of Principal Component Analysis to The Design of Neural Networks," *Neural, Parallel & Scientific Computations*, vol. 2, No. 1, pp. 43-54, 1994.

92. "Drinking Water Standards and Health Advisories, EPA 822-R-04-005," U.S.E.P. Agency, Washington, DC, 2004.

93. D. R. Reyes, D. Iossifidis, P. A. Auroux and A. Manz, "Micro Total Analysis Systems. 1. Introduction, Theory, and Technology," *Analytical Chemistry*, vol. 74, No. 12, pp. 2623-2636, 2002.

94. Y. Li, J. S. Buch, F. Rosenberger, D. L. DeVoe and C. S. Lee, "Integration of Isoelectric Focusing with Parallel Sodium Dodecyl Sulfate Gel Electrophoresis for Multidimensional Protein Separations in a Plastic Microfludic Network," *Analytical Chemistry*, vol. 76, No. 3, pp. 742-748, 2004.

95. S. Ekstrom, P. Onnerfjord, J. Nilsson, M. Bengtsson, T. Laurell and G. Marko-Varga, "Integrated Microanalytical Technology Enabling Rapid and Automated Protein Identification," *Analytical Chemistry*, vol. 72, No. 2, pp. 286-293, 2000.

96. J. S. Buch, C. Kimball, F. Rosenberger, W. E. Highsmith, D. L. DeVoe and C. S. Lee, "DNA Mutation Detection in a Polymer Microfluidic Network Using Temperature Gradient Gel Electrophoresis," *Analytical Chemistry*, vol. 76, No. 4, pp. 874-881, 2004.

97. P. A. Auroux, D. Iossifidis, D. R. Reyes and A. Manz, "Micro Total Analysis Systems. 2. Analytical Standard Operations and Applications," *Analytical Chemistry*, vol. 74, No. 12, pp. 2637-2652, 2002.

98. K. Uchiyama, H. Nakajima and T. Hobo, "Detection Method for Microchip Separations," *Analytical and Bioanalytical Chemistry*, vol. 379, No. 3, pp. 375-382, 2004.

99. K. B. Mogensen, H. Klank and J. P. Kutter, "Recent Developments in Detection for Microfluidic Systems," *Electrophoresis*, vol. 25, No. 21-22, pp. 3498-3512, 2004.

100. K. Swinney and D. J. Bornhop, "Detection in Capillary Electrophoresis," *Electrophoresis*, vol. 21, No. 7, pp. 1239-1250, 2000.

101. S. R. Mikkelsen, *Bioanalytical Chemistry*, New York: Hoboken, N.J.: Wiley-Interscience, 2004.

102. A. T. Timperman, K. Khatib and J. V. Sweedler, "Wavelength-Resolved Fluorescence Detection In Capillary Electrophoresis," *Analytical Chemistry*, vol. 67, No. 1, pp. 139-144, 1995.

103. J. P. Landers, *Handbook of Capillary Electrophoresis*, Boca Raton, Fla.: CRC Press, 1997.

104. D. Y. Chen, K. Adelhelm, X. L. Cheng and N. J. Dovichi, "Simple Laser-Induced Fluorescence Detector For Sulforhodamine-101 In A Capillary Electrophoresis System - Detection Limits Of 10 Yoctomoles Or 6 Molecules," *Analyst*, vol. 119, No. 2, pp. 349-352, 1994.

105. Q. F. Xue, Y. M. Dunayevskiy, F. Foret and B. L. Karger, "Integrated Multichannel Microchip Electrospray Ionization Mass Spectrometry: Analysis of Peptides from On-chip Tryptic Digestion of Melittin," *Rapid Communications in Mass Spectrometry*, vol. 11, No. 12, pp. 1253-1256, 1997.

106. C. L. Nilsson and P. Davidsson, "New Separation Tools for Comprehensive Studies of Protein Expression by Mass Spectrometry," *Mass Spectrometry Reviews*, vol. 19, No. 6, pp. 390-397, 2000.

107. I. M. Lazar, R. S. Ramsey, S. Sundberg and J. M. Ramsey, "Subattomole-Sensitivity Microchip Nanoelectrospray Source with Time-of-flight Mass Spectrometry Detection," *Analytical Chemistry*, vol. 71, No. 17, pp. 3627-3631, 1999.

108. D. Snakenborg, K. B. Mogensen and J. P. Kutter, "Optimization of Signal-to noise Ratio in Absorbance Detection by Integration of Microoptical Components," in *Micro Total Analysis Systems 2003*, Squaw Valley, CA, pp. 841-844, 2003.

109. K. W. Ro, B. C. Shim, K. Lim and J. H. Hahn, "Integrated Light Collimating System for Extended Optical-path-length Absorbance Detection in Microchip-based Capillary Electrophoresis," in *Micro Total Analysis Systems 2001*, Monterey, CA, pp. 274-276, 2001.

110. G. Ocvirk, E. Verpoorte, A. Manz, M. Grasserbauer and H. M. Widmer, "High-Performance Liquid-Chromatography Partially Integrated Onto A Silicon Chip," *Analytical Methods and Instrumentation*, vol. 2, No. 2, pp. 74-82, 1995.

111. Z. H. Liang, N. Chiem, G. Ocvirk, T. Tang, K. Fluri and D. J. Harrison, "Microfabrication of a Planar Absorbance and Fluorescence Cell for Integrated Capillary Electrophoresis Devices," *Analytical Chemistry*, vol. 68, No. 6, pp. 1040-1046, 1996.

112. L. Ceriotti, K. Weible, N. F. de Rooij and E. Verpoorte, "Rectangular Channels for Lab-on-a-chip Applications," *Microelectronic Engineering*, vol. 67-8, pp. 865-871, 2003.

113. N. J. Petersen, K. B. Mogensen and J. P. Kutter, "Performance of an In-plane Detection Cell with Integrated Waveguides for UV/Vis Absorbance Measurements on Microfluidic Separation Devices," *Electrophoresis*, vol. 23, No. 20, pp. 3528-3536, 2002.

114. K. B. Mogensen, N. J. Petersen, J. Hubner and J. P. Kutter, "Monolithic Integration of Optical Waveguides for Absorbance Detection in Microfabricated Electrophoresis Devices," *Electrophoresis*, vol. 22, No. 18, pp. 3930-3938, 2001.

115. K. B. Mogensen, J. El-Ali, A. Wolff and J. P. Kutter, "Integration of Polymer Waveguides for Optical Detection in Microfabricated Chemical Analysis Systems," *Applied Optics*, vol. 42, No. 19, pp. 4072-4079, 2003.

116. V. Namasivayam, R. S. Lin, B. Johnson, S. Brahmasandra, Z. Razzacki, D. T. Burke and M. A. Burns, "Advances in On-chip Photodetection for Applications in Miniaturized Genetic Analysis Systems," *Journal of Micromechanics and Microengineering*, vol. 14, No. 1, pp. 81-90, 2004.

117. A. M. Jorgensen, K. B. Mogensen, J. P. Kutter and O. Geschke, "A Biochemical Microdevice with an Integrated Chemiluminescence Detector," *Sensors and Actuators B-Chemical*, vol. 90, No. 1-3, pp. 15-21, 2003.

118. I. Rech, A. Restelli, S. Cova, M. Ghioni, M. Chiari and M. Cretich, "Microelectronic Photosensors for Genetic Diagnostic Microsystems," *Sensors and Actuators B-Chemical*, vol. 100, No. 1-2, pp. 158-162, 2004.

119. G. Minas, J. S. Martins, J. C. Ribeiro, R. F. Wolffenbuttel and J. H. Correia, "Biological Microsystem for Measuring Uric Acid in Biological Fluids," *Sensors and Actuators A-Physical*, vol. 110, No. 1-3, pp. 33-38, 2004.

120. T. Kamei, B. M. Paegel, J. R. Scherer, A. M. Skelley, R. A. Street and R. A. Mathies, "Integrated Hydrogenated Amorphous Si Photodiode Detector for Microfluidic Bioanalytical Devices," *Analytical Chemistry*, vol. 75, No. 20, pp. 5300-5305, 2003.

121. O. Leistiko and P. Friis, "Bio/chemical Microsystems with Integrated Photodiode Arrays of Improved Sensitivity and Functionality," in *Proceedings of the SPIE - The International Society for Optical Engineering*, pp. 10-19, 1999.

122. M. L. Adams, M. Enzelberger, S. Quake and A. Scherer, "Microfluidic Integration on Detector Arrays for Absorption and Fluorescence Micro-spectrometers," *Sensors and Actuators A-Physical*, vol. 104, No. 1, pp. 25-31, 2003.

123. R. Korde, C. Prince, D. Cunningham, R. E. Vest and E. Gullikson, "Present Status of Radiometric Quality Silicon Photodiodes," *Metrologia*, vol. 40, No. 1, pp. S145-S149, 2003.

124. L. R. Canfield, R. E. Vest, R. Korde, H. Schmidtke and R. Desor, "Absolute Silicon Photodiodes for 160 nm to 254 nm Photons," *Metrologia*, vol. 35, No. 4, pp. 329-334, 1998.

125. T. Rohr, D. F. Ogletree, F. Svec and J. M. J. Frechet, "Surface Functionalization of Thermoplastic Polymers for The Fabrication of Microfluidic Devices by Photoinitiated Grafting," *Advanced Functional Materials*, vol. 13, No. 4, pp. 264-270, 2003.

126. Y. Li, *Multidimensional Protein Separations in a Plastic Microfluidic Network*, Ph. D. thesis, Department of Chemistry and Biochemistry, University of Maryland, College Park, 2004.

127. J. G. Graeme, *Photodiode Amplifiers: Op Amp Solutions*, Boston, MA: McGraw Hill, 1996.

128. P. Held, "Quantitation of Peptides and Amino Acids with a Synergy HT using UV Fluorescence," B.-T. Instruments, Winooski, VT, 2003.

129. G. Piazza, R. Abdolvand, G. K. Ho and F. Ayazi, "Voltage-Tunable Piezoelectrically-transduced Single-crystal Silicon Micromechanical Resonators," *Sensors and Actuators A-Physical*, vol. 111, No. 1, pp. 71-78, 2004.

130. D. L. DeVoe, "Piezoelectric Thin Film Micromechanical Beam Resonators," *Sensors and Actuators A-Physical*, vol. 88, No. 3, pp. 263-272, 2001.

131. B. Piekarski, D. DeVoe, M. Dubey, R. Kaul and J. Conrad, "Surface Micromachined Piezoelectric Resonant Beam Filters," *Sensors and Actuators A-Physical*, vol. 91, No. 3, pp. 313-320, 2001.

132. G. Piazza, P. J. Stephanou, J. M. Porter, M. B. J. Wijesundara and A. P. Pisano, "Low Motional Resistance Ring-shaped Contour-mode Aluminum Nitride Piezoelectric Micromechanical Resonators for UHF Applications," in *Proceedings 18th IEEE International Conference on Micro Electro Mechanical Systems*, Miami Beach, FL, USA, pp. 20-23, 2005.

133. A. N. Cleland, M. Pophristic and I. Ferguson, "Single-crystal Aluminum Nitride Nanomechanical Resonators," *Applied Physics Letters*, vol. 79, No. 13, pp. 2070-2072, 2001.

134. T. Thundat, G. Y. Chen, R. J. Warmack, D. P. Allison and E. A. Wachter, "Vapor Detection Using Resonating Microcantilevers," *Analytical Chemistry*, vol. 67, No. 3, pp. 519-521, 1995.

135. B. Ilic, Y. Yang, K. Aubin, R. Reichenbach, S. Krylov and H. G. Craighead, "Enumeration of DNA Molecules Bound to a Nanomechanical Oscillator," *Nano Letters*, vol. 5, No. 5, pp. 925-929, 2005.

136. B. Ilic, H. G. Craighead, S. Krylov, W. Senaratne, C. Ober and P. Neuzil, "Attogram Detection Using Nanoelectromechanical Oscillators," *Journal of Applied Physics*, vol. 95, No. 7, pp. 3694-3703, 2004.

137. J. Fritz, M. K. Baller, H. P. Lang, H. Rothuizen, P. Vettiger, E. Meyer, H. J. Guntherodt, C. Gerber and J. K. Gimzewski, "Translating Biomolecular Recognition into Nanomechanics," *Science*, vol. 288, No. 5464, pp. 316-318, 2000.

138. L. Li, *Piezoelectric Microbeam Resonators Based on Epitaxial Al0.3Ga0.7As Films*, Ph. D. thesis, Department of Mechanical Engineering, University of Maryland, College Park, 2005.